University of Bergen
Department of Physics and Technology

Master Degree Project in
Measurement Science and Instrumentation

Permittivity measurements using dual open ended coaxial probes

Mahsa Karimi

November 2012

O

Abstract

The motivation for this study has been to conduct a feasibility study on a measuring device to monitor hydrate formation close to the inner surface of a pipe where a multiphase hydrocarbon fluid mixture is flowing. This measurement device is supposed to measure both the permittivity and the conductivity of the fluid mixture, and estimate the hydrate layer thickness formed on the inner surface of the pipe. The permittivity was calculated using a Bilinear Calibration Procedure (BCP) based on reflection measurements within the frequency range of 10 MHz – 13 GHz using two different open-ended coaxial probes. Measurements on fluids with known permittivity were used to verify the sensitivity and reproducibility of the measurement device. Two open ended coaxial sensors with different geometries mounted into the pipe wall may be a suitable technique for performing hydrate monitoring by measuring the changes of permittivity and corresponding thickness. The objective of this work was to examine if a dual probes system is suitable for measuring both permittivity and thickness of fluid layers with sufficient accuracy to be applied for hydrate monitoring.

The main conclusion of this work is that a two-probe system (small and large) with different geometries and sensitivity depths can be employed to determine both the permittivity and the layer thickness using the BCP and an empirical exponential model. The mounted sensor system on the pipe wall can be a suitable technique for gas hydrate monitoring by measuring the changes of permittivity and corresponding hydrate layer thickness.

In this work, the open ended coaxial sensors, used as non-intrusive permittivity sensors, have been investigated and the basic principles of permittivity measurement on fluid layers have been revealed. A test material of unknown permittivity can be placed in aperture of the sensor where the reflection coefficient will be measured using a network analyzer. The BCP together with a simple capacitance model has been used to determine the broadband complex permittivity from recorded reflection coefficients.

The broadband complex permittivity spectrum contains information about static permittivity, high frequency permittivity, dispersion frequency, etc. It is found that the

apparent static permittivity for an increasing thickness of unknown sample is in good agreement with an empirical model of the open ended coaxial sensors. This empirical model relates the apparent permittivity, the thickness and permittivity of the layer. By applying two coaxial probes with different geometries in an ideal condition for a permittivity known sample, the sensitivity depths and constants of the probes are obtained. The thickness detection is applicable for layers thinner than the sensitivity depth of the large probe. The permittivity measurement is however the most accurate for layers with thickness larger than the sensitivity depth of the small probe. It is found that the thicknesses of the layers can be predicted within minimum 78.23% accuracy (mean accuracy is 89.85%) for layers thinner than the sensitivity depth of the large probe and also it is found that the permittivity of the layers can be calculated within minimum 94.3% accuracy (mean accuracy is 97.4%) for layers thicker than approximately 1.5 mm.

Further on, it is also observed that the relaxation frequency obtained from the broadband complex permittivity spectrum increases as the conductivity of the dispersed phase increases.

Acknowledgment

This thesis is written in collaboration with Christian Michelsen Research (CMR) and University of Bergen (UoB), Department of Physics and Technology, and was submitted for the M.Sc. degree in measurement science and instrumentation.

First of all, I would like to express my best gratitude to my co-supervisors, Kjetil Folgerø at CMR and Bjørn Tore Hjertaker at UoB. I would like to thank specially Kjetil Folgerø; without his daily support at CMR and invaluable suggestions this work would have not been accomplished and thanks Bjørn Tore Hjertaker for giving me not just practical, but moral and spiritual support.

I have been fortunate to work on a subject that has been challenging and interesting. Many people contributed in some way to this work. I would like to express my thanks to the workshop staff of Department of Physics and Technology, where the experimental setup was prepared, for their fast and accurate work. Thanks to Kjetil Haukalid for willingly sharing his experience and knowledge and to Zahra Bayati for her kind supports.

Last but not least, I thank my family and friends for their patience and understanding. I am particularly grateful for all supports given by my lovely husband Omid and my little son Kian.

This page is left intentionally blank.

List of Contents

List of Tables

This page is left intentionally blank.

List of Figures

List of Figures in Appendix

This page is left intentionally blank.

List of Abbreviations

The most commonly used symbols and abbreviations in this work are listed below:

Symbols	Description
T/R	Transmission/Reflection
E	Electrical field
r	Distance from charge Q
Q, q	Charge
ε	Relative dielectric constant
ε_0	Permittivity of vacuum
ε_s	Static relative permittivity
P	Polarization
l	Distance between two charges
u	Dipole moment of a polar molecule
σ_d	Surface charge density
E_{ind}	Electric field inside the capacitor
D	Electric displacement
P	Polarization
$\vec{\mathrm{E}}$	Electric field in the dielectric
k_b	Boltzmann constant
T	Temperature
μ_d	Dipole moment
α_p	Distortion polarizability
M_w	Molecular weight
N_A	Avogadro's constant
ρ	Density
ε_∞	High frequency permittivity
ε^*	Complex relative permittivity
ε'	Dielectric constant
ε''	Dielectric loss
$tan\ \delta$	Dissipation factor
f_d	Dispersion frequency
τ	Relaxation time
σ	Conductivity
ξ	Friction constant
α_d	Distribution factor
H	Magnetic field
B	Magnetic flux density
J	Current density
ρ_q	Charge density
μ	Permeability
λ	Wavelength
TE	Transverse electric wave
TM	Transverse magnetic wave

TEM	Transverse electromagnetic wave
ω	Angular frequency
γ	Propagation constant
α	Attenuation factor
β	Phase constant
c	Speed of light in vacuum
V_0	Amplitude of wave
k	Wave number
E_T	Transverse electric wave
E_Z	Axial electric wave (Z axis)
H_T	Transverse magnetic wave
H_Z	Axial magnetic wave (Z axis)
λ_m	Wavelength in the material
υ_m	Phase velocity in the material
Γ_L	Reflection coefficient
T_L	Transmission coefficient
V_r	Reflected voltage
V_i	Incident voltage
Z_L	Load impedance
Z_0	Characteristic impedance of the coaxial probe
S_{ij}	Scattering parameter
l_e	Electrical length
Γ_M	Measurement plane reflection coefficient
Γ_R	Reference plane reflection coefficient
Γ_M^{ref}	Measurement plane reflection coefficient for reference fluid
Γ_R^{ref}	Reference plane reflection coefficient for reference fluid
a	Inner conductor radius (mm)
b	Outer conductor radius (mm)
C_F	Fringing field in the material
εC_0	Fringing field in the dielectric
Y	Admittance
G_0	Free space radiation conductance
E_{ij}	Scattering parameters of the error network
A_{ij}, B_{ij}, C_{ij}	Calibration coefficients
ε_{app}^*	Apparent permittivity
D_1	Probe constant for the small probe
D_2	Probe constant for the large probe
D_0	Probe constant
d	Thickness
$S(f)$	Sensitivity of the probe
x_e	Mole fraction of ethanol in ethanol/water mixture
ε_1	Permittivity of sample under test
ε_2	Permittivity of backing layer
BCP	Bilinear Calibration Procedure
BCT	Bilinear Calibration Transformation
SUT	Sample Under Test
Φ	Water cut

1 Introduction

At specific low temperature and high pressure conditions, gas hydrates can be formed in hydrocarbon production pipelines. Gas hydrate is an ice-like crystalline solid formed from a mixture of water and natural gas, usually methane. The gas molecules (denoted “guests”) are trapped in water cavities (denoted “hosts”) composed of hydrogen-bonded water molecules, meaning that the building blocks of gas hydrates consist of a gas molecule surrounded by a cage of water molecules. The solid formed is composed of crystallized water (ice) molecules, making a rigid cages (a clathrate) containing a molecule of natural gas, mainly methane [1].

A significant challenge in flow assurance during production and transportation of hydrocarbons is hydrate plugging of the pipelines, which may be prevented by using methods such as insulation, heating or by adding chemical inhibitors. However, both heating and insulation are expensive and not realistic, therefore adding a thermodynamic inhibitor is the most common method to reduce or stop hydrate formation. Due to environmental and economic considerations, the amount of additives should be as low as possible. Gas hydrates are clathrate structures between water as host molecules and gas-molecules. These clathrate structures consist of different unit cells which are formed by hydrogen bonded water, and the entrapped guest molecule stabilizes the structure by van der Waals interactions [2]. When gas hydrate formation is taking place, free water molecules are converted to clathrate structure. The change in structure of the water gives changes in dielectric properties. Subsequently, formation of gas hydrate in mixture can be detected by monitoring local changes in the dielectric parameters. Permittivity measurements have wide range applicability such as research within medical and industrial applications, in addition to qualitative and quantitative applications. As an example, quality measurement of materials such as e.g. characterization of drugs in pharmacy, in the food industry, characterization of concrete and quantity measurements incorporated in multiphase meters in the oil and gas industry.

In a pipeline, the hydrate can flow with the fluid phase, especially the liquid, and it will tend to accumulate in the same location as the liquid does [3]. The most probable location

for hydrates to form is on the inner wall of the pipeline. In annular multiphase flow regime, in which the lighter fluid flows in the centre of the pipe and the heavier fluid is contained in a thin film on the pipe wall, hydrate formation can take place on the wall of the pipeline, and a layer of hydrates can deposit on the wall. In the worst case it can cause severe problems such as agglomeration and plugging of the line. The aim of this thesis is to investigate if dielectric spectroscopy and coaxial sensors can be used to detect formation of hydrates in hydrocarbon production and subsequently determine the thickness of hydrate layers.

The open-ended coaxial probe is considered to be a suitable sensor for measuring the permittivity of fluid layers or films close to a pipe wall. The permittivity is calculated from the measured reflection coefficient of the probe. The main challenge involving measurement with an open ended coaxial probe is that there is no simple analytical relationship between the reflection coefficient and the permittivity. For determining the complex permittivity of the sample, some models have been developed in the past such as the BCP and the iterative algorithms from calibrated scattering parameter measurements [4]. The open ended coaxial probe is also suitable for conductivity measurement of the fluid layer, where the relaxation frequency of the Maxwell-Wagner effect depends on the conductivity of the dispersed phase.

To avoid pressure drop in the pipeline, the permittivity measurement device should preferably be of a non-intrusive nature, and it should demand little or no maintenance. Since the open ended coaxial sensor is non-intrusive, it is suitable to be integrated into the pipe wall in direct contact with the flow, i.e. without disturbing flow regime and creating a pressure drop. Moreover, it should be non-destructive that there is no need for sample customization, and it has the potential for on-line use. These properties makes this kind of probe applicable to be used in broad band dielectric measurements [5] of multiphase hydrocarbon annular flow.

Figure 1.1 illustrates the difference between a coaxial cell and a probe. The coaxial cell is more sensitive than the coaxial probe but it is intrusive. Since the coaxial probe is not intrusive, it is commonly used for measurements of broad band permittivities by transmission and reflection methods.

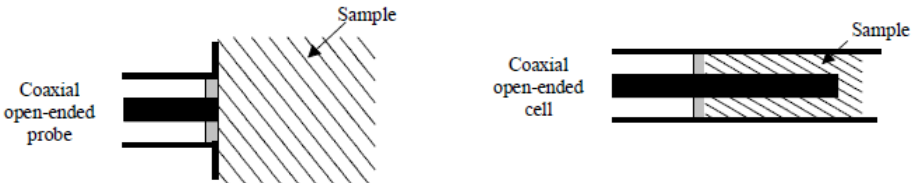

Figure 1.1: Two different types of open ended coaxial sensors [5].

Although Marcuvitz was the first to develop and analyze these probes in 1951 [6], Tanabe and Jones [7] was in 1976 the first to make use of them to measure permittivity of materials. The main challenge using coaxial probes was to develop a relationship between the measured data and the permittivity of the test sample, especially in the high frequency range [5]. The "lumped parameter model" was introduced by Stuchly et al. in the low frequency range in the 1980's [8] [9] [10] [11] [12] and [13]. These models did however not work in the high frequency range. However, during the 1990's, models based on the electromagnetic equations and full wave analysis were introduced with applicability over a wide frequency range [4] [14] [15] [16] [17] [18] and [19].

1.1 Project goal and thesis build up

The aim of this project was to investigate the possibility of monitoring gas hydrate formation in multiphase hydrocarbon annular flow. A multiphase flow regime is assumed in which the lighter fluid (gas) flows in the center of the pipe, whereas the heavier fluid (emulsion) is contained in a thin film on the pipe wall. Consequently, hydrates may form close to the inner surface of the pipe where the multiphase mixture of gas and liquid is flowing. The coaxial probes are most sensitive to the dielectric closest to the probes, and the open-ended coaxial probes are therefore mounted flush with the pipe wall to detect hydrate formation on the inner pipe wall. As the coaxial probes are non-intrusive, pressure drop along the pipeline is avoided. By implementing a dual probes system, the permittivity and the layer thickness can be estimated by the empirical models. By comparing the measured permittivity with the hydrate permittivity, hydrate formation can be indicated, where the hydrate layer thickness also can be estimated. The conductivity of the fluid mixture can also be determined by the Hanai-Boyle mixture equation and the Maxwell-Wagner effect.

Figure 1.2 shows a schematic of the dual open-ended probes used in this study to detect formation of hydrates. The location of the probes, the gas flow component and the thin layer of the fluid film are also shown in the figure. In vertical annular flow it can be assume that the liquid is distributed evenly on the inner surface of the pipe, and that the thickness of the liquid film is approximately the same in different sections of the pipe.

The objective of this work was to examine if a dual probes system is suitable for measuring both permittivity and thickness of fluid layers with sufficient accuracy to be applied for hydrate monitoring.

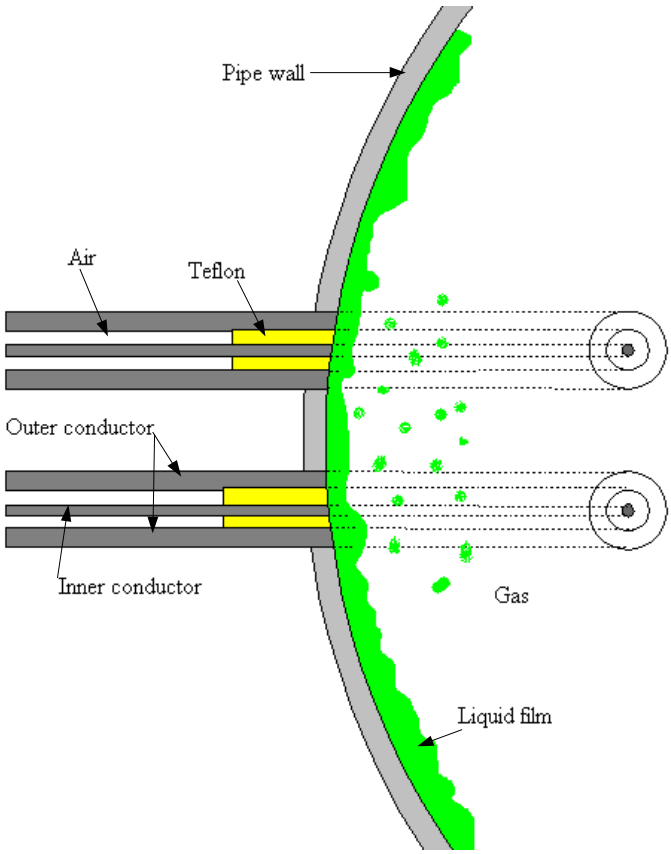

Figure 1.2: Dual open ended coaxial probes for measurement of relative permittivity and thickness of liquid film in multiphase annular flow.

This page is left intentionally blank.

2 Background Theory

2.1 Permittivity

Permittivity measurement methods can be classified into single frequency and broad band frequency methods. Although single frequency methods ensure high accuracy and precision permittivity measurements, broad band methods provide quicker permittivity measurements over a wide frequency range. For broad band measurements, the sample is typically placed between the inner and the outer conductor of a coaxial cable. The signal applied to the sample is partly transmitted, partly reflected and partly absorbed, and the permittivity of the sample can be calculated from transmission/reflection coefficients. The basic principles of broad band measurement in coaxial cells were developed in 1970s. In dielectric spectroscopy the permittivity change of a material over a broad band frequency range is investigated [20]. The dielectric spectra contain information about the structure and composition of material being examined.

2.1.1 Dielectric constant

Intermolecular forces can be categorized into different classes. Electrostatic force is among those forces that arise from the Coulomb force between charges. The interactions between e.g. ions, permanent dipoles and quadruples also recognize as this type of force [21]. It also involves polarization interaction resulting from the dipole moments induced in atoms and molecules by the electrical field of nearby charges and/or permanent dipoles. The electrical field *(E)* at a distance *r* away from charge Q_1 is:

$$E_1 = \frac{Q_1}{4\pi\varepsilon_0\varepsilon r^2} \tag{1}$$

where ε is the relative permittivity or dielectric constant of the medium and the ε_0 is the permittivity of vacuum. Israelachvili [21] defines the dielectric constant as a measure of the extent of electrical field reduction, and consequently a measure of the reduced strength

of electrostatic interaction in medium. The dielectric permittivity is a function of frequency i.e. ε(*f*), and is also known as the relative permittivity, which is the ratio of the electrical field stored in a material by the applied voltage relative to that stored in free space. Dielectric constant is ratio of permittivity of medium to the permittivity of free space. As Permittivity of medium and permittivity of free space both have same units dielectric constant becomes dimensionless quantity. The relative permittivity of a material for zero frequency i.e. ε_s is referred as the static relative permittivity [5].

Figure 2.1 shows the typical behaviour of permittivity as a function of frequency, where a variety of physical phenomena can affect the permittivity of a material such as atomic, electronic and orientation polarization which will be discussed in the next parts. In the microwave frequency range, dipolar relaxation leads to variation in permittivity. The nature of electronic and atomic polarization is the same. In neutral atoms when an electric field displaces the nucleus from electrons, electronic polarization occurs, and by applying an electric field, adjacent positive and negative ions stretch and atomic polarization occurs [22].

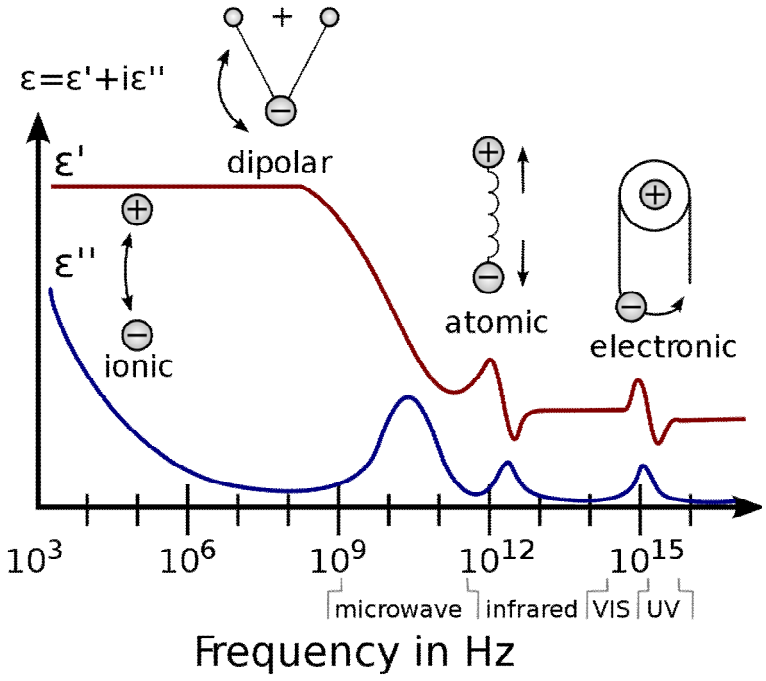

Figure 2.1: Dielectric permittivity spectrum over a wide frequency range. ε' is the dielectric constant (red) and ε'' is the dielectric loss (blue) [23].

2.1.2 Polarization

In dielectrics, all charges are tightly attached to specific atoms or molecules, and all they can do is a bit of movement within an atom or the molecule. When a neutral atom is placed in an electrical field, there will be a positively charged core (the nucleus) and a negatively charged electron cloud surrounding it. The nucleus is pushed in the direction of the field, and the electrons will be pushed the opposite way. The two opposing forces reach a balance, leaving the atom polarized [24].

When a separation exists between the average position of the negative and the average position of positive charges in the atom, it is called polar atoms [25]. If the material consists of neutral atoms or non-polar molecules, the electrical field will induce a tiny dipole moment in each of these, pointing in the same direction as the field, whereas for the material containing polar molecules, each dipole will experience a torque, tending to line up along the field direction. Subsequently, many small dipoles pointing along the direction of the electrical field are produced and the material becomes polarized. The dipole moment of a polar molecule is defined as $u=ql$ where l is distance between the two charges $+q$ and $-q$. The polarization can be estimated based on dipole moment per unit volume.

In the case of two parallel plates as a capacitor with surface charge densities $+\sigma_d$ and $-\sigma_d$ on the two electrodes as shown in Figure 2.2, the electric field inside the capacitor assuming vacuum is, $E_0=\sigma_d/\varepsilon_0$, where ε_0 is the permittivity of vacuum equal to 8.854 pF m^{-1}.

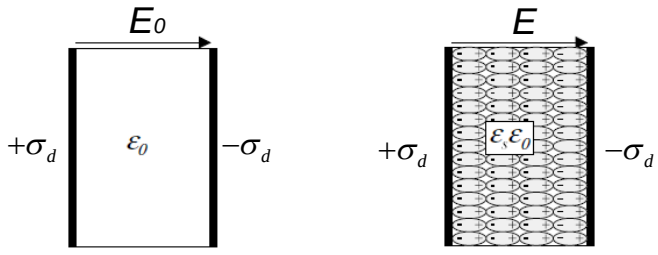

Figure 2.2: Capacitor with and without a dielectric material between the two plates [5].

By placing a dielectric material made of polar molecules in the electric field between the plates of the capacitor, in the absence of an electric field the dipoles are randomly oriented. However, if an electric field is applied, the dipoles will align with the electrical field. The

dielectric is now polarized, and if a material with permittivity ε_s is placed between the two plates, the electric field inside the capacitor is:

$$E_{ind} = \frac{\sigma_d}{\varepsilon_s \varepsilon_0} \tag{2}$$

The net electric field $\vec{E}$ in the dielectric is [25]:

$$\vec{E} = E_0 - E_{ind} \tag{3}$$

The reduction in electric field will lead to a reduction of the surface charge density, and this difference in surface charge density is called electrical polarization of the material (i.e. *P*) given in equation 4 [5]:

$$P = \sigma_d \left(1 - \frac{1}{\varepsilon_s}\right) \tag{4}$$

The new electrical field, which has been faced with the reduction in surface charge density, is called the electric displacement (*D*), and relates to the electric field and polarization as follows:

$$D = \sigma_d = \varepsilon_s \varepsilon_0 E = \varepsilon_0 E + P \tag{5}$$

Re-writing equation 5, gives the polarization using electrical field and permittivity:

$$P = (\varepsilon_s - 1)\varepsilon_0 E \tag{6}$$

As shown in Figure 2.1, there are three main molecular mechanisms that may contribute to the total polarization [26]:

1. Atomic polarization (electron clouds relative to the nuclei)
2. Electronic polarizations (electron clouds relative to the nuclei)
3. Orientation polarization (the torque of the electric fields tend to align permanent electric dipole moments)

In 1929, Debye derived a model for the relationship between static permittivity and molecular properties considering polarizability [27]:

$$\frac{\varepsilon_s - 1}{\varepsilon_s + 2}\frac{M_w}{\rho} = \frac{N_A}{3\varepsilon_0}\left(\alpha_p + \frac{\mu_d^{\,2}}{3k_b T}\right) \tag{7}$$

where k_b is the Boltzmann constant, T is the temperature, μ_d is the dipole moment, α_p is the distortion polarizability, M_w is the molecular weight, ρ is the density and N_A is Avogadro's constant.

In an alternating electrical field of sufficiently high frequency, the dipoles are unable to align themselves along the electrical field, and the permittivity will decrease from its static value ε_s to its high frequency value ε_∞ accordingly. Only the distortion polarizability will contribute to the permittivity and hence equation 7 is revised into the Lorentz-Lorentz relationship given in equation 8:

$$\frac{\varepsilon_s - 1}{\varepsilon_s + 2}\frac{M_w}{\rho} = \frac{N_A}{3\varepsilon_0}\alpha_p \tag{8}$$

2.1.3 Complex permittivity

Permittivity is a frequency dependent property and can be expressed as a complex variable. In dielectric spectroscopy the frequency dependency of the permittivity is characterized. The measured dielectric spectra contain information relating to the structure and composition of material being examined.

As shown in Figure 2.1 (blue curve), the permittivity decreases from its maximum (i.e. static) value to the corresponding value (ε_∞) as the frequency increases. This reduction region is called the dispersion region and is characterized by a phase-difference between the applied electric field, *E*, and the displacement vector, *D*. Consequently, *D/E* is a complex variable.

$$\frac{D}{E} = \varepsilon^*\varepsilon_0 = \left(\varepsilon' - j\varepsilon''\right)\varepsilon_0 \tag{9}$$

where ε^* is the complex relative permittivity, ε' is the dielectric constant and ε'' is the dielectric loss. The phase difference between *D* and *E* will result in energy absorption in the form of heat. The absorption is zero when the dielectric loss ε'' is zero. The ratio between ε' and ε'' is defined as the dissipation factor.

$$\tan\delta = \frac{\varepsilon''}{\varepsilon'} \tag{10}$$

The frequency where the dielectric loss is at its maximum is called the dispersion frequency f_d. The relaxation time τ at this frequency is:

$$\tau = \frac{1}{2\pi f_d} \tag{11}$$

In case of a dielectric possessing a finite conductivity σ, loss in a dielectric material is expected, which can be defined as:

$$\varepsilon^* = \varepsilon' - j\left(\varepsilon'' + \frac{\sigma}{\omega\varepsilon_0}\right) \tag{12}$$

Debye's equation describes the dielectric relaxation process as follows:

$$\varepsilon^* = \varepsilon_\infty + \frac{\varepsilon_s - \varepsilon_\infty}{1 + j\omega\tau} - j\frac{\sigma}{\omega\varepsilon_0} \tag{13}$$

where τ is the macroscopic relaxation time and ξ is the friction constant describing rotational capability of the molecule in the medium as follows:

$$\tau = \frac{\varepsilon_s + 2}{\varepsilon_\infty + 2} \times \frac{\xi}{2k_b T} \tag{14}$$

For monohydric alcohols a multiple Debye model with up to three discrete relaxation times have been reported in the literature [28] [29] [30] and [31]. To analytically represent the present spectra within the limits of error, it is sufficient to consider the double Debye equation:

$$\varepsilon^* = \varepsilon_\infty + \frac{\Delta\varepsilon_1}{1 + j\omega\tau_1} + \frac{\Delta\varepsilon_2}{1 + j\omega\tau_2} \tag{15}$$

where $\varepsilon_s = \varepsilon_\infty + \Delta\varepsilon_1 + \Delta\varepsilon_2$. Many relaxation processes can take place in the materials, which can be written as a sum of Debye processes with different relaxation times. If the relaxation times are symmetrically around a common value, they can be described by an empirical factor α_d in Debye's equation [27]. Cole and Cole extended Debye's formula by introducing a distribution of the relaxation time [32]:

$$\varepsilon^* = \varepsilon_\infty + \frac{\varepsilon_s - \varepsilon_\infty}{1 + \left(j\omega\tau\right)^{1-\alpha_d}} - j\frac{\sigma}{\omega\varepsilon_0} \tag{16}$$

where α_d is distribution factor. Figure 2.3 demonstrates the difference between Debye (solid line) and Cole-Cole (dashed line) dispersion profile [5].

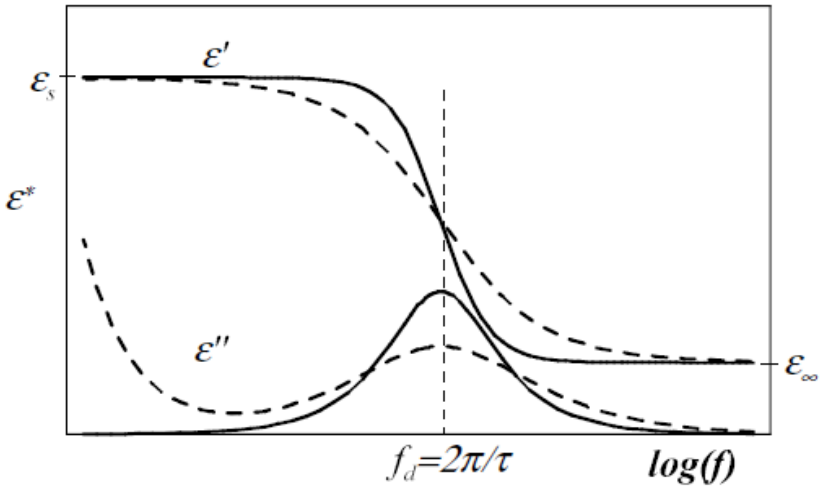

Figure 2.3: A comparison between the Debye (solid line) and Cole-Cole (dashed line) permittivity profiles as a function of frequency [5].

2.2 Propagation of electromagnetic waves in transmission lines

A macroscopic material can be exposed to an electromagnetic field rather than electrical field. The interaction between a macroscopic material and electromagnetic fields are generally described by Maxwell's equations as follows:

$$\nabla.D = \rho_q \tag{17}$$

$$\nabla.B = 0 \tag{18}$$

$$\nabla \times H = \partial D / \partial t + J \tag{19}$$

$$\nabla \times E = -\partial B / \partial t \tag{20}$$

where *D*, *B* and *J* are defined as follows:

$$D = \varepsilon * E = (\varepsilon' - j\varepsilon'')E \tag{21}$$

$$B = \mu H = (\mu' - j\mu'')H \tag{22}$$

$$J = \sigma E \tag{23}$$

where *H* is the magnetic field; *E* is electric field; *B* is the magnetic flux density; *D* is the electric displacement; *J* is the current density; ρ_q is the charge density; ε* is the complex permittivity; μ is the complex permeability and σ is the conductivity of the material [24].

There are resonant and non-resonant methods for characterization of material properties. The microwave phenomena related to these methods are microwave propagation and microwave resonance. Propagation of an electromagnetic wave along a transmission structure can be analyzed using Maxwell's equations:

$$\nabla^2 E + k^2 E = 0 \tag{24}$$

$$\nabla^2 H + k^2 H = 0 \tag{25}$$

where $k=2\pi/\lambda$ represents the wave number and λ is the wavelength. *E* and *H* can be written as a sum of the transverse and the axial components:

$$E = E_T + E_Z \tag{26}$$

$$H = H_T + H_Z \tag{27}$$

There are three types of electromagnetic waves with special E_Z and H_Z. If E_Z equals zero, the electromagnetic wave is called a transverse electric wave (TE). If H_Z equals zero, the electromagnetic wave is called a transverse magnetic wave (TM). If both E_Z and H_Z are zero, the electromagnetic wave is called a transverse electromagnetic wave (TEM). A transverse electromagnetic wave (TEM) that propagates in the +*z*-direction through a

transmission line filled with a dielectric material with permittivity of ε^* and angular frequency of ω can be described as:

$$V(z,t) = V_0 \exp(j\omega t - \gamma z) \tag{28}$$

where V_0 is the amplitude of wave and γ is the propagation constant given by equation 29:

$$\gamma = \alpha + j\beta = j\frac{\omega}{c}\sqrt{\varepsilon^*} \tag{29}$$

where α is the attenuation factor, β is the phase constant and c is the speed of light in vacuum. Figure 2.4 shows how the electromagnetic waves behave in a medium with and without a dielectric material on the right and left hand side, respectively.

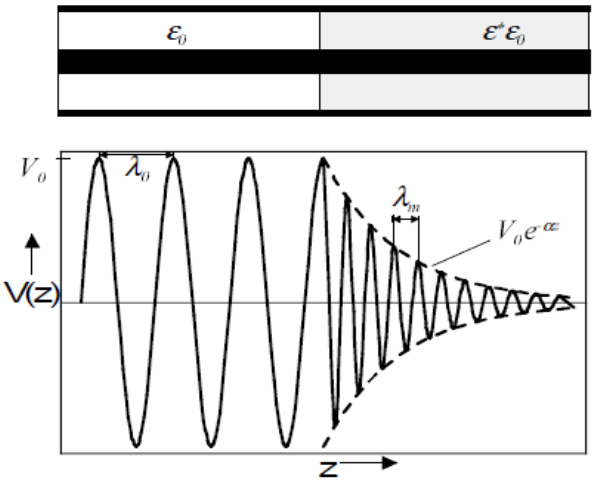

Figure 2.4: Electromagnetic wave propagation in a medium with and without a dielectric material (right and left, respectively) [5].

As shown in Figure 2.4, if a dielectric material exists between the inner and the outer conductor, the wave will be attenuated exponentially $e^{-\alpha z}$, and the wavelength in the material decreases to a value of $\lambda_m = 2\pi/\beta$. Hence, the phase velocity is reduced as follows:

$$\upsilon_m = f\lambda_m = \frac{\omega}{\beta} \tag{30}$$

Equation 29 can be split into its real and imaginary parts, where the permittivity can be defined such that ε' and ε'' are taken into account, as discussed in previous section, i.e. equations 9 and 10:

$$\alpha = \frac{\omega}{c}\sqrt{\frac{\sqrt{\varepsilon'^2+\varepsilon''^2}-\varepsilon'}{2}} = \frac{\omega}{c}\sqrt{\varepsilon'\frac{\sqrt{1+\tan^2\delta}-1}{2}} \tag{31}$$

$$\beta = \frac{\omega}{c}\sqrt{\frac{\sqrt{\varepsilon'^2+\varepsilon''^2}+\varepsilon'}{2}} = \frac{\omega}{c}\sqrt{\varepsilon'\frac{\sqrt{1+\tan^2\delta}+1}{2}} \tag{32}$$

For low-loss materials the above equations can be simplified to:

$$\alpha \approx \frac{\omega}{c}\frac{\varepsilon''}{2\sqrt{\varepsilon'}} \tag{33}$$

$$\beta \approx \frac{\omega}{c}\sqrt{\varepsilon'} \tag{34}$$

Knowing the attenuation and phase constants of a dielectric material, the real and imaginary parts of the permittivity can be determined using the following equations [5].

$$\varepsilon' = \frac{c^2(\beta^2-\alpha^2)}{\omega^2} \tag{35}$$

$$\varepsilon'' = \frac{c^2(2\alpha\beta)}{\omega^2} \tag{36}$$

2.3 Permittivity measurement methods

In 1974 Weir found that permittivity measurements could be conducted directly in the frequency domain using a network analyzer [33] with the combined reflection and transmission method presented by Nicolson and Ross. In the early 1980s, Cole developed a Bilinear Calibration Procedure. The BCP provided a tool for compensating errors caused by signal lines and connectors, as well as the non-ideal behaviour of the probe itself [34].

2.3.1 The permittivity estimation procedure

The procedure for estimating the permittivity of a sample located in front of the open ended probe includes the following three steps:

1. Calibration of the network analyzer and probe length compensation
2. Determine the sensor model
3. Calculation of the permittivity

Calibration of the network analyzer must be performed in order to define the end of the coaxial cable, i.e. the measurement plane, as shown in Figure 2.5. This is usually done by measuring the reflection from an open circuit, a short circuit and a matched termination (load) at the end of coaxial cable [35].

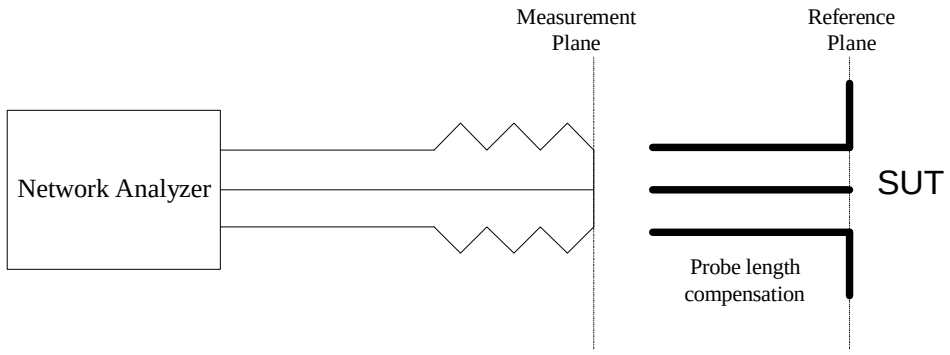

Figure 2.5: Sketch of the measurement system including measurement and reference planes.

The sensor model relates the permittivity of the SUT (Sample Under Test) to the reflection at the reference plane defined as the probe fluid interface. Therefore, the measurement system must initially be calibrated at the reference plane to determine the accurate permittivity.

This standard calibration procedure compensates for source mismatch, frequency response dependency, directivity in the network analyzer, electrical length and non-perfect behaviour of the coaxial cable. However, some additional errors will still be present, such as:

- The physical length of the probe
- Mismatch in the connection between the coaxial cable and the probe
- Mismatch in the probe itself

The ideal calibration consists of calibrating the system at the end of probe using short, open and matched termination. However, making a perfect matched termination is difficult, and therefore the standard calibration method is preferred. The standard calibration system should be performed at the end of the probe, and some additional calibrations are needed to compensate for the probe and its connection. The reference plane rotation and two-port error models can compensate for the probe and its connection.

2.3.2 S-parameter (Scattering Parameter)

In a uniform transmission line, a voltage wave has two components propagating along the $+z$ and $-z$ direction, called the incident and the reflection waves, respectively. As shown in Figure 2.6, a load with impedance Z_L is connected to a piece of transmission line.

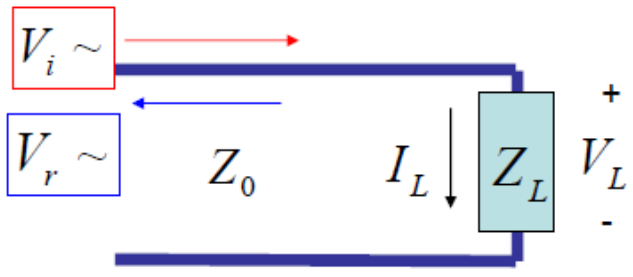

Figure 2.6: Schematic of a transmission line.

The voltage reflection coefficient represents the voltage ratio between the reflected voltage (V_r) and the incident voltage (V_i):

$$\Gamma_L = \frac{V_r}{V_i} \tag{37}$$

Following, the impedance can be expressed through equation 38:

$$Z_L = \frac{V_L}{I_L} = Z_0 \frac{V_i + V_r}{V_i - V_r} = Z_0 \frac{1+\Gamma_L}{1-\Gamma_L} \tag{38}$$

Knowing the impedance, the reflection coefficient is determined [22]:

$$\Gamma_L = \frac{Z_L - Z_0}{Z_L + Z_0} \tag{39}$$

The relationship between the input wave and output waves are often described by scattering parameters [S], where a_x and b_x are the input and the output waves, respectively.

$$[b_x] = [S][a_x] \tag{40}$$

Figure 2.7 demonstrates a simple two port network consisting of two inputs and two outputs that can be defined as $[a_x] = [a_1, a_2]^T$ and $[b_x] = [b_1, b_2]^T$. The scattering parameter matrix [S] is given by [22]:

$$S_{ij} = \frac{b_i}{a_j}[S] = \begin{bmatrix} S_{11} & S_{12} \\ S_{21} & S_{22} \end{bmatrix} \tag{41}$$

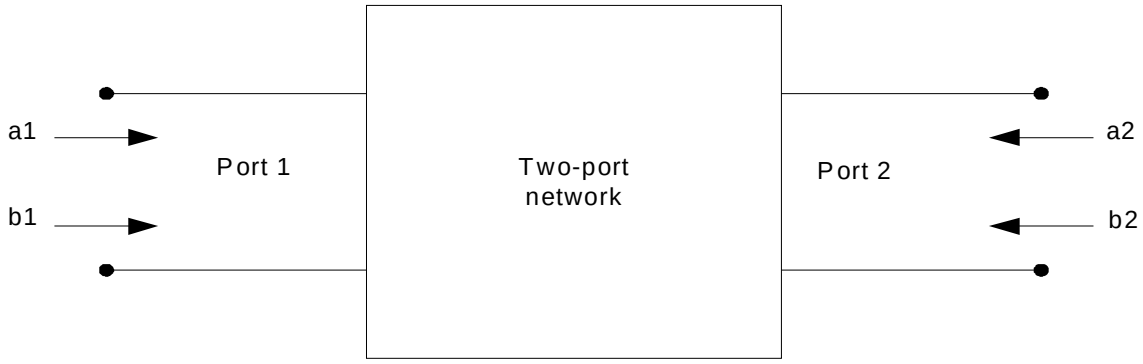

Figure 2.7: Simple schematic of a two port network with input and output waves (a_x and b_x) at each port.

The scattering parameter S_{ij} assuming $a_i=0$ $(i\neq j)$, from equation 41, is given as:

$$S_{jj} = \frac{b_j}{a_j} (j=1, 2) \tag{42}$$

and

$$S_{ij} = \frac{b_i}{a_j} (i \neq j;\ i=1,2\ ;j=1,2) \tag{43}$$

When port j is connected to a source and the other port is connected to a matching load, the reflection coefficient at port j is:

$$\Gamma_j = S_{jj} = \frac{b_j}{a_j} \tag{44}$$

Furthermore, when port j is connected to a source, and port i is connected to a matching load, the transmission coefficient from port j to port i is:

$$T_{j\to i} = S_{ij} = \frac{b_i}{a_j} \tag{45}$$

2.3.3 Reference Plane Rotation

For a well designed probe with no mismatch at the connector, the relationship between the measured reflection coefficient and reference plane coefficient is:

$$\Gamma_R = \Gamma_M e^{2\gamma l_e} \tag{46}$$

where l_e is the electrical length of the probe and γ is the propagation constant. There is a phase shift between the measured reflection coefficient and reference plane coefficient. By normalization (to the measurements on a reference fluid such as air), the effect of the phase shift can be removed by:

$$\frac{\Gamma_R}{\Gamma_R^{ref}} = \frac{\Gamma_M}{\Gamma_M^{ref}} \tag{47}$$

where Γ_R^{ref} is the reference plane reflection coefficient for reference fluid and Γ_M^{ref} is the measurement plane reflection coefficient for reference fluid.

The reflection coefficient at the reference plane is [5]:

$$S_{11}^R = \frac{\Gamma + pz^2}{1 + p\Gamma z^2} \tag{48}$$

$$\Gamma = \frac{1 - g\sqrt{\varepsilon^*}}{1 + g\sqrt{\varepsilon^*}} \tag{49}$$

$$z = \exp(-\gamma l) = \exp(-\frac{j\omega l}{c}\sqrt{\varepsilon^*}) \tag{50}$$

$$p = \frac{Z_t - Z_{C0}/\sqrt{\varepsilon^*}}{Z_t + Z_{C0}/\sqrt{\varepsilon^*}} \tag{51}$$

$$g = \frac{Z_0}{Z_{C0}} \tag{52}$$

Equation 48 can be expanded into a power series which was done first by Cole. For $\frac{1}{3}(\gamma l)^2 << 1$ the bilinear equation for the permittivity is:

$$\varepsilon^* = \frac{1}{g\gamma_0 l}\frac{1 - S_{11}^R}{1 + S_{11}^R} \tag{53}$$

where $\gamma_0 = j\omega / c$ is propagation constant in vacuum.

2.3.4 The two-port error model

The transmission/reflection (T/R) methods are commonly used for measurement of the broad band complex permittivity of dielectric materials in the microwave frequency range, i.e. between 300 MHz and 300 GHz. A measurement based on the T/R method proceeds by placing the sample in a waveguide or coaxial transmission line and subsequently to measure the two port complex scattering parameters with a network analyzer. Figure 2.8 shows a two-port error network that represents the difference between the measurement plane and the reference plane. By modelling the transmission line between these two planes, we can compensate for the probe and its connections.

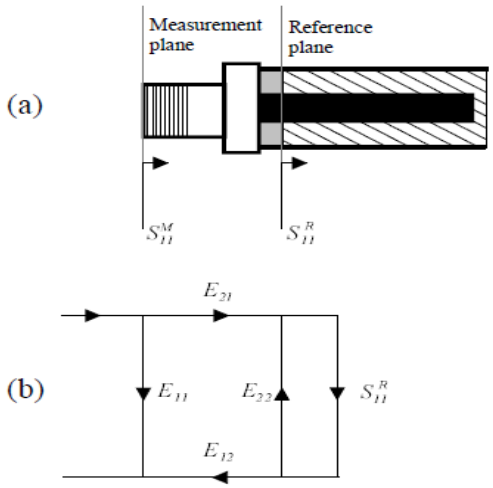

Figure 2.8: Schematic of a two-port error network and corresponding transmission line [5].

The network analyzer is calibrated at the end of the coaxial probes, but equation 48 gives the reflection coefficient at measurement plane. Due to this difference there will be a phase lag between the reflection coefficients at the reference plane and the measurement plane. The calibration procedure is therefore essential. The reference plane reflection coefficient S_{11}^R is found from the measured reflection coefficient S_{11}^M. The scattering parameter for the network is given by

$$S_{11}^R = \frac{S_{11}^M - E_{11}}{E_{22}S_{11}^M + (E_{12}E_{21} - E_{11}E_{22})} \tag{54}$$

where E_{11}, E_{12}, E_{21}, and E_{22} are the scattering parameters of the error network. By rearranging the above equation the BCT is obtained:

$$S_{ij}^R = \frac{A_{ij}S_{ij}^M + B_{ij}}{C_{ij}S_{ij}^M + 1} \ (i=1,2)\ (j=1,2) \tag{55}$$

where A_{ij} ,B_{ij} and C_{ij} are referred to as calibration coefficients, which are found from S-parameter measurements using three different calibration fluids with known high accuracy permittivities. Any errors in the reference values will affect the calibration coefficients, and subsequently cause major uncertainty in the measured permittivity of the unknown fluid [35].

2.3.5 Electromagnetic models of the open-ended coaxial probes

The reflection coefficient at the end of the open-ended coaxial probe is defined as:

$$S_{11}^{R} = \frac{1 - Z_0 Y(\varepsilon^*)}{1 + Z_0 Y(\varepsilon^*)} \tag{56}$$

where Z_0 is the characteristic impedance of the coaxial probe:

$$Z_0 = \frac{60}{\sqrt{\varepsilon'_{coax}}} \ln \frac{b}{a} \tag{57}$$

for a coaxial probe with an inner conductor radius *a*, an outer conductor radius *b* and filled with a material of dielectric constant ε'_{coax} between the inner and the outer conductor. $Y(\varepsilon^*)$ is the aperture admittance of the probe.

The Marcuvitz expression for admittance is as follows [6]:

$$Y(\varepsilon^*) = \frac{j\omega\varepsilon^*}{c\sqrt{\varepsilon_{coax}}} \frac{1}{\ln(b/a)} \int_0^\infty \frac{\left(J_0(\lambda b) - J_0(\lambda a)\right)^2}{\sqrt{\left(\lambda^2 - (\omega/c)^2 \varepsilon^*\right)\lambda}} d\lambda \tag{58}$$

where ε_{coax} is the permittivity of the dielectric bead, and *J* is zero order of the Bessel function of the first kind. This electromagnetic model is a rigorous and complicated one, but in the low frequency range the following equation approaches to a linear capacitance model:

$$Y = j\omega C(\varepsilon) \tag{59}$$

and

$$C(\varepsilon) = C_F + \varepsilon C_0 \tag{60}$$

Where C_F is the fringing field in the material between the inner and the outer conductor, and εC_0 is the fringing field in the dielectric depending on the sample's permittivity [11].

2.3.6 Bilinear Calibration Procedure

The Bilinear Calibration Procedure (BCP) calculates the permittivity based on the measured reflection coefficients. The procedure, which is robust, is a combination of sensor model and probe length compensation. The calculation of the permittivity is quick,

but the experimental calibration routine is time consuming because three samples of known permittivity must be measured. Equation 48 can be expanded into a power series, and an equation for the permittivity as a function of the measured reflection coefficient is then found by combining equation 53 and 55.

$$\varepsilon^* = \frac{\tilde{A}_{ij} S_{ij}^M + \tilde{B}_{ij}}{\tilde{C}_{ij} S_{ij}^M + 1} \tag{61}$$

where $\tilde{A}_{ij}$, $\tilde{B}_{ij}$ and $\tilde{C}_{ij}$ are determined from S parameters measurements of the three fluids with known permittivities, similarly to the BCP. By combining equation 59 with equation 61 and 56, it is found that the BCP (equation 62) is applicable for open-ended coaxial probes.

$$\varepsilon^* = \frac{A_{ij}\rho + \varepsilon_{ref}^*}{1 - B_{ij}} \tag{62}$$

where ε_{ref}^* is the permittivity of a reference fluid. *A* and *B* can be calculated from the *S* parameter measurements of two fluids with known permittivity in the same way as equation 62, where ρ is defined as:

$$\rho = \frac{S_{ij}^{ref} - S_{ij}^M}{S_{ij}^{ref} + S_{ij}^M} \ (i=1,2)\ (j=1,2) \tag{63}$$

where S_{ij}^{ref} is the measured *S* parameter of the reference fluid with permittivity ε_{ref}^*.

The BCP calculates the apparent permittivity on the basis of the measured reflection coefficients, but doesn't give good results when it is extrapolated beyond the calibrated permittivity range.

The model has a limited operating range and will fail in the high frequency range. At frequencies where the wavelength in the sample is comparable to the dimension of the probe, the linear capacitance model fails because the probe becomes radiating, and the deviation between the linear capacitance model and the Marcuvitz model become distinct. This can be compensated for by including a radiation conductance in the linear capacitance model and by letting C_0 become frequency dependent. It can be modified to the admittance model as follows [36]:

$$Y(\varepsilon) = G_0 \omega^4 \varepsilon^{5/2} + j\omega\left(C_F + C_0(\omega)\varepsilon\right) \tag{64}$$

where G_0 is the free space radiation conductance and C_0 is the capacitance that represents the fringing field. For high permittivity samples, such as distilled water in the high

frequency range, the radiation conductance term is dominant. This equivalent circuit model is shown in Figure 2.9.

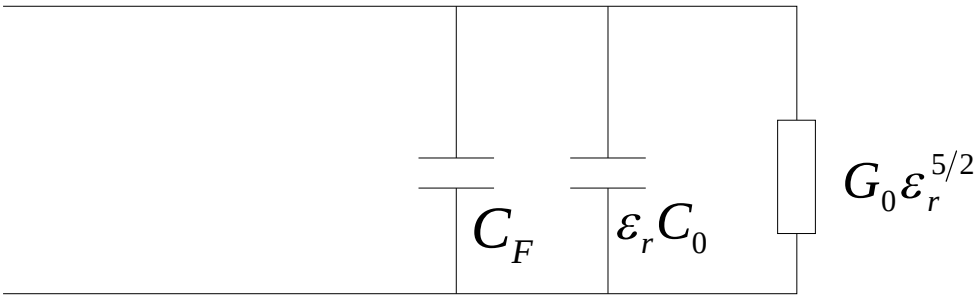

Figure 2.9: Equivalent circuit for coaxial cell filled with dielectric sample.

2.3.7 Electromagnetic resonance

In the high frequency range, the open ended probe may act as an antenna and radiate electromagnetic waves. If these waves are reflected at an interface (see Figure 2.10), they can interfere with the reflected signal from the probe/fluid interface and some peaks and minima may be observed. The reason for the peaks and the minima is that the incident waves to a boundary at some resonance frequencies become constructive and destructive, respectively.

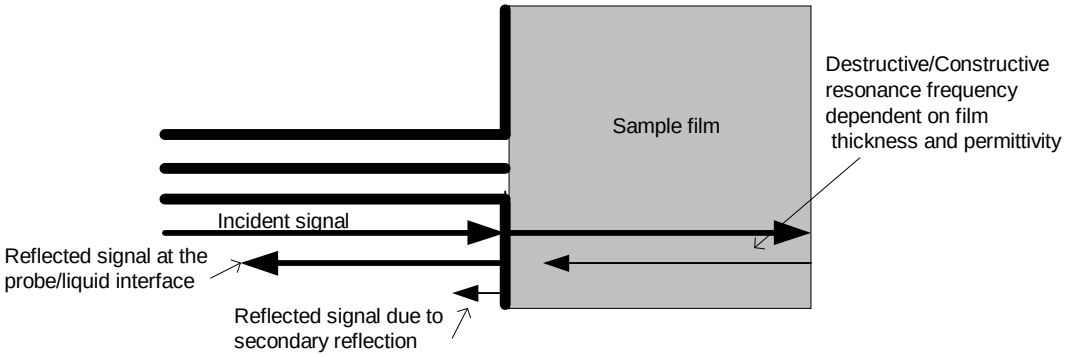

Figure 2.10: Illustration of destructive/constructive resonance in high permittivity fluid films [35].

The destructive / constructive resonance occurs in high permittivity fluid films, and the total reflected signal is influenced by a reflection at the second interface. This secondary reflection varies and vanishes at certain resonance frequencies when destructive /

constructive interference occurs. Therefore, when the resonance occurs, the magnitude of the total reflected signal decreases / increases. Electromagnetic resonance occurs when the film thickness equals any number of a quarter wavelengths. The velocity of the electromagnetic wave is dependent on permittivity. Therefore, the resonance frequency is dependent on both thickness and permittivity of the film (see also equation 31)[35].

$$f_{resonance} = \frac{c}{\frac{4d}{n}\sqrt{\frac{\varepsilon' + \sqrt{\varepsilon'^2 + \varepsilon''^2}}{2}}} \tag{65}$$

2.3.8 Operating frequency range for probes

In order to find out the proper frequency range for each probe two factors have to be taken into account [6]. The first is radiation loss and the second is maximum level of frequency in which the simple capacitance model can be applied.

The radiation loss is not negligible as long as the difference between the inner radius of the outer conductor (b) and the outer radius of the inner conductor (a) is greater than 10% of the sample wave length (λ_m) or $b\text{-}a > 0.1 \cdot \lambda_m$. In other words, the radiation is negligible where $b\text{-}a << \lambda_m$. The corresponding values of a and b are given in Table 3.5. The radiation loss is dependent on frequency and permittivity, as described in equation 64.

The simple capacitance model is applicable when the wavelength of the coaxial line (λ_c) becomes less than the summation of the inner radius of the outer conductor (b) and the outer radius of the inner conductor (a) multiplied by π, i.e. $\lambda_c < \pi(a+b)$. Therefore, this wavelength corresponds to a maximum coaxial frequency (f_c) which correlates the material frequency f_m to f_c according to the following equation: $f_m = f_c \sqrt{\varepsilon^*}$.

2.4 Apparent permittivity

A simple empirical model has been introduced for a sample of finite thickness [5]. This model is based on the assumption that the depth sensitivity of the probes decreases exponentially (first order exponential relationship), and that it is independent of the sample's permittivity and the implemented measurement frequency.

$$\varepsilon_{app}^{*} = (\varepsilon_2^{*} - \varepsilon_1^{*})\exp(-d/D_0) + \varepsilon_1^{*} \tag{66}$$

where the apparent permittivity (ε_{app}^{*}) is the measured permittivity when an infinitely thick sample with permittivity ε_1^{*} is the backing layer for a media with permittivity ε_2^{*}; d is the thickness of the sample and D_0 is an empirical, real parameter depending on the sensor geometry only. The apparent permittivity can be calculated using the BCP. In this work the backing layer was either Teflon or air with permittivities equal to 2.1 and 1, respectively. The sensitivity depth is dependent on the geometry of the probe introduced by the variable real parameter D_0.

The permittivity over the aperture of the coaxial probe is called apparent permittivity. If the thickness of film is more than the sensitivity depth of the probe, the apparent permittivity and the permittivity of SUT may be equal. However for thin film SUT with thickness less than the sensitivity depth of the probe, apparent permittivity will be less than the permittivity of the SUT.

2.4.1 Sensitivity depth

The sensitivity depth is defined as the spatial width of the sensitivity volume of the probe viewed from the probe-fluid interface into the sample. Open ended probe has restricted sensitivity depth, which means that only the sample close to the end of the probe affects the measured reflection coefficient. If the thickness of the film is smaller than a critical thickness, called the depth sensitivity of the probe, the apparent permittivity is lower than the permittivity of the film where the backing layer is a low permittivity material such as air or Teflon. When the thickness of the fluid film is larger than the depth sensitivity, the apparent permittivity is equal to the permittivity of the film, and the permittivity of the backing layer does not influence on the measured permittivity. Thicknesses larger than or

less than the depth sensitivity are referred to as infinite thickness and finite thickness, respectively. An important issue is to determine the sensitivity depths of probes of different geometries.

2.4.2 Sensitivity of the probe

A sensitive measurement element is such that a small change in the input leads to a large change in output, i.e. sensitivity is the gradient of the output versus the input characteristic. For a linear element the relationship is [37]:

$$S = \frac{\Delta O}{\Delta I} \tag{67}$$

The relationship for calculating the sensitivity of a nonlinear element (e.g. coaxial probe) is:

$$S = \left| \lim_{d\varepsilon \to 0} \frac{d\Gamma}{d\varepsilon} \right| \tag{68}$$

Normalized sensitivity can be defined as:

$$S_N = \left| \lim_{d\varepsilon \to 0} \frac{d\Gamma}{d\varepsilon} \frac{\varepsilon}{\Gamma} \right| \tag{69}$$

A sensitive sensor is one with the property that a small change in the permittivity leads to a large change in measured parameter (admittance). The geometric capacitance in equation 58 and 59 should be as large as possible to give high sensitivity measurements [5].
The sensitivity of an open ended coaxial probe will be dependent on:

- Probe dimension
- Operating frequency (modifying input)
- Permittivity of the sample

The sensitivity, *S*, of the probe with respect to permittivity variations can be derived using the expression of the reflection coefficient [35].

$$S(f) = \left| \frac{\varepsilon}{\Gamma(\varepsilon, f)} \frac{\partial \Gamma(\varepsilon, f)}{\partial \varepsilon} \right| \tag{70}$$

where ε is input, f is modifying input and Γ is output.

Figure 2.11 shows how the sensitivity S of a probe varies with frequency and permittivity.

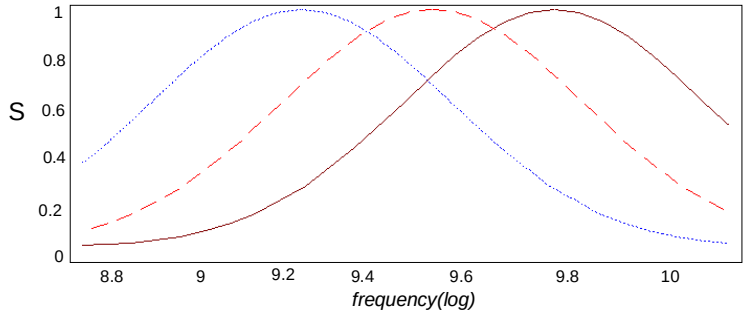

Figure 2.11: The sensitivity S of a probe as a function of frequency and permittivity. The three lines represent the sensitivity for three samples with different permittivities.

The sensitivity of a measurement element will be changed by a possible modifying input I_M. When the modifying input is zero, the measurement is performed at standard condition. If the modifying input is changed from the standard value, then $I_M K_M$ is the deviation from standard conditions (Figure 2.12). The sensitivity changes from K to $K + K_M I_M$, where K_M is the change in sensitivity for unit change in I_M. K_M is referred as environmental coupling constants or sensitivity. As equation 70 shows, the frequency is the modifying input in the coaxial probe system.

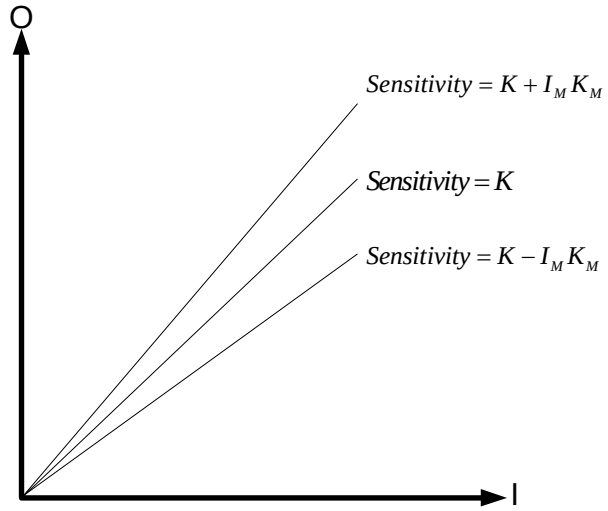

Figure 2.12: The sensitivity changes from K to $K \pm I_M K_M$ by effect of modifying inputs.

The steady state output of this element in general is given by:

$$O = KI + K_M I_M I \tag{71}$$

where O is the dependent variable, which is expressed in terms of the independent variables I and I_M.

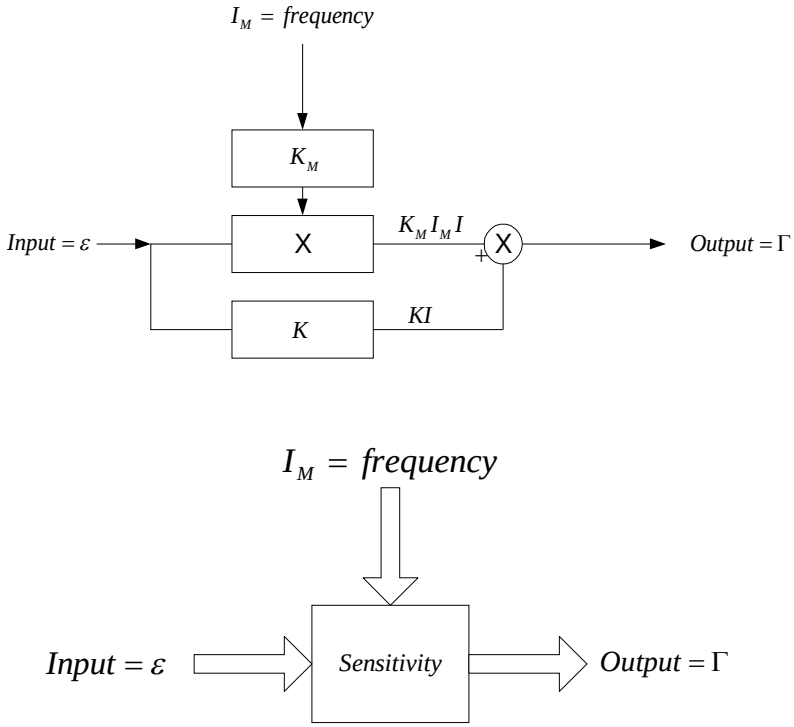

Figure 2.13: General measurement model of the coaxial probe.

As illustrated in Figure 2.13, permittivity and reflection coefficient are introduced as input and output to the system, respectively. The sensitivity of system changes with frequency as a modifying input.

2.5 Dielectric properties of heterogeneous mixtures

In this study permittivity measurements were conducted on quite complex mixtures rather than simplistic water/ethanol mixtures. Consequently, seven mixtures of diesel as the oil component and water with different salinities (conductivities) as water component were used. Diesel has relatively low permittivity and loss, which implies that high sensitivity measurements are required to perform these measurements.

In case of complex permittivity measurements where particle suspensions exist in the fluid mixture, the interaction between particles should be taken into account. For diluted spherical particles there is no such interaction, while for a concentrated particle suspension the interaction between induced dipoles of particles is expected. Referring to various scientists and publications, Asami describes in detail the stages in complex permittivity measurements of two component mixtures [38]. Already in the former century, Maxwell [39] discussed dielectric behaviour of heterogeneous mixtures, and initiated the interest in the associated theoretical models. In 1914 Wagner [40] presented a theory of the dielectric properties of dilute suspensions of spherical inclusions in a continuous medium. Asami referred to Bruggeman whom derived an equation for the conductivity of spherical particle suspensions applying the effective medium theory. In his theory, each particle is assumed to be dispersed into the effective medium, including particles, rather than the real medium. In a following work, the Bruggeman equation was reduced to the Boyle's mixture equation, as given in equation 72.

$$\frac{\varepsilon_{eff}^{*}-\varepsilon_{2}^{*}}{\varepsilon_{1}^{*}-\varepsilon_{2}^{*}}\left(\frac{\varepsilon_{1}^{*}}{\varepsilon_{eff}^{*}}\right)^{N}=1-\Phi \qquad (72)$$

where Φ is the water cut (or volume fraction of water in an oil/water mixture), $\varepsilon_1^{*}=\varepsilon^{*}_{oil}$ and $\varepsilon_2^{*}=\varepsilon^{*}_{water}$. For an ideal water-in-oil emulsion, all particles (water droplets) are assumed to be spherical and distributed heterogeneously through the continuous component (oil). For spherical particles, Hanai [41] extended Boyle's mixture equation [42], where N=1/3. Hanai's mixture equation has proved to give excellent simulations for various colloidal dispersions over a wide range of volume fraction up to 0.8 [38]. Therefore, in this study the Hanai-Boyle mixture equation together with Peyman et al [43] equations were applied to determine the dielectric constant and dielectric loss of the water/oil (diesel) emulsion.

2.5.1 Maxwell-Wagner effect

One of the dielectric dispersion phenomena observed in heterogeneous systems is the interfacial polarization, also called Maxwell-Wagner relaxation. If the dispersed phase of a water-in-oil emulsion is conductive, dielectric dispersion and an increase in the static permittivity are expected. As shown in Figure 2.14, the relaxation frequency increases as the conductivity of the dispersed component increases [44]. By applying Hanai-Boyle mixture equation, the dispersion frequency for each conductive emulsion is easily found.

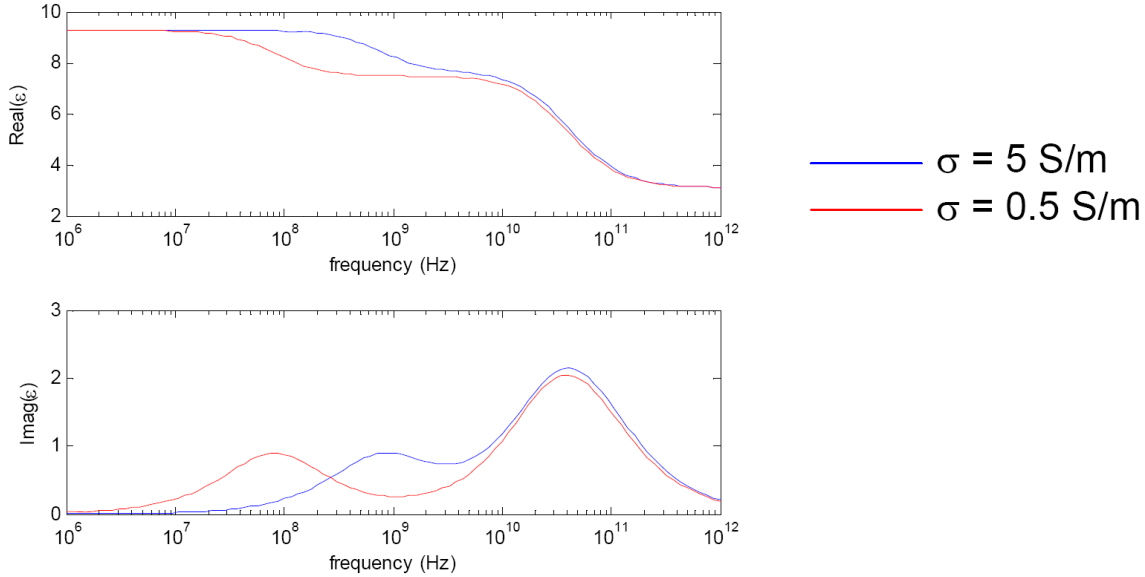

Figure 2.14: Dielectric constant and dielectric loss as examples of two emulsions with different conductivities [45].

2.5.2 Effect of temperature on conductivity

Peyman et al [43] derived an equation from which conductivity of a NaCl solution can be calculated as a function of temperature and concentration.

$$\sigma = 0.174tc - 1.582tc^2 + 5.923c \tag{73}$$

where t is the temperature of the fluid in degrees Celsius and c is the concentration of the solution in mole/litre.

In the next section the measurement procedure and the results are discussed.

3 Material and Methods

3.1 Test fluids

In total nine different test fluids with known permittivity were used in the first part of the experimental work. These include:

- Air
- Teflon
- Distilled water
- Ethanol
- Methanol
- Water/ethanol mixture x_e=0.22
- Water/ethanol mixture x_e=0.36
- Water/ethanol mixture x_e=0.54
- Water/ethanol mixture x_e=0.76

where x_e is the mole fraction of the ethanol.

In the second part of the experimental work another nine different fluids and emulsions, were prepared. These include:

- Diesel
- Water/diesel emulsion (Φ=20% and σ=0 [S/m])
- Water/diesel emulsion (Φ=20% and σ=0.1 [S/m])
- Water/diesel emulsion (Φ=20% and σ=0.5 [S/m])
- Water/diesel emulsion (Φ=20% and σ=1 [S/m])
- Water/diesel emulsion (Φ=20% and σ=1.5 [S/m])
- Water/diesel emulsion (Φ=20% and σ=2 [S/m])
- Water/diesel emulsion (Φ=20% and σ=2.5 [S/m])
- Water/diesel emulsion (Φ=20% and σ=3 [S/m])

Span80 was used as an emulsifier for preparation of water/diesel emulsions.

Four different models were implemented to calculate the frequency dependency of the permittivities of these media:

1. The constant permittivity model
2. The double Debye model
3. The Cole-Cole model
4. The Hanai-Boyle mixture model

The samples and permittivity models used in the experiments are summarized in Table 3.1 and Table 3.2.

Table 3.1: Literature data (Debye parameters) at 20°C for ethanol/water mixtures at different mole fractions x_e studied in this thesis [28].

Ethanol mole fraction	ε_s	$\Delta\varepsilon_1$	$\Delta\varepsilon_2$	τ_1 [ps]	τ_2 [ps]
x_e=1.00 (ethanol)	25.2	20.7	1.0	184	8
x_e=0.76	29.8	24.2	1.8	121	11
x_e=0.54	36.5	28.4	3.8	80	16
x_e=0.36	45.2	35.1	5.5	55	14
x_e=0.22	55.2	46.0	4.8	38	8

Table 3.2: Literature data (Cole-Cole parameters) at 20°C for the samples studied in this thesis [5].

Medium	ε_s	ε_∞	τ [ps]	α	Model
Air	1.00	1.00			constant
Teflon	2.10	2.10			constant
Methanol*	33.64	5.7	53	0.044	Cole-Cole
Water	80.21	5.6	9.36		Cole-Cole
Diesel	2.71	2.71			constant
Water/Diesel emulsion	3.96	3.96	9.36		Hanai-Boyle

*Gregory et al. [46]

3.1.1 Preparation of mixture of ethanol/water

The applied mole fraction of ethanol in the mixture (x_e) with its corresponding concentration of ethanol and water to make the desired mixture (c_w and c_e), are shown in Table 3.3. In this study, 0.3 litre of mixture was used. Knowing c_w, c_e and the desired x_e, the required weight of water and ethanol can be calculated using the following equation:

$$w_i\left[\text{gr}\right] = 0.3\left[\text{litre}\right] \times c_i\left[\frac{\text{mole}}{\text{litre}}\right] \times mw_i\left[\frac{\text{gr}}{\text{mole}}\right] \tag{74}$$

where w_i is the fluid weight in grams, mw is the molecular weight and i denotes either water or ethanol.

Table 3.3: Density *(ρ)* and concentrations of ethanol *(c_e)* and water *(c_w)* of the ethanol/water mixtures at different temperatures *T* and mole fractions x_e of ethanol [28].

$T \pm 0.05$, °C	$x_e = 0$ [71]	$x_e = 0.22$	$x_e = 0.36$	$x_e = 0.54$	$x_e = 0.76$	$x_e = 01$
			$\rho \pm 1.5$, mg/cm^3			
0	999.84	945.5	910.0	872.5	836.0	807.5
10	999.70	938.5	903.5	865.0	829.0	799.0
20	998.20	932.5	895.0	856.5	820.0	789.5
25	997.05	928.5	891.0	852.0	817.0	785.5
30	995.65	924.5	887.0	848.5	812.5	781.5
40	992.22	917.0	879.0	840.0	804.0	773.5
50	988.03	909.5	870.5	831.5	794.5	765.0
60	983.19	901.5	862.5	822.5	784.5	757.0
			$c_e \pm 0.02$, mol/L			
0	0	8.70	11.60	14.15	16.15	17.53
10	0	8.64	11.52	14.03	16.01	17.34
20	0	8.58	11.41	13.89	15.84	17.14
25	0	8.55	11.36	13.82	15.78	17.05
30	0	8.51	11.31	13.76	15.69	16.96
40	0	8.44	11.21	13.62	15.53	16.79
50	0	8.37	11.10	13.48	15.35	16.61
60	0	8.30	11.00	13.34	15.15	16.43
			$c_w \pm 0.02$, mol/L			
0	55.50	30.22	20.84	12.24	5.78	0
10	55.49	30.00	20.69	12.14	5.74	0
20	55.41	29.80	20.50	12.02	5.70	0
25	55.35	29.68	20.41	11.96	5.68	0
30	55.27	29.55	20.31	11.91	5.65	0
40	55.08	29.32	20.13	11.79	5.61	0
50	54.84	29.07	19.94	11.67	5.56	0
60	54.58	28.81	19.75	11.54	5.51	0

3.1.2 Preparation of the water/oil (diesel) emulsion mixture

Three calibration fluids were needed to measure the dielectric constant and dielectric loss of the mixture, i.e. pure diesel, an ethanol/water mixture with x_e=0.76 and a water/diesel emulsion with 20% water fraction. Due to the wear and tear of the original calibration kit of the network analyzer, an alternative calibration kit was used in this part of study. This calibration kit had a frequency range up to 9 GHz compared to a frequency range of 13.6 GHz of the original calibration kit.

An emulsion of water and oil (diesel) with a water fraction of 20% was prepared using Span80 as emulsifier for stabilization of the mixture. Standard diesel fuel was used in all the water/diesel emulsion investigations in these experiments. The non-ionic surfactant added to the mixture reduces the interfacial tension between the water and the diesel in order to produce the emulsion and to stabilize the water droplet phase within the continuous diesel fuel phase. The emulsion preparation procedure includes three steps, as follows. The first step is to mix the Span80 (1.0% volume of the mixture) and diesel (79% of the mixture) for two minutes using a laboratory high-speed mixer. Following, the water (20% of the mixture) is gradually added, while the mixture is being mixing. In the third step, mixing is done for 2 minutes and then the mixer is turned off for one minute and this third step operation is repeated 5 times [47]. As soon as the mixture was ready, it was poured into the beaker and the reflection coefficients S_{11} and S_{22} were measured using the small and the large probes, respectively. Thereafter, S_{11} and S_{22} for thick layer of ethanol water mixture x_e=0.76 was measured and subsequently for the thick layer of pure diesel. The measured parameters were used as calibration coefficients in the BCP. The calibration process was done using a water/diesel emulsion with a water fraction of 20%, diesel and an ethanol/water mixture with x_e=0.76.

In addition to the above, water/diesel emulsions (20% water) with different salinities were also prepared. The preparation procedure was the same as described above. The only difference is that a solution of distilled water and different concentrations of NaCl were used instead of distilled water. The dispersion frequency for the 7 different brine solutions were measured and plotted versus conductivity. Detailed information concerning these brine solutions is given in Table 3.4. While mixing the emulsion using the high-speed mixer, the temperature of the emulation is raised from room temperature to 30 – 36$^{\circ}C$.

Since the conductivity is temperature dependent the conductivity of the mixture will have an associated measurement uncertainty.

Table 3.4: Literature data according Hanai-Boyle mixture equation [38] and Peyman et al. equations [43].

No. of measurements	1	2	3	4	5	6	7
Salt [g/500ml]	0.29	1.38	2.71	4.86	6.52	7.90	9.10
Concentration [mole/litre]	0.010	0.047	0.93	0.166	0.223	0.271	0.311
Conductivity (35˚C) [S/m]	0.12	0.56	1.10	1.95	2.60	3.14	3.58
f_0 (35˚C) [MHz]	24.8	117	233	419	568	694	799
Conductivity (30˚C) [S/m]	0.11	0.52	1.02	1.81	2.41	2.90	3.31
f_0 (30˚C) [MHz]	23	106	211	382	516	630	726
Conductivity (36˚C) [S/m]	0.12	0.57	1.12	1.98	2.64	3.19	3.64
f_0 (36˚C) [MHz]	25	120	238	428	580	708	816

3.2 The open-ended probes

The two open-ended probes used in this work are modified commercially available coaxial couplings referred to in this work as the “large” probe and the “small’’ probe. Both probes were modified and cut at the Teflon level layer to ensure close contact between the measurement sample and the coaxial aperture. The large probe was coated with a thin layer of epoxy to avoid leakage into the connectors of the network analyzer. The effect of this coating is compensated for by using the BCP. The specifications of the probes are as listed in Table 3.5. The open-ended probes are mounted in a device which allows accurate adjustment of the fluid film thickness.

Table 3.5: Specification of the two open ended coaxial probes used in this work [48].

Probe	Type	a[mm] Outer radius of inner conductor	b[mm] Inner radius of outer conductor
Large	SUHNER 31N-716-50-1	2.75	8.9
Small	SUHNER 23N-50-0-23	1.54	4.87

The original sketch of the probes from the supplier (SUHNER Huber) catalogue before modification is shown in Figure 3.1.

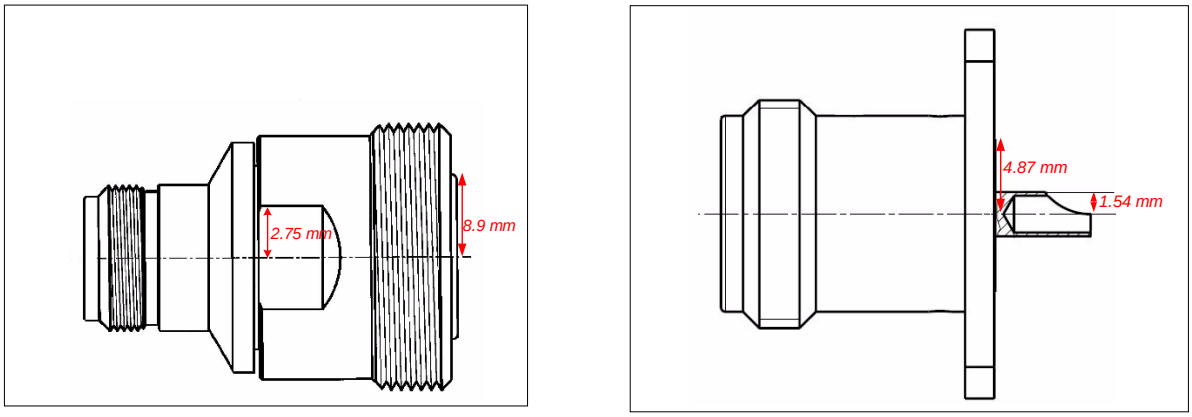

Figure 3.1: Sketch of lateral view of the unmodified SUHNER 31N-716-50-1 probe (left figure) and the unmodified SUHNER 23N-50-0-23 probe (right figure) [48]

3.2.1 Operating frequency range for the large and the small probe

Table 3.8 summarizes the corresponding frequencies for both the large and the small probes, in which the required operating condition can be met in terms of radiation onset, as well as applicability of a simple capacitance model.

Table 3.6: Frequency condition for the large and the small probes according to dimensions of the probes.

Probe	Minimum f_c for radiation	Maximum f_c for simple capacitance model
Large	$4.8/\sqrt{\varepsilon^*}$ GHz	8.2 GHz
Small	$9.0/\sqrt{\varepsilon^*}$ GHz	14.9 GHz

As given in Table 3.6, the corresponding minimum radiation frequency for the large and the small probes are reported to be $4.8/\sqrt{\varepsilon^*}$ and $9.0/\sqrt{\varepsilon^*}$ GHz, respectively. The simple capacitance model fails at frequencies higher than 8.2 and 14.9 GHz for the large and the small probes, respectively. Table 3.7 summarizes the frequency condition for the large and the small probe according to the permittivity of the SUT.

Table 3.7: Frequency condition for the large and the small probes according to the permittivity of the SUT.

Compound	Large probe		Small Probe	
	$f_{min.\text{radiation}}$ (GHz)	$f_{min\cdot\text{failure}}$* (GHz)	$f_{min\cdot\text{radiation}}$ (GHz)	$f_{min\cdot\text{failure}}$ * (GHz)
Air	4.8	8.2	9.0	14.9
Teflon	3.3	8.2	6.2	14.9
Methanol	0.8137	8.2	1.52	14.9
Water	0.536	8.2	1.00	14.9
Ethanol	0.9007	8.2	1.79	14.9
Ethanol/Water x_e=0.76	0.8793	8.2	1.64	14.9
Ethanol/Water x_e=0.54	0.7945	8.2	1.49	14.9
Ethanol/Water x_e=0.36	0.714	8.2	1.33	14.9
Ethanol/Water x_e=0.22	0.646	8.2	1.21	14.9

* $f_{min\cdot\text{failure}}$ is the minimum frequency at which the simple capacitance model fails.

3.2.2 Probe sensitivity as a function of frequency and permittivity

The sensitivity of an open ended coaxial probe is dependent on the dimension of the probe, the frequency, the apparent permittivity of the fluid being examined and its thickness. To achieve satisfactory measurement sensitivity, the probe selection should be done carefully, i.e. with respect to both the permittivity and the operating frequency. A probe with a large aperture is sensitive at lower frequencies and permittivities. Applying the expression of reflection coefficient (equation 38) and assuming the linear capacitance model (equations 58 and 59), the normalized sensitivity of the probe can be derived as:

$$S(f) = \left| \frac{\varepsilon}{\Gamma(\varepsilon, f)} \frac{\partial \Gamma(\varepsilon, f)}{\partial \varepsilon} \right| \tag{75}$$

where Γ is the reflection coefficient as a function of apparent permittivity (ε) and frequency (f). According to equations 58 and 59, the calculated C_0 using the electrostatic model of Fan and Misra for both the small and the large probes are $1.68\times10^{-13}F$ and $2.74\times10^{-13}F$, respectively [19].

As Figure 3.2 shows, in order to obtain satisfactory sensitivity for the small probe at low permittivities, the measurement frequency should be relatively high. An alternative is, however, to use a larger probe where the three curves will shifted toward the left. The frequency shift is dependent on the increased dimension of the larger probe. As an example, in case of a permittivity value of 25 (blue curve), the large probe is more sensitive at an operating frequency around 450 MHz; while the small probe becomes more sensitive at an operating frequency around 720 MHz as the black arrow indicates in Figure 3.2.

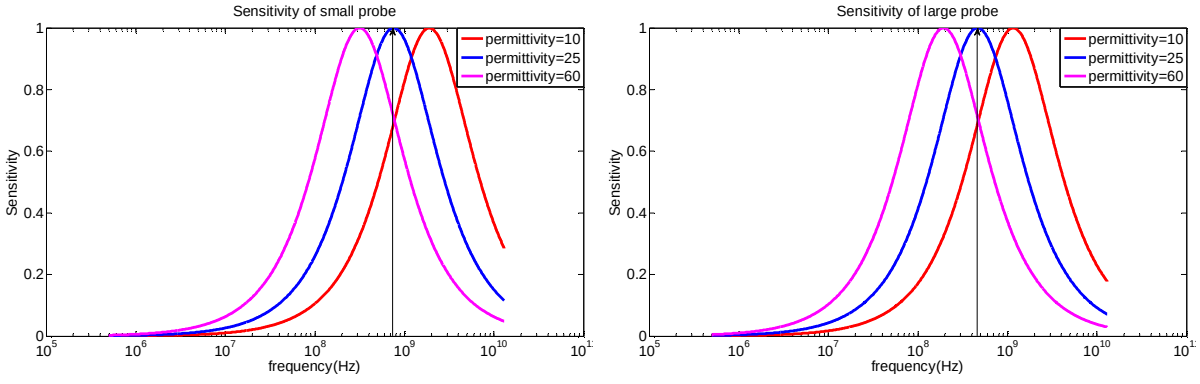

Figure 3.2: The sensitivity of the small and the large probes as a function of frequency and permittivity.

3.3 Permittivity measurement setup

The permittivities of the different fluids were measured inside a measurement cell, as schematically illustrated in Figure 3.3. In this setup, the Teflon part was used to represent gas in the annular flow regime, and by adjusting the height of the Teflon part from zero level, the thickness of the SUT is controlled.

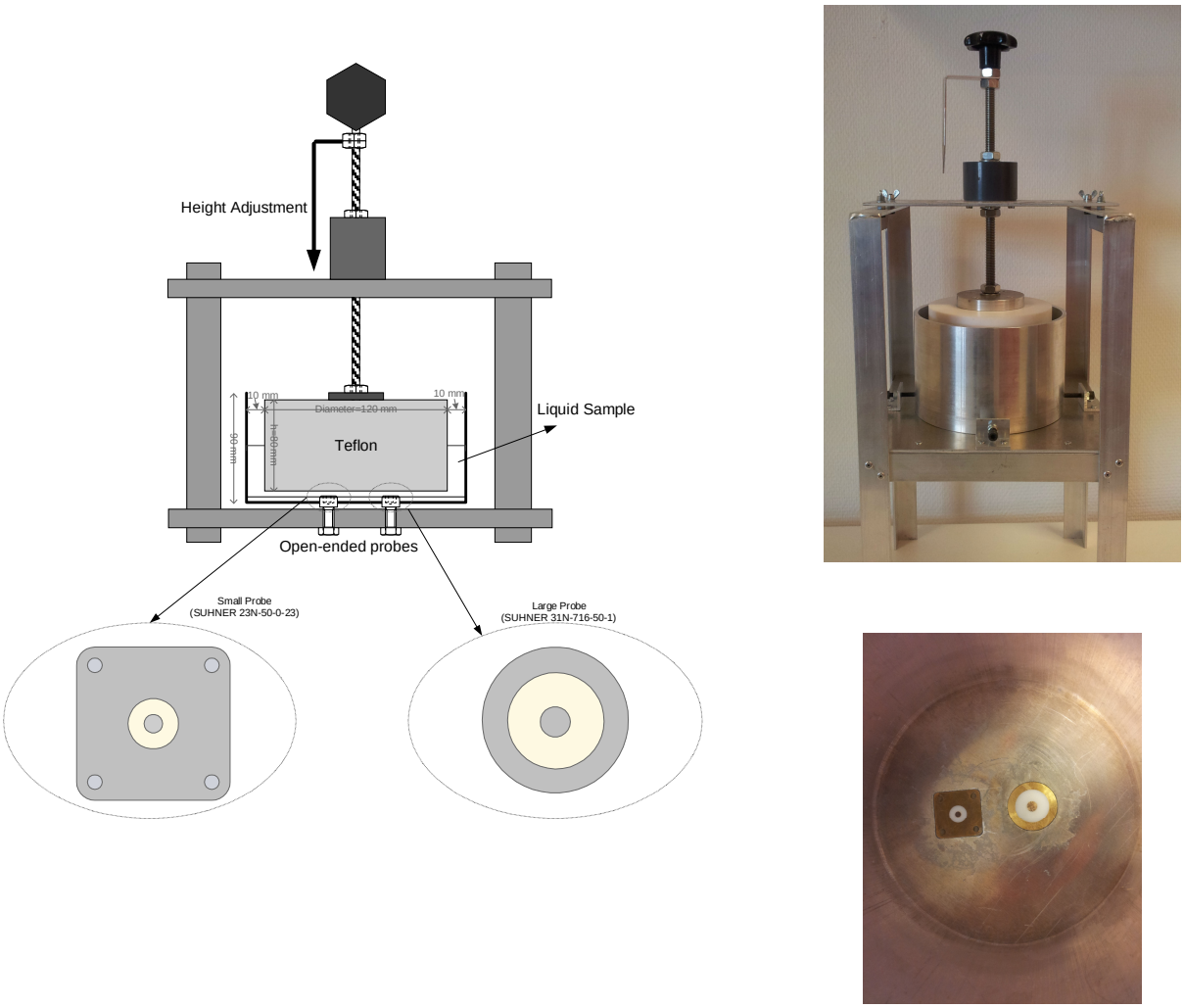

Figure 3.3: Schematic and photograph of the test device for adjustment of fluid film thickness. The permittivity of the fluid film is measured using two open ended coaxial probes.

Based on height measurements done manually on the height adjustment system, the measurement uncertainty of the height adjustment system is considered to be ± 0.11 mm. The two open ended probes were rigidly mounted in the bottom of the beaker, which has an inner diameter of 140 mm, a height of 90 mm and a wall thickness of 4.8 mm. Two holes were drilled in the beaker and the probes were mounted using flanges inside the

beaker. The beaker was screwed onto a box to minimize measurement errors that could be introduced through cable movement between the time of calibration and measurement. A micrometer adjustment system was mounted on a bridge installed on the top of the box, which makes it easy to clean the beaker after each experiment. The micrometer adjustment system was connected to a Teflon cylinder with a diameter of 120 mm and height of 80 mm. Since the permittivity of Teflon and air are relatively close i.e. 2.1 and 1, respectively, Teflon is considered to be a suitable backing material to represent the gas component in annular flow of wet gas. This setup allows the Teflon backing material to be moved in steps of 0.75 mm within a displacement range of 0 to 21 mm. In total, 29 different measurements were obtained for each of the sample fluids. In order to achieve higher accuracy in the thickness adjustment system, an arrow/ full circle protractor (360 degrees) was used on the top of the box to ensure that for each step the arrow moves 180 degrees.

Figure 3.4 illustrates how the permittivity measurement chamber is connected to a network analyzer and a laptop computer, where the acquired measurement data is displayed and stored. For safety reasons the measurement chamber is placed within a ventilation cabinet. All experiments were performed at room temperature (~20 $^{\circ}$C), where the temperature was monitored carefully to detect any sudden changes. The sample beaker was washed and dried after each experiment, i.e. before changing test fluid. During the experimental works, the beaker was fixed to the box using two holders to avoid the beaker jumping up. A horizontal level indicator was also used to ensure that the beaker position did not change.

During data analysis of the original measurement setup, it was found that for zero thickness there was a small void between the surface of the small probe and the surface of the Teflon material. This mechanical inaccuracy will induce measurement error in the low thickness measurements. Therefore, a modified set up was introduced by removing the Teflon part connected to the height adjustment system. Thickness control was done using a 20 ml syringe. While knowing the volume of the beaker, during each incremental thickness step of the SUT, 11 ml of the fluid was added to the fluid volume inside the beaker.

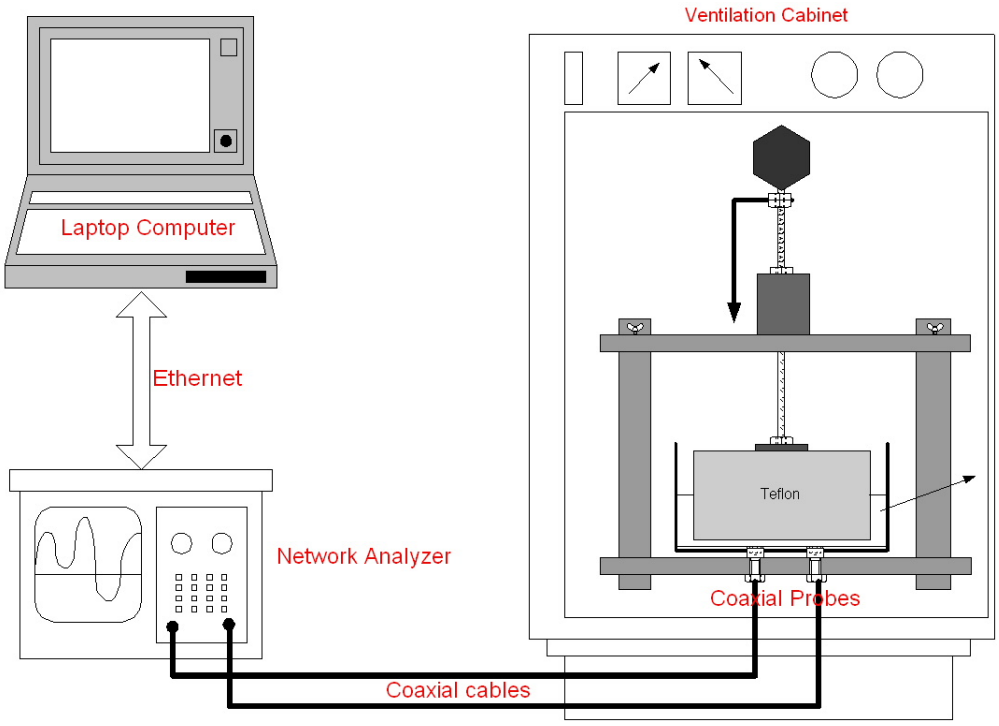

Figure 3.4: Schematic of the experimental setup and electrical connections including the network analyzer and the computer.

The measurements were performed using a Rohde & Schwarz ZVL Network Analyzer, which measures the electromagnetic reflection coefficient of an open-ended probe/fluid interface. The acquisition of data between the network analyzer and the laptop computer was conducted by a computer program written in the C language. The network analyser was controlled via a PC using the Ethernet (LAN) interface. The measured data, as shown in Figure 3.4, was transferred to the laptop computer for analysis and further processing using Matlab software tool.

In order to acquire accurate permittivity measurements in the microwave region, it is important to use high quality cables and connectors. Special care was taken to avoid any changes to the measurement system between the time of calibration and the time of experimental measurements since temperature variations and/or cable movements can introduce perturbations to the systematic errors not accounted for by the calibration procedure. Uncorrected perturbations will result in errors in the permittivity measurements. During calibration, as well as during the procedure of connecting the probes to the cables, the connectors and probes should be handled as stable as possible to prevent twisting. Any small mechanical change in the connections will introduce significant errors in the

measurement data. Therefore, the experimental setup should not move during the experiments. Also, the introduction and removal of fluid should be done without moving the experimental setup by using a syringe and drying paper. The calibration of the network analyzer is usually performed using a standard calibration kit. The calibration kit used here is an “open-short-match-thru”. “Open-short-match” calibrations are done separately for each of the ports, but there is no need for “thru” calibration for reflection measurements. All measurements must be performed with a common calibration to achieve high accuracy. Having 29 different thicknesses of fluids, each measurement will results in 1601 sample points distributed logarithmically within the frequency range of 10 MHz – 13 GHz.
The equipments used in the experimental work are as summarized in Table 3.8.

Table 3.8: Experimental equipments used in the experimental work.

Device Type	Model
Network analyzer	Rohde & Schwarz ZVL Network Analyzer
Laptop computer	Dell Latitude E5500
Cables (2 Pcs.)	Rohde & Schwarz ZV-Z191
Calibration kit	Rohde & Schwarz ZV-Z132 CAL KIT
Digital weight	Mettler Toledo Excellence
High speed laboratory emulsifier mixer	Silverson L2R heavy duty

Langhe and Martens [18] reported that if the thickness of the material is about twice that of the outer radius of the probe, it acts like infinite thickness, regardless of the size of the probe and the permittivity of the fluid to be measured. In order to ensure that the probe faces infinite thickness, the thickness of the fluid sample should be larger than about one to two times the outer radius of the probe [35]. The outer radius of the large probe is 8.9 mm, and according to the dimensions of the fluid beaker and Teflon part, a sample fluid volume of 0.3 litre should be sufficient to make sure that when the Teflon part is in its highest position, the infinite thickness ($2R$=17.8 mm) is obtained.

4 Results and discussions

The objective of this work was to examine the applicability of a dual probes system for permittivity and the liquid layer thickness measurement within sufficient accuracy that can be applied ultimately for hydrate monitoring. In this chapter the following experimental procedures are presented in order to fully investigate the possibility of the study objective. Thereafter, the feasibility of the coaxial probes for conductivity measurements is investigated.

4.1 Characterization of the measurement system

As mentioned in section 2.3.6, when conducting the BCP, three known permittivity fluids, called calibration fluids, are needed to determine the calibration coefficients. In order to perform the measurements with high precision, and to avoid extrapolation, two different calibration fluids with high and low permittivity values are used to cover the full permittivity range, and a reference fluid with a permittivity close to that of the unknown sample were selected.

4.1.1 Choice of calibration and test fluids

Through a series of calibration procedures, as shown in Figure A.1 to Figure A.7 in appendix A, an attempt was made to find a desired set of calibration fluids (air, distilled water, ethanol, methanol and Teflon) to obtain the highest measurement accuracy. However, none of the calibration fluids used turned out to be useful due to ripple in the calculated response, noise, large deviations from literature values, etc, as addressed below.

Since the permittivity of air and Teflon are close to each other, no significant difference will be observed between Figure A.1 and Figure A.2. The permittivity of air is not in the range of the calibration fluids and therefore the measurement accuracy is a bit lower than the case in which the permittivity of the unknown fluid is between the permittivity of the calibration fluids. In case of three calibration fluids (air, Teflon, methanol) and ethanol as the unknown fluid, since the permittivity of air and Teflon are close to each other this combination doesn't lead to satisfactory results (Figure A.5).

When using distilled water as the calibration fluid radiation occurs, especially for the large probe in the high frequency range (Figure A.6 and Figure A.7). In order to eliminate this radiation, the high permittivity fluid should be replaced by a fluid with medium permittivity, e.g. a mixture of ethanol/water with known mole fraction of ethanol. In the following some additional permittivity fluids are consequently introduced and analyzed.

Table 4.1: Summary of calibration fluid combinations and unknown fluids and corresponding results.

Fig.#	Calibration fluids	Test fluid	Comments
Figure A.1	Air, ethanol, methanol	Teflon	No significant change from Figure A.2, Radiation by the large probe at frequency more than 0.8 GHz due to methanol
Figure A.2	Teflon, ethanol, methanol	Air	Extrapolation beyond calibrated permittivity range due to Teflon
Figure A.3	Air, DW[(1)], methanol	ethanol	Radiation by the large probe at frequency more than 0.5 GHz due to distilled water, resonance effect by the large probe
Figure A.4	Air, DW, ethanol	methanol	Radiation by the large probe at frequency more than 0.5 GHz due to distilled water, resonance effect by the large probe
Figure A.5	Air, methanol, Teflon	ethanol	Radiation at frequency more than 0.8 GHz due to methanol
Figure A.6	DW, methanol, Teflon	ethanol	Radiation by the large probe at frequency more than 0.5 GHz due to distilled water, resonance effect by the large probe
Figure A.7	DW, ethanol, Teflon	methanol	Radiation by the large probe at frequency more than 0.5 GHz due to distilled water, resonance effect by the large probe
Figure A.8	Air, DW, EW54[(4)]	methanol	Radiation due to distilled water, resonance effect by both probes
Figure A.9	Air, DW, EW54	ethanol	Radiation due to distilled water, resonance effect by both probes
Figure A.10	Air, DW, EW36[(3)]	methanol	Radiation due to distilled water, resonance effect by both probes
Figure A.11	Air, EW36, DW vs. EW76[(5)]	methanol	Less radiation in the absence of distilled water
Figure A.12	Air, EW36, DW	ethanol	Radiation due to distilled water, resonance effect by both probes
Figure 4.1	Air, EW54, DW vs. EW76	ethanol	Less radiation in the absence of distilled water
Figure A.13	Air, EW22, EW36	ethanol	Resonance effect in the high frequency range, variation from literature
Figure A.14	Air, DW, EW54	methanol	Not in agree with literature values
Figure A.15	Air, DW, EW54	ethanol	Resonance effect and radiation due to distilled water
Figure A.16	Air, DW, EW76	methanol	Not in agreement with literature values
Figure A.17	Air, DW, EW76	ethanol	Resonance effect and radiation at high frequency
Figure A.18	Air, EW36, EW76	methanol	Not in agree with literature values
Figure A.19	Air, EW36, EW76	ethanol	Resonance effect in the high frequency range
Figure A.20	EW22, EW54, EW76	EW36	Satisfactory result but extrapolation in low thicknesses
Figure A.21	EW76, EW22, EW36	EW54	Satisfactory result but extrapolation in low thicknesses
Figure 4.4	EW54, ethanol, EW36	EW76	Good combination but extrapolation in low thicknesses
Figure 4.5	**Air, ethanol, EW54**	**EW76**	**The best combination used, not in agreement with literature values**
Figure A.22	Air, EW36, EW54	methanol	Not in agreement with literature values
Figure A.23	Air, EW36, EW54	EW76	Not smooth spectra

[(1)]DW: Distilled Water

[(2)]EW22: Ethanol/water mixture x_e=0.22

[(3)]EW36: Ethanol/water mixture x_e=0.36

[(4)]EW54: Ethanol/water mixture x_e=0.54

[(5)]EW76: Ethanol/water mixture x_e=0.76

The combinations of the above mentioned fluids (air, distilled water, ethanol, methanol and Teflon) did not provide a suitable set of calibration fluids. In order to obtain a better range of permittivity values, different mixtures of ethanol/water with known ethanol mole fractions were used in combination with previous fluids, either as the calibration fluids or the unknown fluids. Table 4.1 summarizes some of fluid combinations with respect to the results shown in the corresponding figures.

As an example, Figure A.8 and Figure A.9, respectively, show the dielectric constant and the dielectric loss measurements for methanol and ethanol as unknown fluids, and the three calibration fluids that are air, ethanol/water mixture x_e=0.54 and distilled water. It is interesting to see that in the case of ethanol as the unknown fluid, the permittivity measured in the low frequency range with the small probe is higher than that measured with the large probe. This is completely in contrast to the case of methanol, where the large probe measures higher permittivity. In the case of the distilled water as one of the calibration fluids, especially in the high frequency range, radiation emerges and the dielectric spectrum does not behave smoothly. The behaviour of distilled water as the fluid possessing the highest permittivity is poor. As defined by equation 64, the radiation conductance term (first term) acts strongly for distilled water especially in the high frequency range. Therefore, by using a mixture of ethanol/water x_e=0.76 instead of distilled water, better results should be expected. For simplicity, short comments are given in Table 4.1 concerning the rest of the fluid combinations.

Figure 4.1 shows the measured permittivity of ethanol with two different sets of calibration fluids. In Figure 4.1(a), one of the calibration fluids is distilled water, whereas in Figure 4.1(b) distilled water is replaced with ethanol/water mixture x_e=0.76. As shown here, the behaviour by the both probe are in agreement with the above justification in which the dielectric spectrum behaves more smoothly in the absence of distilled water as a calibration fluid. A similar conclusion can also be made from Figure A.11 in Appendix A.

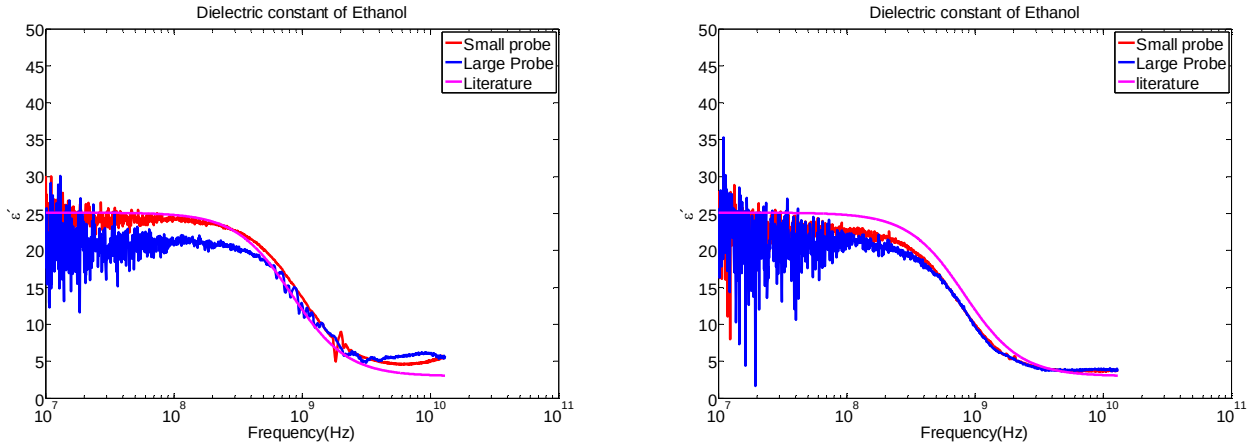

(a) (b)

Figure 4.1: Estimated dielectric constant of ethanol with two different calibration sets. The three calibration fluids in figure (a) are: air, distilled water and ethanol/water mixture x_e=0.54 while in figure (b) distilled water is replaced with ethanol/water mixture x_e=0.76.

In the case of methanol as the test fluid, the measured permittivity shows a deviation from the reported permittivity values in literature [46], as shown in Figure 4.2; although they are in good agreement with the results reported by Kjetil Haukalid [49], however his results are not shown here.

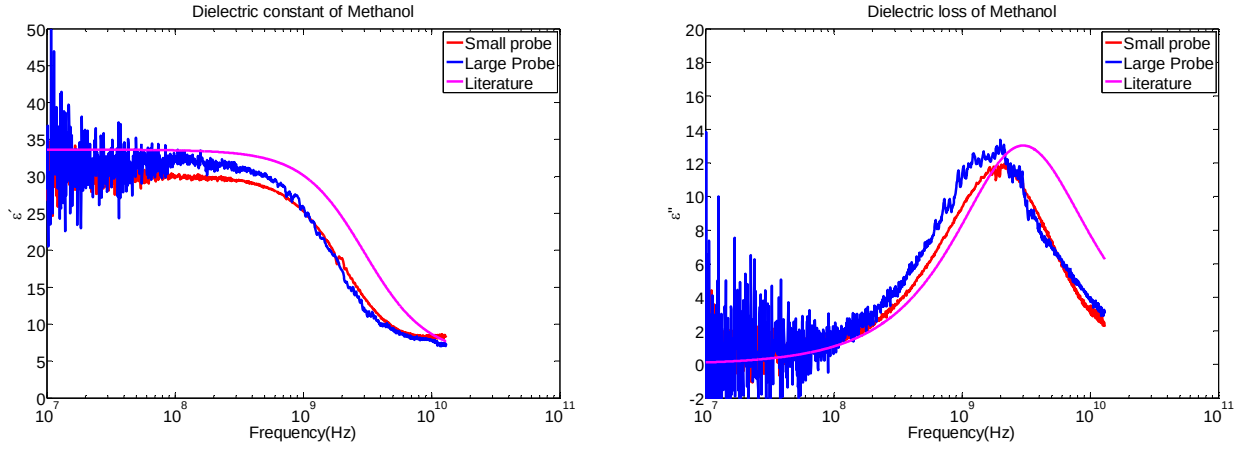

Figure 4.2: Estimated dielectric constant and dielectric loss of methanol when the three calibration fluids are: air, distilled water and ethanol/water mixture x_e=0.54.

In Figure 4.3, in the low frequency range the large probe has much more noise than the small probe, however in the high frequency range both probes give smooth spectra. This is

in contrast to the results reported by Jakobsen and Folgerø [2], which indicate a better performance of the small probe in the high frequency range and of the large probes in the low frequency range. The reason for the poor behaviour of the large probe might be that the modification procedure was not done well enough, e.g. maybe some leakage exists through the connectors and/or the commercially available probe may be cut along the wrong cross-section. It is difficult to find any other reasonable explanation to the poor detecting behaviour of the large probe.

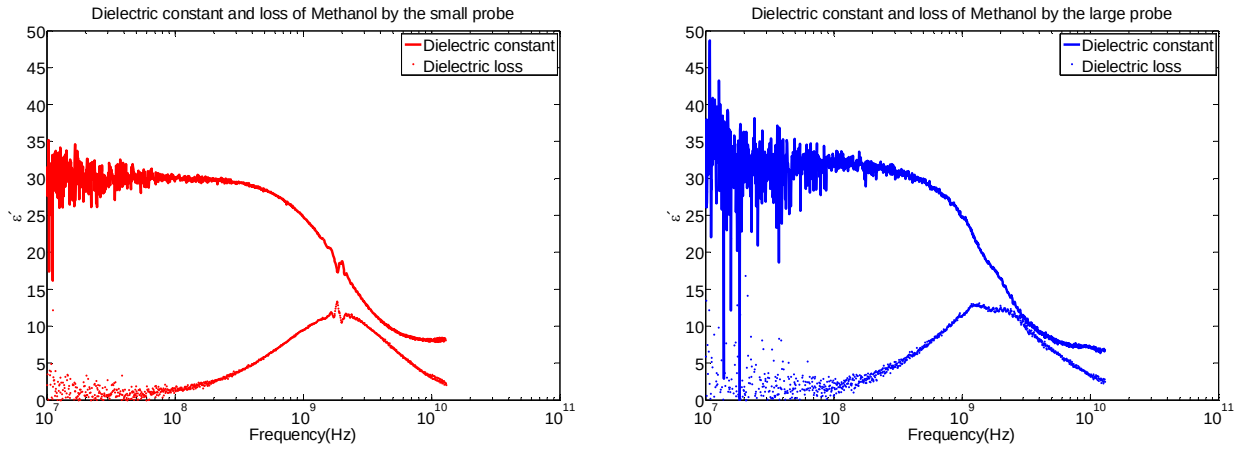

Figure 4.3: Estimated dielectric constant and dielectric loss of methanol by the small (left figure) and the large probes (right figure). The three calibration fluids are: air, ethanol/water mixture x_e=0.36 and ethanol/water mixture x_e=0.54 for the both probes.

In general, the small probe gives smoother frequency spectra with less noise for almost all combinations of calibration fluids and test fluids. After these investigations made, ethanol/water mixture x_e=0.76 with calibration fluids including ethanol and two ethanol/water mixtures possessing ethanol mole fraction of 0.36 and 0.54, seem to be the most desirable fluid combination. As seen in Figure 4.4, the measured permittivity using both probes are in agreement with the permittivity given in literature of ethanol/water mixture x_e=0.76 within the frequency range (pink line). The only challenge with this combination is that in low thicknesses of ethanol/water mixture x_e=0.76, when the apparent permittivity is less than the permittivity of ethanol (=25.2 [5]) as one of the calibration fluids, an extrapolation beyond the calibrated permittivity range occurs.

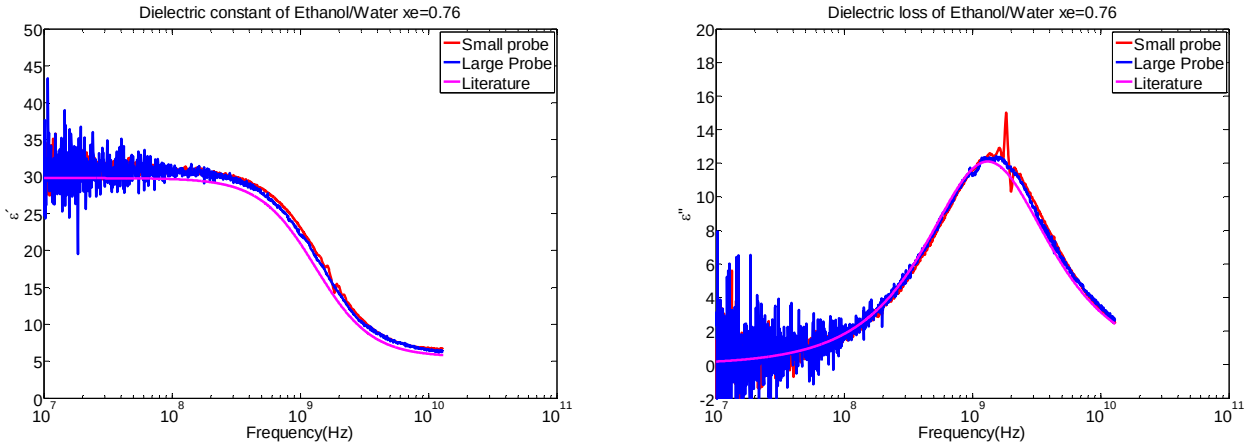

Figure 4.4: Estimated dielectric constant and dielectric loss of ethanol/water mixture x_e=0.76 when the three calibration fluids are: ethanol, ethanol/water mixture x_e=0.36 and ethanol/water mixture x_e=0.54.

Figure A. 24 and Figure A.25 also show the apparent permittivity of different thicknesses of ethanol/water mixture x_e=0.76 of the small and the large probe, where the apparent permittivity extrapolates beyond the calibrated permittivity range for thickness less than 3.75 and 6 mm for the small and the large probes, respectively. For small thicknesses, unexpected noise is observed for both the large and the small probes, as well. All measurements were done within the frequency range of 10 MHz – 13 GHz, and each measurement consisted of 1601 samples (points) taken over the entire frequency range. A moving average technique was applied to find the mean value for each subsequent 5 samples, which reduces the measurement uncertainty.

One of the objectives of this work was to measure thickness, and air was chosen as the low permittivity fluid to avoid extrapolation beyond the calibration permittivity range for low thickness measurements i.e. zero thickness. For thin layers of an ethanol/water mixture x_e=0.76, the apparent permittivity is lower than the permittivity of all calibration fluids, except air. In another words, the apparent permittivity of a thin layer of the SUT extrapolates beyond the calibration range. Therefore, the error in measured apparent permittivity will increase. Hence, for thickness measurements one of the calibration fluids should be air to avoid extrapolation in zero thickness of fluid.

Figure 4.5 shows the dielectric constant and dielectric loss of an ethanol/water mixture x_e=0.76 when the calibration fluids are air, ethanol and ethanol/water mixture x_e=0.54. The permittivity spectrum for the small and the large probes are in agreement with each other,

but some systematic deviation exists when compared to the literature values, which may be caused by deviations in temperature or impurities in the sample or calibration fluids. The instrumentation system may be another source of systematic errors. Hereafter, this combination is referred to as the best calibration set.

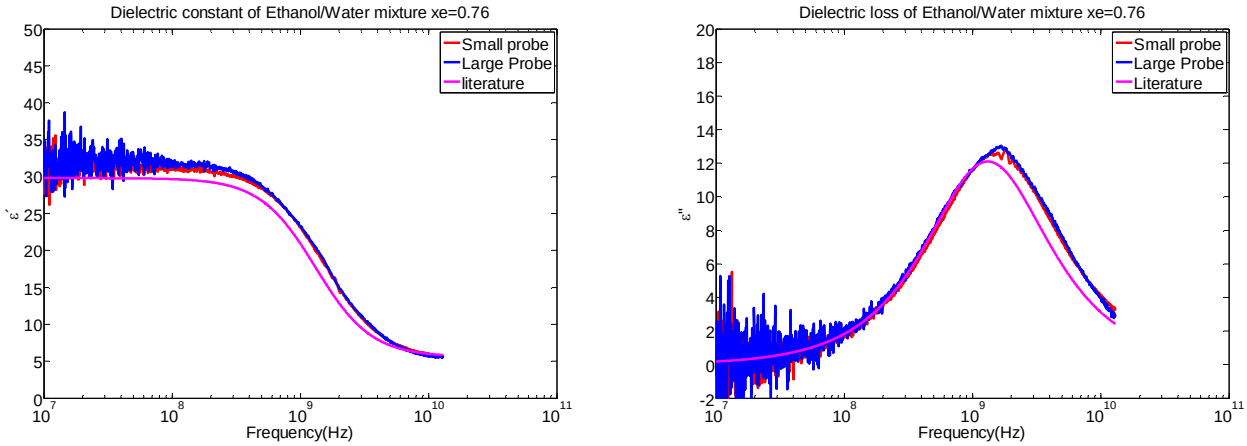

Figure 4.5: Estimated dielectric constant and dielectric loss of ethanol/water mixture x_e=0.76 when the three calibration fluids are: air, ethanol and ethanol/water mixture x_e=0.54.

For the investigation of sensitivity depth, probe constant and thickness measurement experiment, an ideal calibration set is introduced as ethanol/water mixture x_e =0.76 when the calibration fluids are air, ethanol and ethanol/water mixture x_e=0.76. Since one of the calibration fluids is the same as the SUT that is in practice not applicable. Hereafter, the combination of ethanol/water mixture x_e=0.76 when the calibration fluids are air, ethanol and ethanol/water mixture x_e=0.76, is referred to as the ideal calibration set.

In next part of the thesis the reproducibility of the small and the large coaxial probes are investigated. Following, the static permittivity of the SUT for different thickness is determined.

4.1.2 Reproducibility of permittivity measurements

Many factors influence on the measurement uncertainty of the measured permittivity. The factors considered in this work are reported to be the uncertainties in the measured impedances and the reflection coefficients, the literature values of the permittivity of the fluids used for calibration and the impurities in the sample or calibration fluids. Other

factors such as temperature instability, uncertainty in the temperature measurements and the effects not accounted for by calibration routine, can be also taken into account in terms of measurement uncertainties. To reduce the instrumentation uncertainties, the measurement system must be stable during the experiment. The reproducibility of the measurement system was estimated using the ethanol/water mixture x_e=0.76 with the so-called best calibration set at 20°C for 40 consecutive measurements at an interval of approximately 5 minutes.

The spectra were measured with both probes within the frequency range of 10 MHz – 13 GHz. The standard deviation of the repeated measurements for the large probe is less than 2 and for the small probe is around 1.2 within the investigated frequency range as shown in Figure 4.6 and Figure 4.7, respectively. The small probe provides more stable results than the large probe. Both the dielectric constant and the dielectric loss reproducibility results indicate a stable temperature and low instability of implemented instrumentation system.

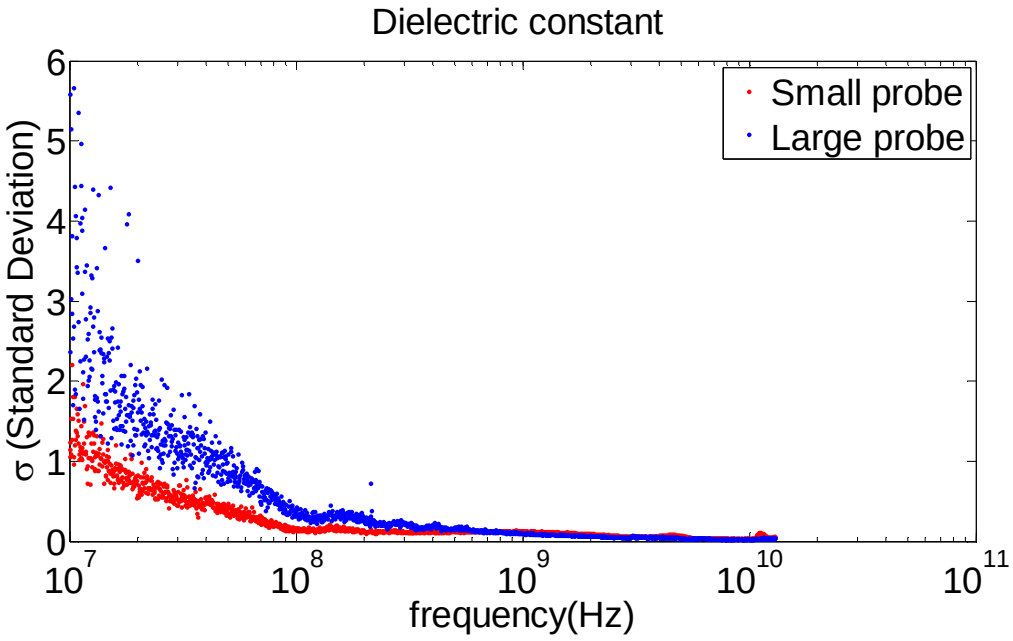

Figure 4.6: The standard deviation for the dielectric constant in 40 consecutive measurements of ethanol/water mixture x_e=0.76 within the frequency range of 10 MHz–13 GHz for the large and the small probes.

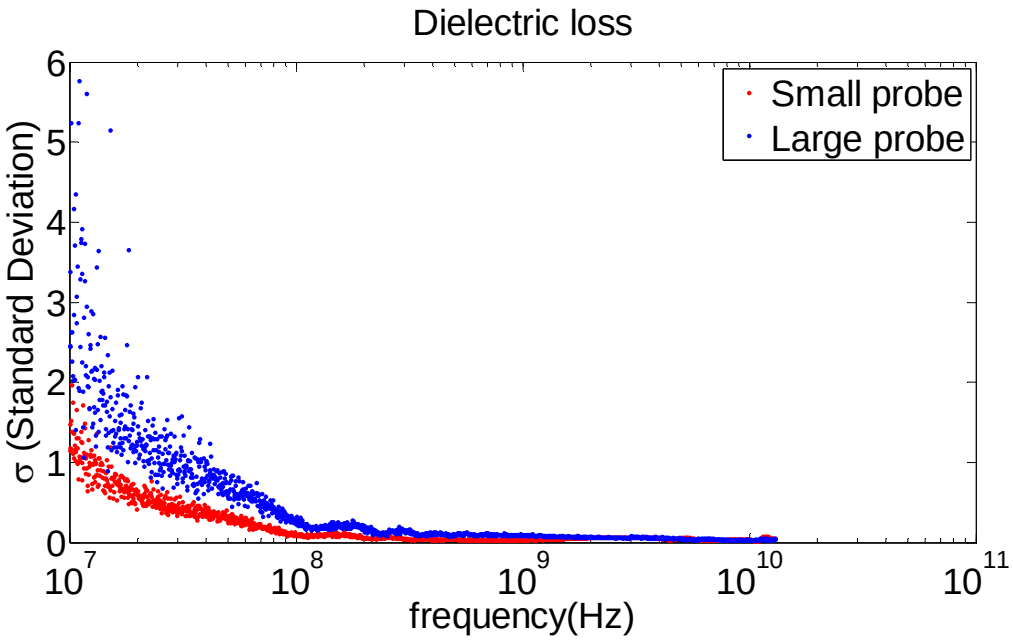

Figure 4.7: The standard deviation for the dielectric loss in 40 consecutive measurements of ethanol/water mixture x_e=0.76 within the frequency range of 10MHz – 13 GHz for the large and the small probe.

As summarized in Table 4.2, the maximum standard deviation for the dielectric constant in the high frequency range for the large probe is approximately 3.6 and for the small probe is 1.45 and at frequencies higher than 50 MHz, the measurement uncertainty of the dielectric constant is less than one. In Table 4.2 the maximum standard deviation for the both probes at different frequency intervals are presented based on moving average calculation for each 5 consecutive samples.

Table 4.2: Maximum standard deviation for the small and the large probes within the different frequency intervals.

Frequency	Standard deviation for dielectric constant		Standard deviation for dielectric loss	
	Small Probe	Large Probe	Small Probe	Large Probe
10 MHz – 20 MHz	1.45	3.6	1.4	3.2
20 MHz – 50 MHz	0.9	1.9	0.7	1.5
50 MHz – 100 MHz	0.4	0.9	0.4	0.8
100 MHz – 13 GHz	0.3	0.2	0.1	0.3

Here, during determination of the sensitivity depths and the probes constants, it has been assumed that one of the calibration fluids is the same as the SUT (i.e. ideal calibration set). As long as both the probes are calibrated with air and the same fluid as the SUT, it is guaranteed that the measured apparent permittivity by the large and the small probe for zero and infinite thickness layer of the SUT will converge at the same value. Therefore, it will be easier to investigate the probes' constants and their sensitivity depths by using the empirical models of the probes. This method of selecting calibration fluids will compensate for all kinds of inequalities in both probes, for zero and infinite thickness of the SUT. By selecting air as a calibration fluid, in addition to avoid extrapolation in low thicknesses, the measured permittivity by both probes at zero thickness (air) is approximately 1, and by selecting the SUT as another calibration fluid, the measured permittivity by both probes for infinite thickness is approximately equal to the permittivity of the SUT.

4.1.3 Comparison of test setups for layer measurements

Due to mechanical inaccuracy of the Teflon part, using the original measurement setup introduces a mechanical offset for low thicknesses and some fluctuation (noise) in the low frequency range, whereas in the absence of the Teflon part in the so-called modified setup, these fluctuations are not observed. In this part of the study the possible effects of the absence or the presence of the Teflon part in the measurement system are investigated, where the ethanol/water mixture x_e=0.76 is the SUT with the ideal calibration set.

The first investigation was done using Teflon. Figure 4.8 and Figure A.26, demonstrate the dielectric constant and loss of an ethanol/water mixture (x_e=0.76) within the frequency range of 10 MHz – 13 GHz using the ideal calibration set, where the small probe is applied. For the large probe, the corresponding results are shown in Figure 4.9 and Figure A.27. The fluctuation in the low frequency range can be clearly seen in the above-mentioned figures. As shown, the film thickness of the mixture varies from 0 to 21 mm for increasing steps of 0.75 mm. Thickness control is performed by adjustment of the Teflon part. By moving the Teflon part upward or downward, the distance from the bottom of the beaker (the surface of the probes) will increase or decrease accordingly, hence changing the fluid thickness.

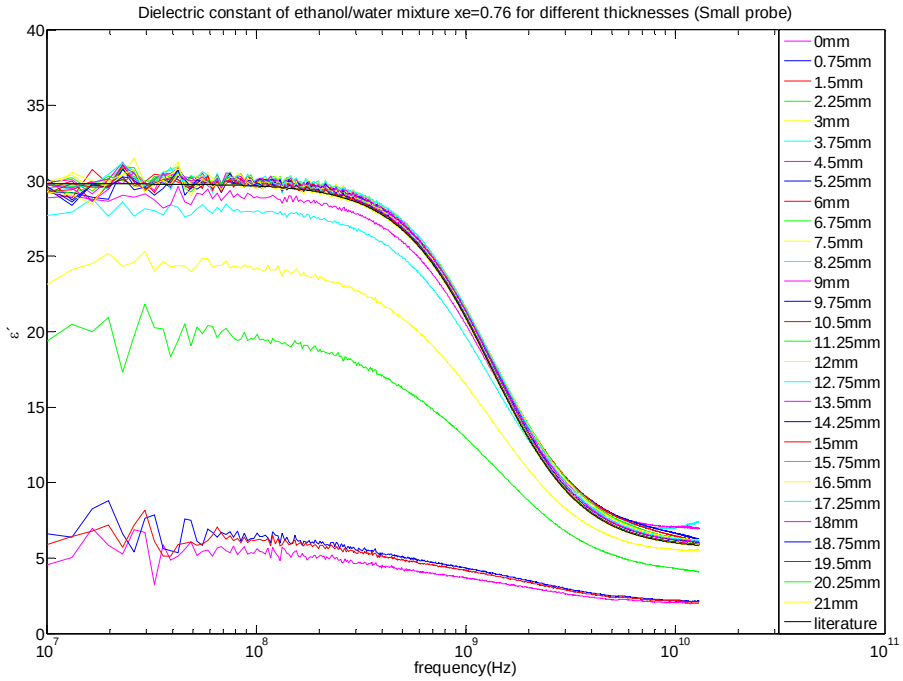

Figure 4.8: Dielectric constant of ethanol/water mixture x_e=0.76 versus frequency for different thicknesses of test fluid with using the Teflon part (small probe) with the ideal calibration set.

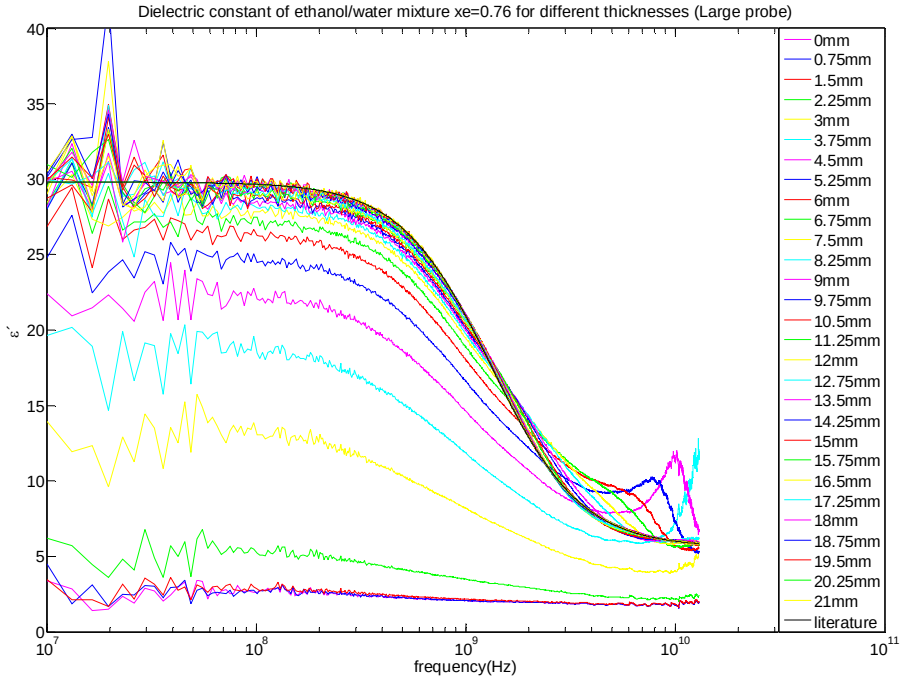

Figure 4.9: Dielectric constant of ethanol/water mixture x_e=0.76 versus frequency for different thicknesses of test fluid with using the Teflon part (large probe) with the ideal calibration set.

The dielectric constant of Teflon is reported to be 2.1 [5] with no dispersion within the working frequency range of this study, whereas in Figure 4.8 it is seen that for a layer thickness of zero (pink line), the measured permittivity by the small probe is not constant and approximately 5 in the low frequency range. Since one of the calibration fluids is air, there is no possibility for extrapolation beyond the calibration range. The measured permittivity for layers with thicknesses of 0.75 mm and 1.5 mm does not increase significantly from the permittivity of the actual zero thickness. Figure 4.9 shows that for layers thinner than 1.5 mm (actual thickness), the large probe measures almost the same permittivity as zero thickness of fluid (Teflon). It should be noted that there is a tiny space between the Teflon and the small probe filling with fluid when the Teflon part is at its lowest position. On the other hand, the thickness of the fluid in the vicinity of the large probe does not change for actual thicknesses less than 1.5 mm due to the squeezing effect. Figure 4.10 clearly demonstrates the inaccuracies of the experimental setup.

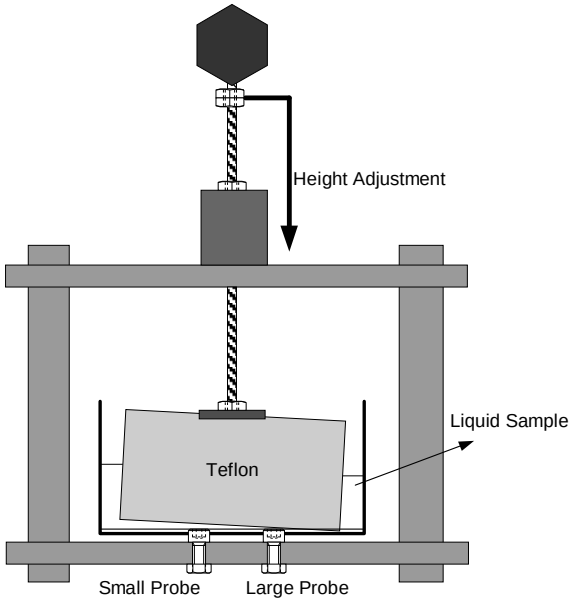

Figure 4.10: Experimental setup when the Teflon part is in its lowest level with exaggerated inaccuracy.

In this part of the study, similar investigations were made as above but in the absence of the Teflon part. The dielectric constant of an ethanol/water mixture x_e=0.76 is shown in Figure 4.11 and Figure 4.12 for the small and the large probes, respectively. Unlike the previous results, no evidence of noise can be observed in the measured dielectric constants. The corresponding dielectric loss for the small and the large probes are as shown in Figure

A. 28 and Figure A. 29, respectively. By removing the Teflon part, the thickness of the test fluid in the modified setup is controlled by adding equal amounts of the ethanol/water mixture x_e=0.76 during each step.

Figure 4.11 shows that the dielectric constant measured using the small probe is less noisiness in the low frequency range and almost smooth in the high frequency range. Furthermore, the measured permittivity increases as the film thickness increases to a value of about the sensitivity depth (6 mm). For thicknesses larger than the sensitivity depth, the measured permittivity becomes independent of the film thickness. The main dielectric relaxation of ethanol/water mixture x_e=0.76 is located at about 1 GHz. Analysis of the imaginary part of the permittivity confirms that the relaxation frequency is close to 1 GHz (Figure A. 28).

Figure 4.12 shows that the dielectric constant measured using the large probe increases in the high frequency range and that it contains some oscillations. This phenomenon is outlined in electromagnetic resonance. When the thickness is approximately 5.25 mm (blue curve) the peak will occur at around 10 GHz, while for a thickness of 6.75 mm (red curve) the peak takes place at around 5 GHz. As the thickness increases, the resonance peak will shift toward the low frequency range, i.e. to the left in the data plot.

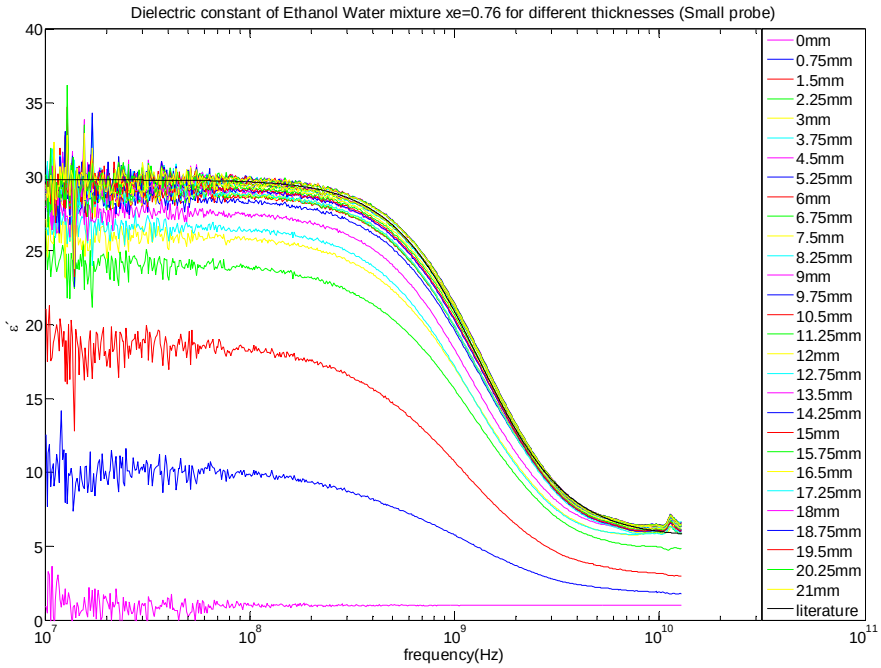

Figure 4.11: The dielectric constant of ethanol/water mixture x_e=0.76 versus frequency for different thicknesses of test fluid without the Teflon part (small probe) using the ideal calibration set. The thickness of fluid is increased from 0 to 21 mm in steps of 0.75 mm.

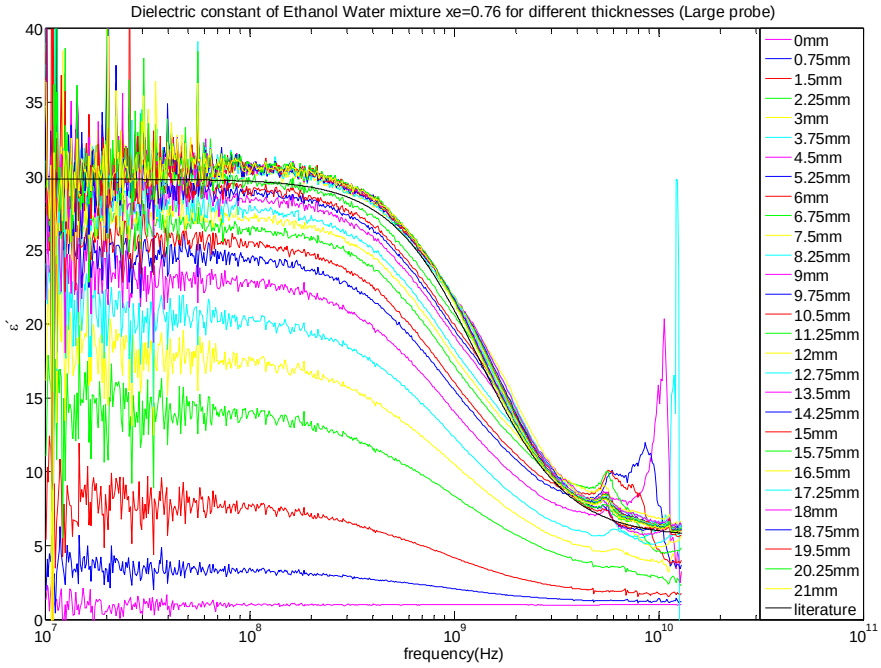

Figure 4.12: The dielectric constant of ethanol/water mixture x_e=0.76 versus frequency for different thicknesses of test fluid without the Teflon part (large probe) using the ideal calibration set. The thickness of fluid is increased from 0 to 21 mm in steps of 0.75 mm.

4.2 Single probe measurements

4.2.1 Apparent permittivity as a function of layer thickness

In this part, the static permittivity in the presence of Teflon is calculated by averaging dielectric constant as shown in Figure 4.8 and Figure 4.9, within the frequency range of 50 MHz – 200 MHz. Then, it is plotted as a function of thickness of liquid sample, where the final results for both probes are shown in Figure 4.13.

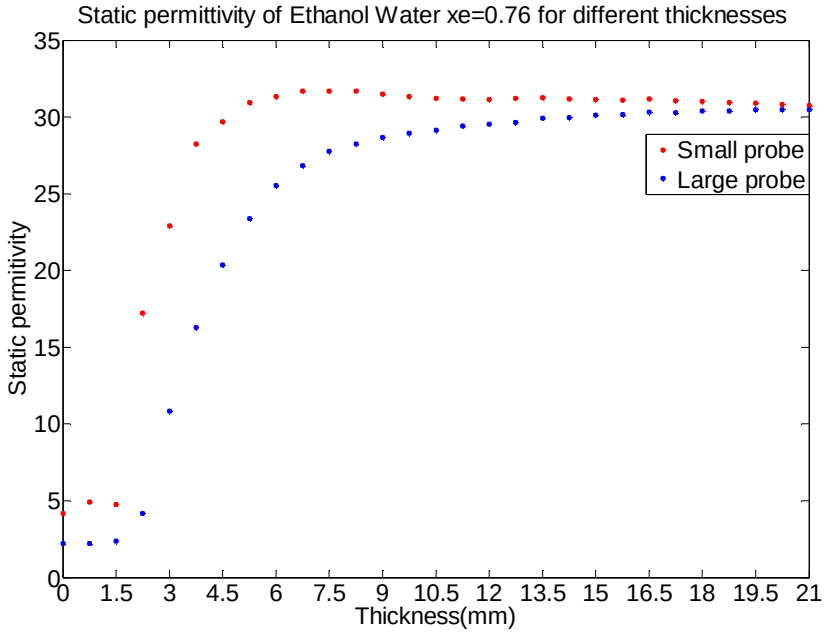

Figure 4.13: Static permittivity of ethanol/water mixture x_e=0.76 versus thickness of the SUT with using the Teflon part. The static permittivity is shown within the frequency range of 50 MHz - 200 MHz.

As can be seen from Figure 4.13, for zero fluid thickness (Teflon), the static permittivities measured by both probes are not identical. Since one of the calibration fluids is air, no extrapolation beyond the calibration permittivity is expected. This difference can be explained by the mechanical offset or mechanical inaccuracies of the Teflon part and height adjustment system. Although the Teflon part is at the lowest level, some fluid still remained in front of the small probes. Due to some mechanical inaccuracies in the measurement setup, the remaining liquid in front of the probe will cause measurement error for low thicknesses, i.e. less than 3 mm, even though the Teflon part is at its minimum level.

The estimation of the static permittivity was done without the Teflon part, and is based on the mean value of dielectric constant of ethanol/water mixture x_e=0.76 within the frequency range of 50 MHz – 200 MHz. The relationship between the static permittivity and the thickness, as shown in Figure 4.14, is given by a first order exponential relationship, where the measured permittivity for zero and infinite thickness of fluid are identical for both probes. Therefore, it can be concluded that more reliable and better results will be obtained when the Teflon part is removed.

Likewise, in section 4.3.2, the data as shown in Figure 4.11 and Figure 4.12 are used to calculate the static permittivity by averaging the dielectric constant within the frequency range of 50 MHz – 200 MHz. Subsequently the results are plotted versus thickness of fluid sample as shown in Figure 4.14. In contrast to Figure 4.13, at zero fluid thickness, i.e. when only air is present, the static permittivities measured by both probes are identical and equal to 1.

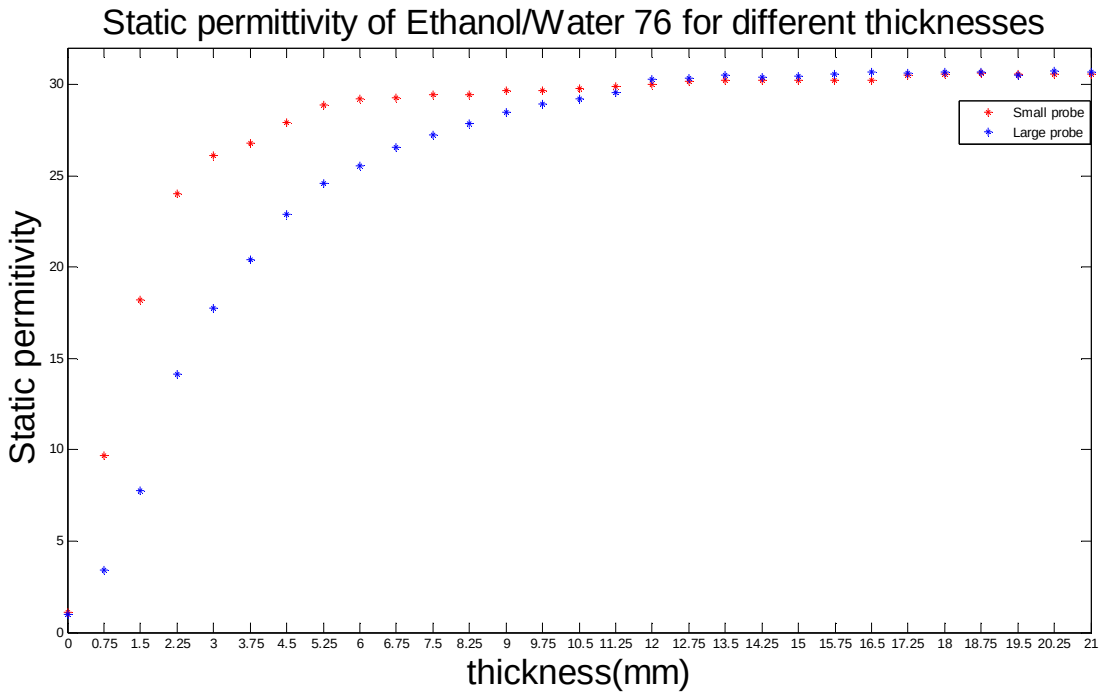

Figure 4.14: Static permittivity of ethanol/water mixture x_e=0.76 using the ideal calibration set for different thicknesses of test fluid without using the Teflon part.

4.2.2 Determination of probe constants

The probe constants D_1 and D_2 can be determined for the small and the large probe by curve fitting the apparent static permittivities to equation 66 using the best-fitted curves for both probes, as shown in Figure 4.15. The probe constants are reported as D_1=1.75 mm and D_2=3.62 mm for the small and the large probes, respectively.

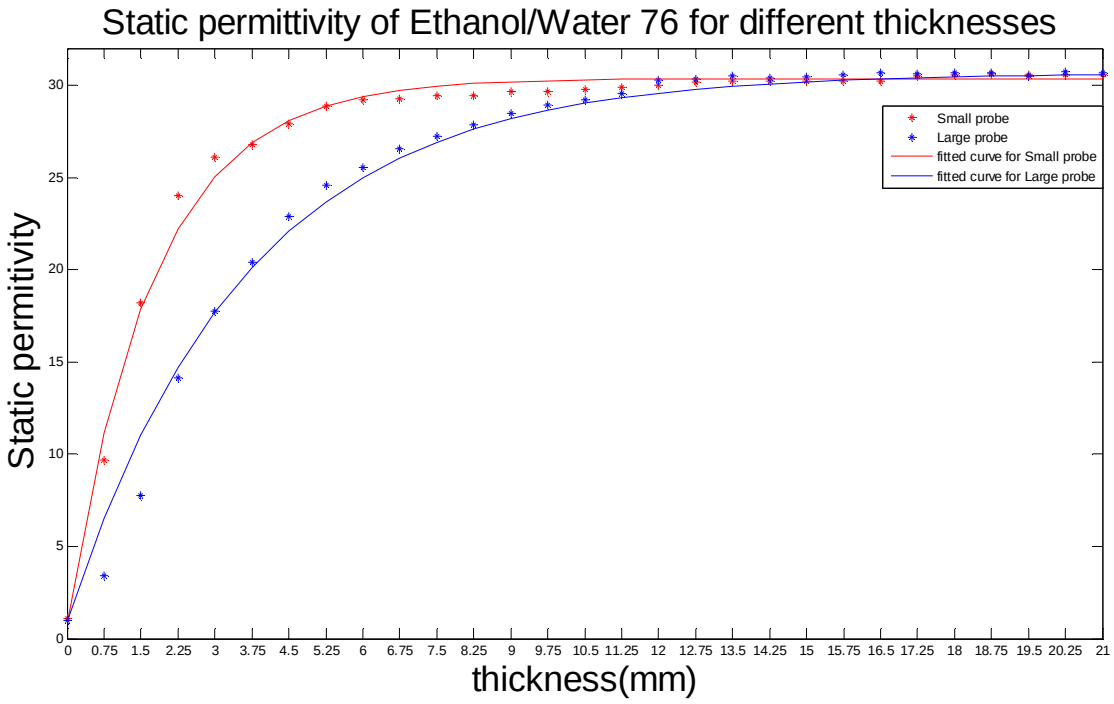

Figure 4.15: The static permittivity of ethanol/water mixture x_e=0.76 using the ideal calibration set for different thicknesses of test fluid without using the Teflon part and corresponding fitted curve for each probe.

4.2.3 Depth sensitivity estimation

It was also attempted to investigate the effect of different film thicknesses on the permittivity both at a single frequency and over a broad band frequency range. As an example of single frequency, Figure 4.16 shows the apparent permittivity for an ethanol/water mixture x_e=0.76 at 100 MHz. The apparent permittivity, measured by both probes increases exponentially with the layer thickness of the film and flattens out for higher film thicknesses. A similar behaviour can be observed for the measured static permittivity using the same fluid composition, as illustrated in Figure 4.16.

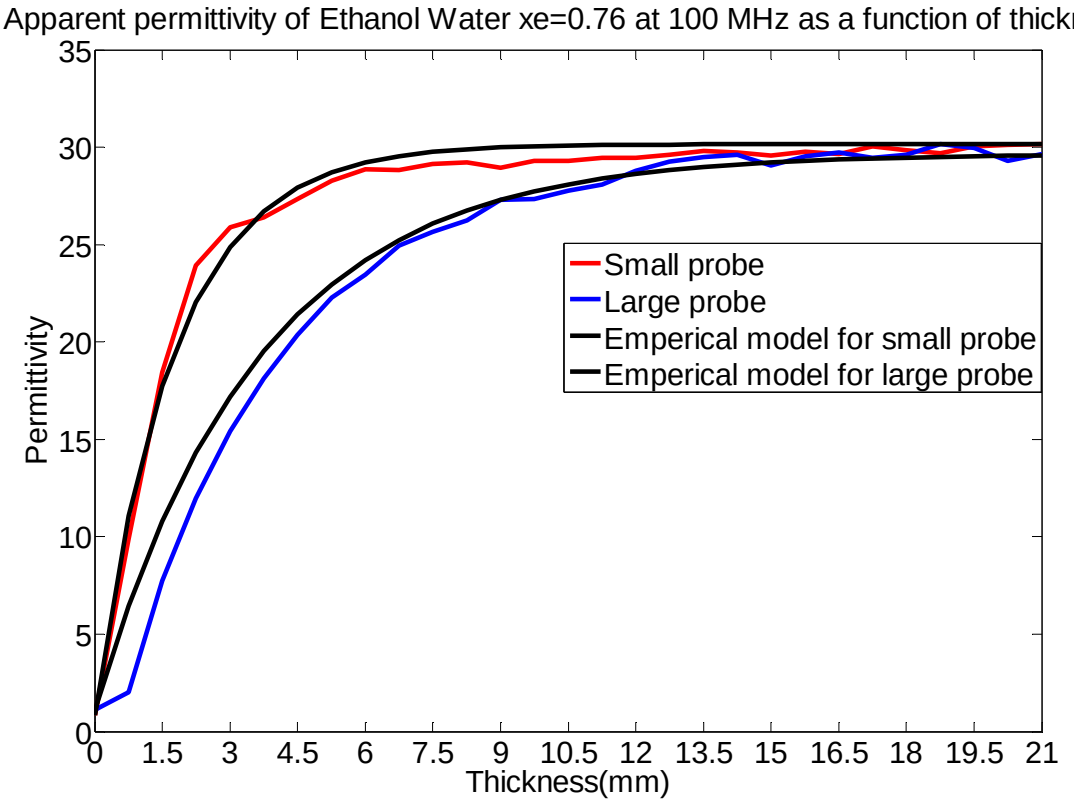

Figure 4.16: Measured apparent permittivity of ethanol/water mixture x_e=0.76 film with varying thickness by the large and small probes. The operating frequency is 100 MHz.

The depth sensitivity was also examined, and it was found that the measured permittivity is in good agreement with the infinite thickness criteria, as shown in Figure 4.17. As reported earlier, the sensitivity depths of both probes were 6 and 12 mm, or almost 1.3 times bigger than the outer radius of the probe.

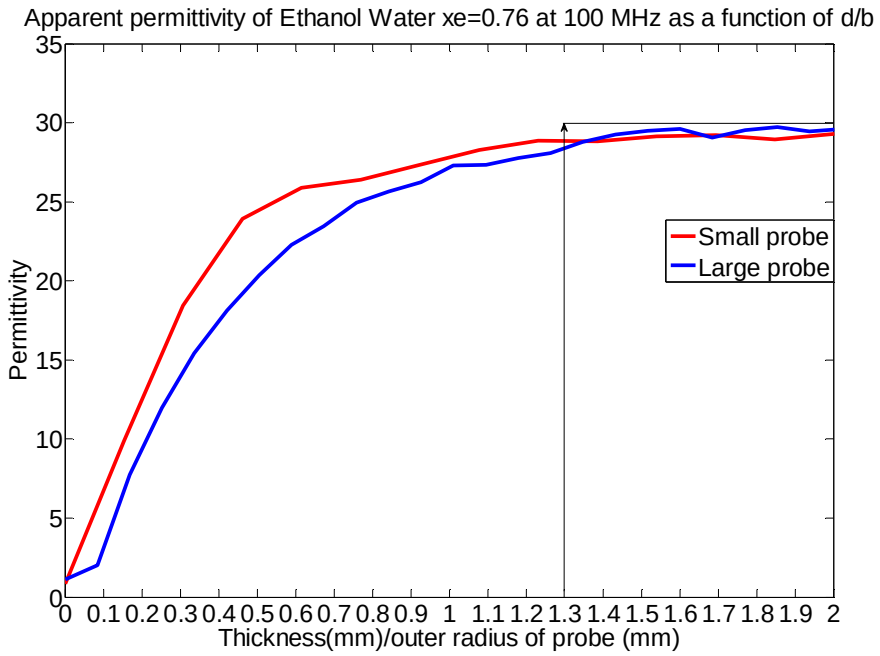

Figure 4.17: Measured apparent permittivity of the ethanol/water mixture x_e=0.76 film versus the ratio of thickness to the outer radius of the large and the small probes. The operating frequency is 100 MHz.

The sensitivity depth is defined as the thickness where the relative difference between the apparent permittivity and the fluid film permittivity is 2% or $(\varepsilon_A - \varepsilon_2) = 0.98(\varepsilon_1 - \varepsilon_2)$. Thereby, the critical film thickness corresponds to the thickness that gives an apparent permittivity which equals 98% of the fluid film permittivity. The sensitivity depth is defined as the spatial width of the sensitivity volume of the probe as viewed from the probe-fluid interface into the mixture [35]. As mentioned earlier in the theory section, the thickness of the sample has to be larger than about one to two times the outer radius of the probe in order to be treated as "infinite thickness". The sensitivity of a probe decreases exponentially with distance from the aperture. If the thickness (*d*) remains greater than the outer aperture radius (*b*), the permittivity converges to the data for infinite thickness. It means that by increasing the thickness of the layer the apparent permittivity does not increase any more when *(d/b* >1~2*)*. According to the results of the empirical model, the sensitivity depths are found to be about 6 mm for the small probe and 12 mm for the large probe. It can be concluded that the sensitivity depth is approximately 1.3 times bigger than the outer radius for each probe, which is in agreement with the defined criteria in section 3.5 (i.e. *d/b* >1~2).

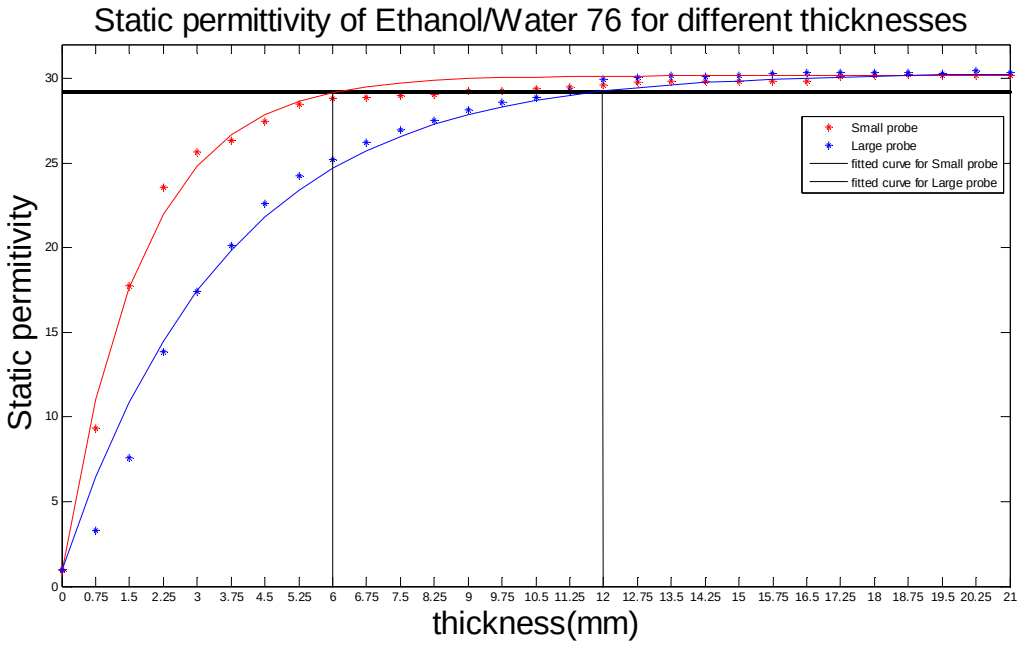

Figure 4.18: Apparent static permittivity versus thickness and sensitivity depth investigation for both probes.

4.2.4 Thickness and permittivity estimation using single probe system

For accuracy evaluation, it is assumed that the layer thickness d and permittivity of layer ε_1 are unknown, but the permittivity of the backing layer (air) or ε_2 is known. The ideal calibration set is used for this evaluation.

In the first case, the thickness of the film and the apparent permittivity are assumed to be known, and the permittivity of the ethanol/water mixture x_e=0.76 is calculated by the empirical model independent of the measurements done by the probes. The calculated ε_1 is shown in Figure 4.19, where in the first four measurements some deviation from the permittivity reported in literature is observed. However, the average of the accuracy values for the remaining measurements by the small and the large probe are reported to be approximately 99.6% and 97.25%, respectively. In this study, the accuracy is defined as:

$$Accuracy = \frac{Actual\ value\ -\ \left|Measured\ Value - Actual\ value\right|}{Actual\ value} \times 100 \qquad (76)$$

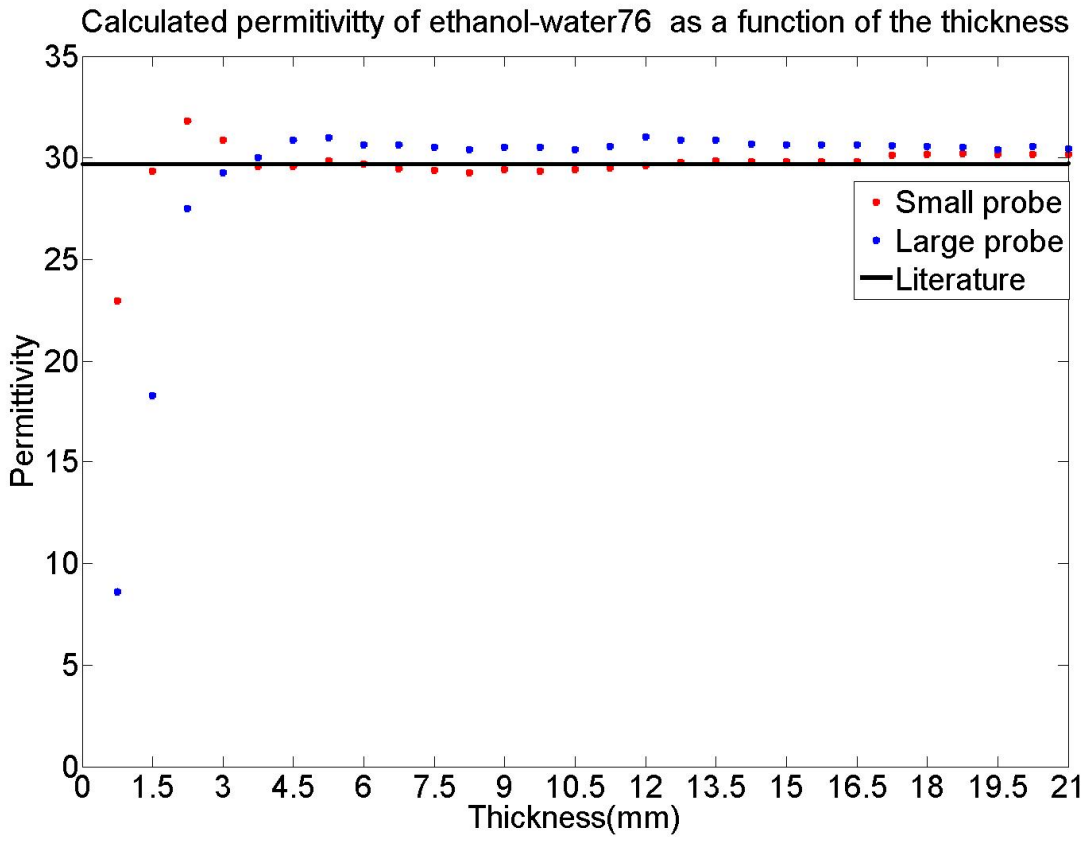

Figure 4.19: Measured permittivity of the ethanol/water mixture x_e=0.76 when the thickness and the apparent permittivity are known.

In the second case, the permittivity of layer ε_1 and the apparent permittivity are assumed to be known, and the film thickness of the ethanol/water mixture x_e=0.76 is calculated using the empirical model independently for each of the measurements done by both probes. As can be seen in Figure 4.20, the measured thickness of the ethanol/water mixture x_e=0.76 by the small probe and the large probe indicate some deviation from the actual thickness value. Since the probes are more sensitive for low thicknesses, the deviation from actual value is less pronounced in low thicknesses while for high thicknesses more deviation is observed for both probes, approving that for thicknesses larger than the small probe's sensitivity depth, a significantly higher error is to be expected. The sensitivity depth for the small probe and the large probe are reported to be 6 mm and 12 mm, respectively, which will be discussed in the next section.

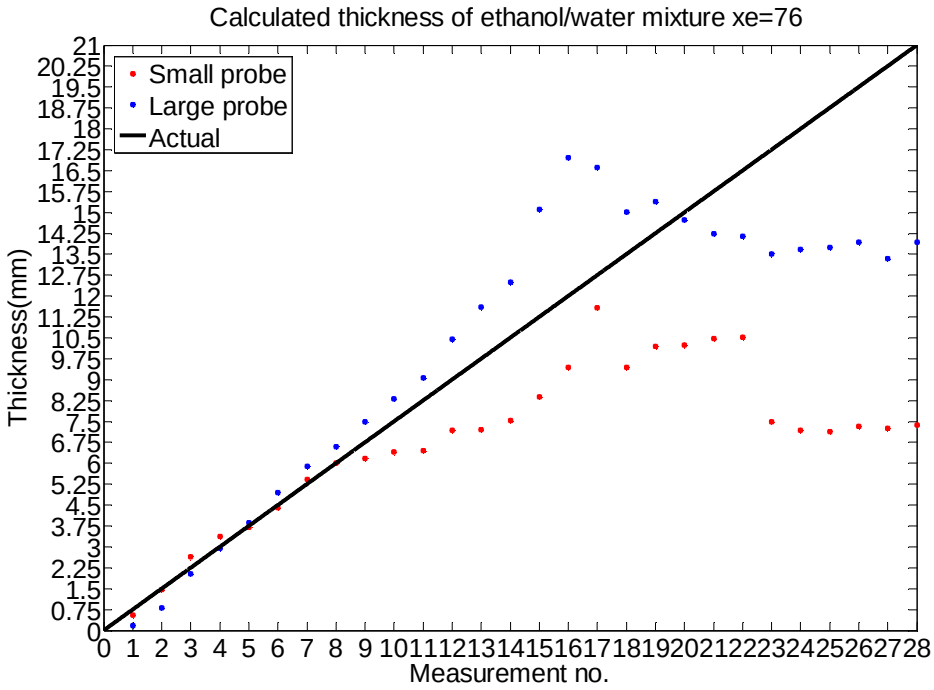

Figure 4.20: Measured thickness of fluid film when the apparent permittivity and the permittivity of the ethanol/water mixture x_e=0.76 are known.

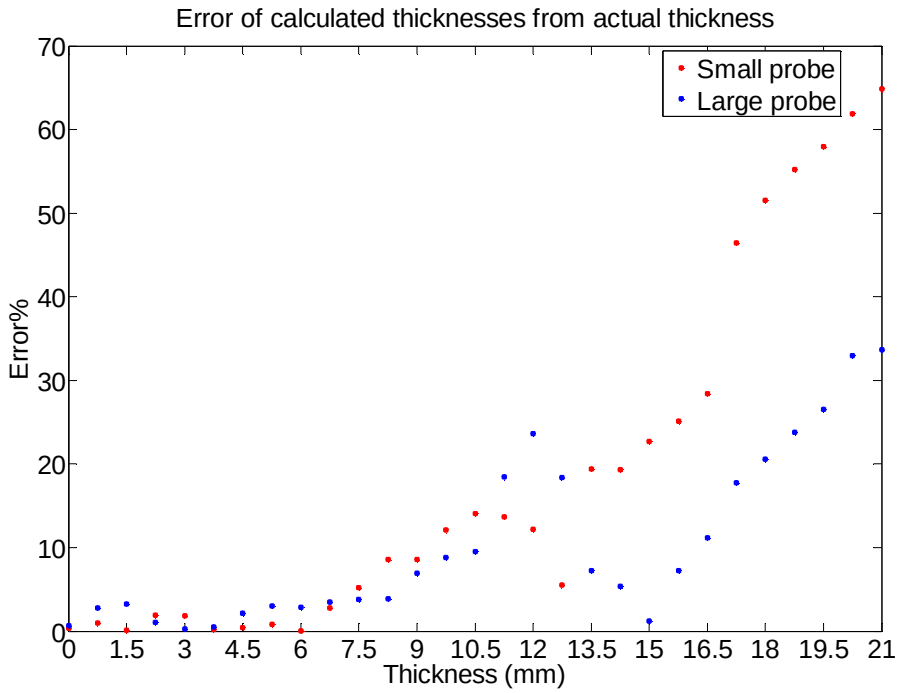

Figure 4.21: Error for measured thickness by the large and the small probes.

As shown in Figure 4.21, the error of the calculated thickness for thicknesses less than 6 mm, i.e. the sensitivity depth of the small probe, is less than 4%, while the maximum error for the calculated thickness is less than 12 mm, i.e. the sensitivity depth of the large probe is around 20%.

4.3 Dual probes system

In this section, the measured permittivities by the small and the large probes for different thicknesses of the SUT using the best calibration set are presented. Thereafter the static apparent permittivity as a function of film thickness for each probe is shown. Using the empirical exponential model of the probes, the thickness and permittivity of the SUT are estimated.

How the permittivity varies as the thickness increases at a selected single frequency and over a frequency range are investigated. Thickness control is performed by adding a distinct amount of fluid without using the Teflon part and the height adjustment system.

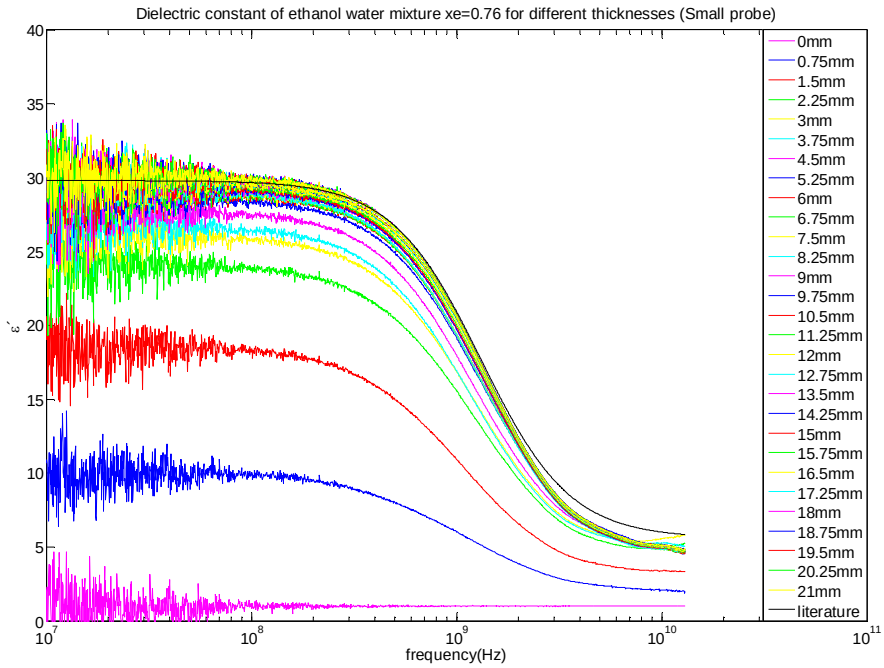

Figure 4.22: Estimated apparent permittivity of the ethanol/water mixture x_e=0.76 for the small probe when the three calibration fluids are: air, ethanol and ethanol/water mixture x_e=0.54. The fluid thickness is increased from 0 to 21 mm in steps of 0.75 mm without the height adjustment system.

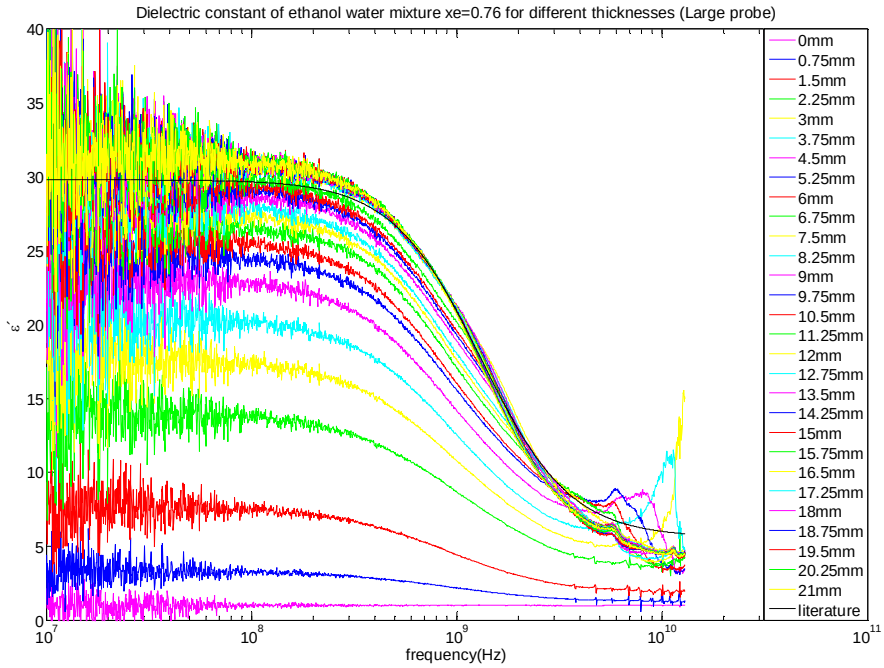

Figure 4.23: Estimated apparent permittivity of the ethanol/water mixture x_e=0.76 for the large probe when the three calibration fluids are: air, ethanol and ethanol/water mixture x_e=0.54. The fluid thickness is increased from 0 to 21 mm in steps of 0.75 mm without the height adjustment system.

Figure 4.22 and Figure 4.23 show the measured dielectric constant for the ethanol/water mixture x_e=0.76 by the small and the large probes, respectively. As shown, the film thickness of the mixture varies from 0 to 21 mm in increasing steps of 0.75 mm. The best combination set of calibration fluids for thickness measurement (ethanol, air, ethanol/water mixture x_e=0.54) was used for the BCP prior to each experiment, as described earlier. All measurements were performed in a range of low to high frequency from 10 MHz to 13 GHz. Figure A.30 and Figure A.31 illustrate the measured dielectric loss for the ethanol/water mixture x_e=0.76 using the small and the large probes, respectively.

As can be seen from these figures, as expected the apparent permittivity and dielectric loss depend on the thickness of the sample, where all the curves follow a similar trends to that reported in the literature (black curve) for dielectric permittivity and loss of ethanol/water mixture x_e=0.76. It is also interesting that the measured permittivity values converge towards the literature reported values, especially for the film with thickness higher than the sensitivity depth. Figure 4.23 also shows how radiation affects the large probe measurements in the high frequency range.

According to Table 3.7, it is known that the minimum radiation frequency for the large probe for this set of calibration fluids and the SUT, is approximately 0.8 GHz. Due to the quarter-wavelength resonance effect, destructive resonance occurs in the high permittivity fluid films, and the total reflected signal is influenced by a reflection at the second interface. Therefore, the secondary reflected wave at the certain resonance frequencies becomes destructive. At higher thicknesses the radiating wave can be attenuated through the SUT, but in lower thicknesses and at certain frequencies, resonance peaks can be observed. The resonance frequency is dependent on both the thickness and the permittivity of the film.

As described in Chapter 2, the permittivity decreases from its maximum (i.e. static) value to the corresponding value (ε_∞) as the frequency increases. This reduction region is called the dispersion region. According to Figure 4.22 and Figure 4.23, the dispersion frequency is located at frequencies higher than 200 MHz for both probes. At frequencies lower than approximately 50 MHz there is significant noise in the measured permittivity. Therefore, the static permittivity is calculated by averaging the permittivity within the frequency range of 50 MHz – 200 MHz.

Since one of the calibration fluids is air, the measured static permittivity for zero thickness of film, i.e. air, is measured identically by both probes, as illustrated in Figure 4.24 and Figure 4.16. The static permittivity measured by both probes within the frequency range of 50 MHz – 200 MHz is calculated and plotted for different thicknesses of the SUT as shown in Figure 4.24.

As determined previously, the probe constant for the small and the large probes are D_1=1.75 mm and D_2=3.62 mm, respectively. Using the probe constants, the static permittivity from the empirical model is plotted as a function of layer thickness for ethanol/water mixture x_e=0.76 in Figure 4.24 (solid lines). It is seen that there is a good correlation to the measured static permittivities (dotted data).

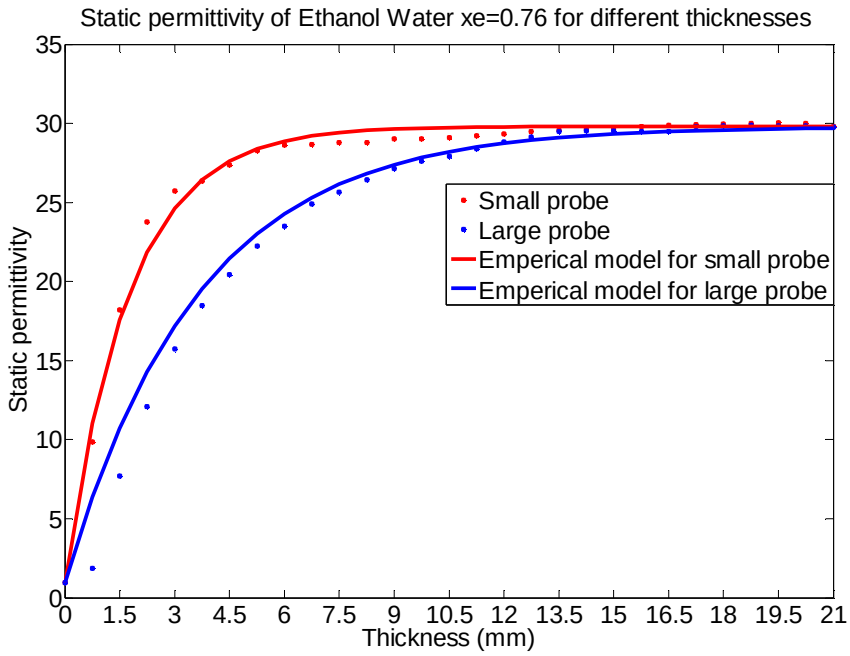

Figure 4.24: Static permittivity of ethanol/water x_e=0.76 versus thickness of the SUT, without the Teflon part and corresponding fitted curve for each probe. The calibration fluids are air, ethanol and ethanol/water mixture x_e=0.76.

4.3.1 Simultaneous estimation of permittivity and layer thickness using the dual probes system

In the dual probes system, the sample permittivity (ε_1) and film thickness (d) can be determined if the probe constants (D_1 and D_2) and the measured apparent permittivity (ε_{A1} and ε_{A2}) are known for the small and the large probes, respectively. Applying equation 66 for each probe generates two equations 77 and 78 with two unknowns (ε_1 & d), that can be solved simultaneously.

$$\varepsilon_{A1} = (\varepsilon_2 - \varepsilon_1)\exp(-d/D_1) + \varepsilon_1 \tag{77}$$

$$\varepsilon_{A2} = (\varepsilon_2 - \varepsilon_1)\exp(-d/D_2) + \varepsilon_1 \tag{78}$$

where D_1=1.75 mm and D_2=3.62 mm. A total of 29 series of apparent permittivity measurements were carried out in this study by the dual probes system providing data to solve the two equations with the two unknowns for each series. The calculated permittivities and film thicknesses for all the 29 measurements are illustrated in Figure 4.25 and Figure 4.26, respectively.

As can be seen in Figure 4.25, a relatively good agreement is established between the calculated permittivity of ethanol/water mixture x_e=0.76 from the dual probes system (red line) and the corresponding the literature value (black solid line) for all investigated thicknesses.

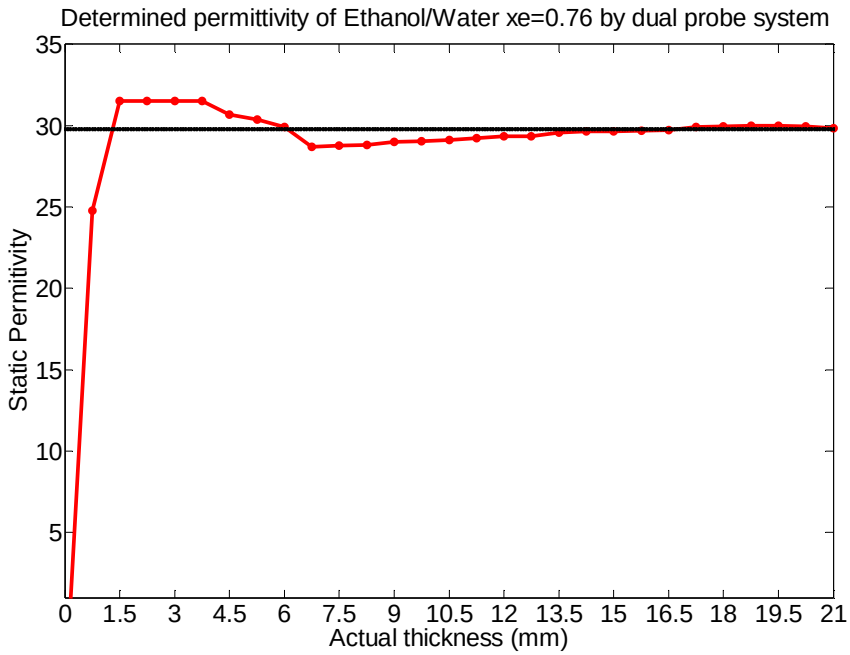

Figure 4.25: Determined permittivity of ethanol/water mixture x_e=0.76 for different thicknesses by the dual probes system, shown by red points. The black line is the corresponding literature values of permittivity of ethanol/water mixture x_e=0.76. The best calibration set is used.

As shown in Figure 4.26, the film thickness may be determined by using the dual probes system if the thickness of the film is smaller than the sensitivity depth of the small probe (black solid line at around 6 mm), whereas for film thicker than the sensitivity depth of the small probe, the estimated (d) deviates from the actual thickness (black curve). The sensitivity depths reported in section 4.10 are about 6 mm for the small probe and 12 mm for the large probe. It is found that the permittivity of the layer can be calculated within a minimum 94.3% accuracy (mean accuracy is 97.4%) for layers thicker than about 1.5 mm

If the thickness of the film is between the sensitivity depth of the small and the large probe (i.e. 6 mm <d< 12 mm), the thickness can be calculated by an alternative method. For thickness larger than 6 mm, the apparent permittivity measured by the small probe (ε_{A1}) is assumed to be equal to the permittivity of the infinitely thick layer of ethanol/water

mixture x_e=0.76 (or ε_1). By assuming $\varepsilon_1=\varepsilon_{A1}$, and solving the empirical relation for the large probe, the thickness is determined from the sensitivity depth of the small probe up to the sensitivity depth of the large probe (i.e. 6 mm<d<12 mm).

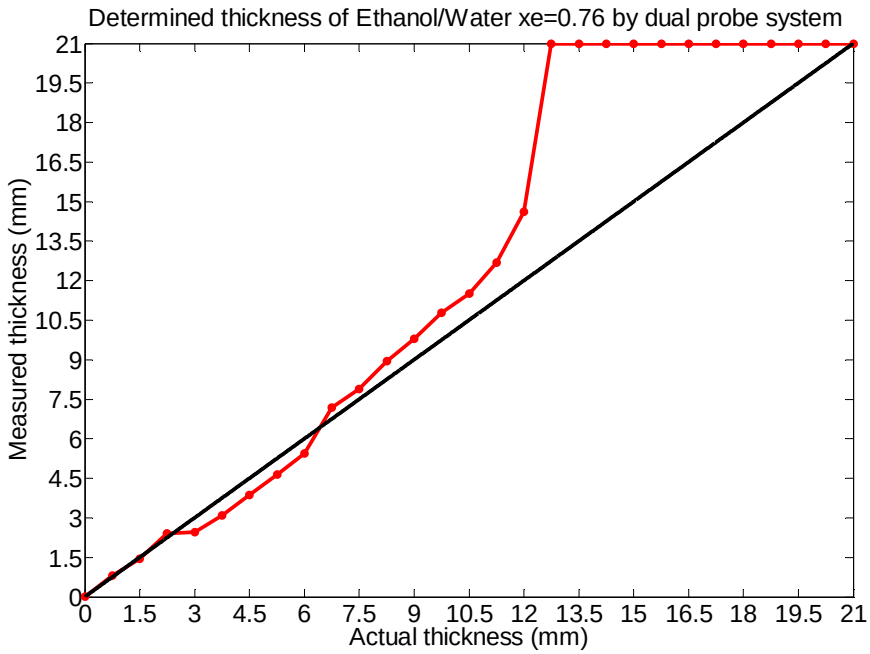

Figure 4.26: Determined thickness of ethanol/water mixture x_e=0.76 by dual probes system shown by red points and the black line represent true values of thickness. The best calibration set is used.

The results shown in Figure 4.27 confirm that the thickness prediction can be performed with good precision within minimum 78.23% accuracy (mean accuracy is 89.85%) using the dual probes system for thicknesses less than the sensitivity depth of the large probe where the maximum error in the thickness prediction for layers thinner than 6 mm (sensitivity depth of the small probe) is 0.75 mm and the corresponding error for layers thinner than 12 mm (sensitivity depth of the large probe) is approximately 2 mm.

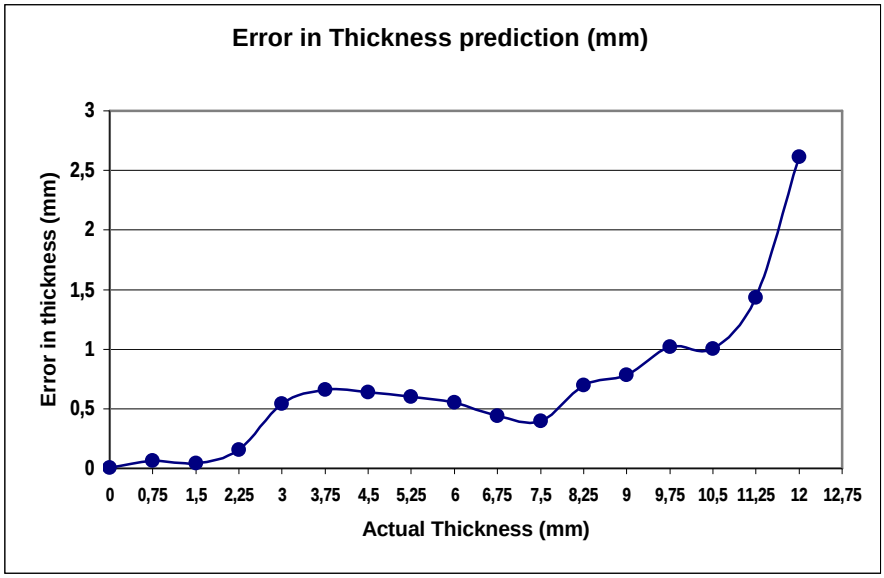

Figure 4.27: Error in thickness measurements done with the dual probes system for thicknesses less than the sensitivity depth of the large probe.

4.3.2 Measurement uncertainty analysis in the film thickness and permittivity measurements

As mentioned in section 4.2, in the frequency range higher than 50 MHz, the reproducibility of the permittivity measurement by each probe system is less than one. Therefore, the overall measurement uncertainty will be higher. In this part of the thesis, the existing error(s) in thickness and permittivity measurement are investigated and quantified. It is assumed that the standard deviation of all the measurements are equal to one as the worst case in uncertainty analysis, which means that the apparent permittivity measured by both probes possesses a ±1 unit deviation from its actual permittivity value.

In order to make our approach in measurement uncertainty analysis more understandable, a further clarification is made here. For a particular set of the measured apparent permittivities (ε_{A1} for the small probe and ε_{A2} for the large probe), the sample permittivity (ε_1) and film thickness (d) are calculated. Following, if a unity value representing the standard deviation of one is added to or deducted from the existing (ε_{A1} and ε_{A2} as the base), four series of new apparent permittivities ($\varepsilon_{A1\text{-}new}$ and $\varepsilon_{A2\text{-}new}$) are obtained. By solving the corresponding two equations with two unknowns for each of these so-called new apparent permittivities, will result in four newly calculated ε_1 and d. Hence, the error

between these four new- ε_1 and original base-case ε_1 can be found and the maximum error is determined.

Figure 4.28 and Figure 4.29, show the maximum error in the calculated permittivity of test fluid and film thickness, respectively, assuming that the measurement uncertainty equals one. As Figure 4.28 shows, the maximum error for the estimated permittivity of ethanol/water mixture x_e=0.76 with the dual probes system is almost identical for that of the actual thickness of 4.5 mm, but higher for both the measured and the ideal data in between one and two for thicknesses higher than the sensitivity depth of the small probe, i.e. 6 mm.

It should be mentioned that the so-called ideal data represent the corresponding ε_1 and d data calculated from the empirical models developed by curve-fitting the measured data in Figure 4.25 (solid lines). The corresponding trend of maximum error reflects the deviation of the estimated unknowns, i.e. ε_1 and d, from their actual values exactly.

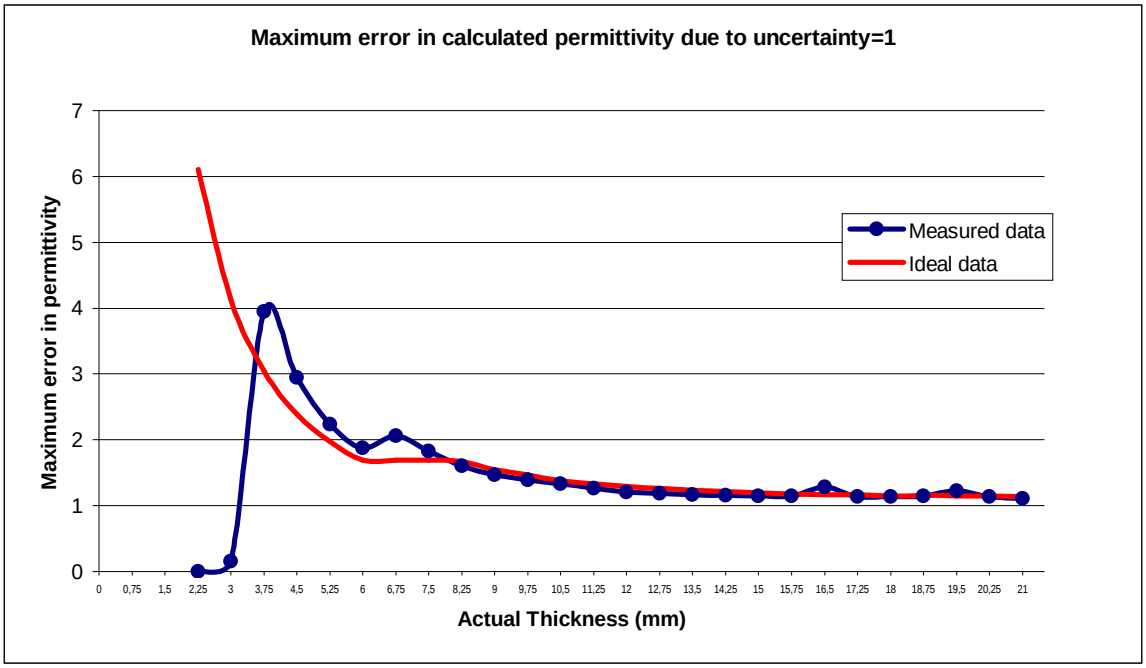

Figure 4.28: Maximum error of the calculated permittivity due to an uncertainty equal to one by the dual probes system.

As shown in Figure 4.29, following a similar trend, the maximum error of the estimated film thickness for both the measured and ideal data increases gradually to a maximum value of around 11 mm at actual thickness of 9 – 9.75 mm, from where the maximum error decreases. The slight difference between the two curves can be explained based on the fact that the empirical models used for the ideal data do not fit completely with the measured data, as illustrated in Figure 4.25.

In order to find an explanation for why the increasing trend in maximum error is observed, a thorough investigation was made on four cases of uncertainty analysis for ideal data. As can be seen in Figure 4.30a and Figure 4.30b, the generated error is relatively low, around 0.15 mm for thicknesses larger than 3 mm, where a unity value is added to or deducted from the measured apparent permittivities by both probes. In Figure 4.30c and Figure 4.30d however an increasing trend is observed just for the uncertainty cases where one unity value is added to one of the measured apparent permittivities and is deducted from another one or vice versa. For the third case in the uncertainty analysis, as shown in Figure 4.30c , the error increases from 1.5 mm for the sensitivity depth of the small probe to around 4.5 mm at a thickness of 12 mm, corresponding to the sensitivity depth of the large probe. A maximum error is also reflected in Figure 4.29 and is observed only in the last case of the uncertainty analysis, where one unity value is deducted from the measured apparent permittivity of the small probe and one unity value is added to the measured apparent permittivity of the large probe. As can be seen, the error is relatively low and around 2 mm up to the sensitivity depth of the small probe (i.e. 6 mm), and reaches its maximum a at thickness of 9.75 mm. It is anticipated that the corresponding thicknesses from the new apparent permittivities ($\varepsilon_{A1\text{-}new} = \varepsilon_{A1}$-1 and $\varepsilon_{A2\text{-}new} = \varepsilon_{A2}$+1) is under- or over-estimated by adding a unity value, hence generating more errors as layer thickness increases.

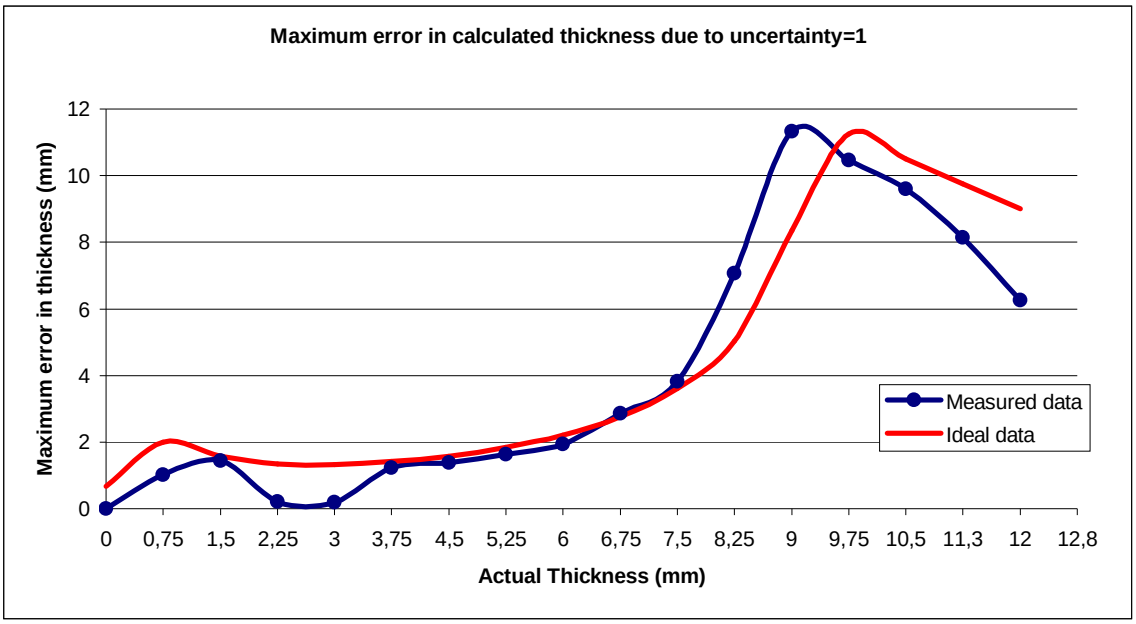

Figure 4.29: Maximum error of calculated thickness due to uncertainty equal to one by the dual probes system.

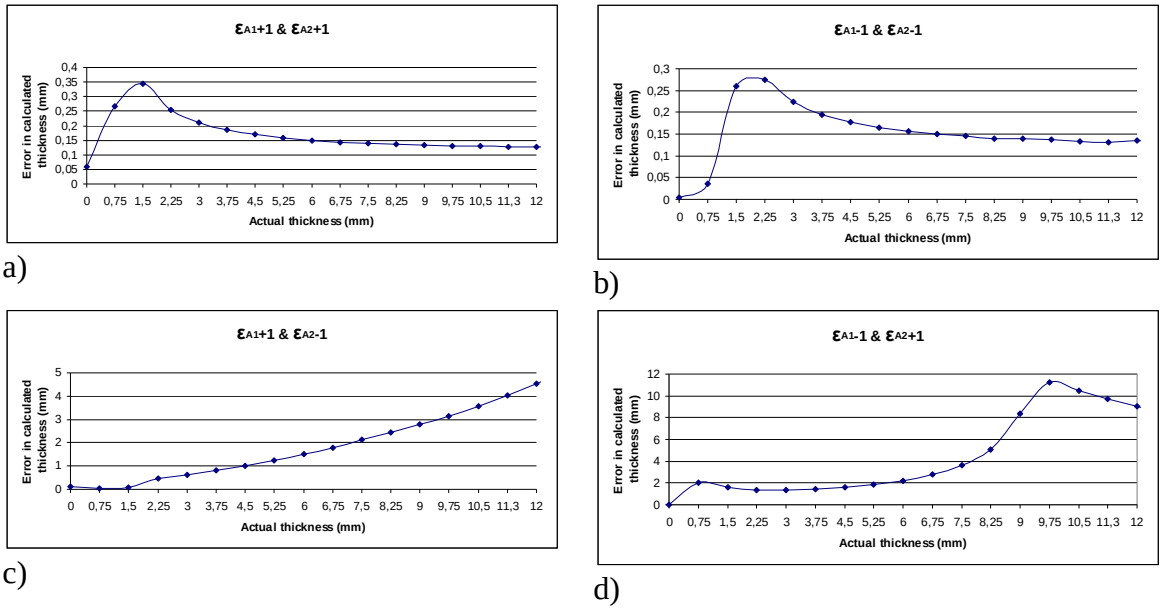

a) b) c) d)

Figure 4.30: Generated errors in calculated thicknesses due to one unity uncertainty for ideal data, where a) $\varepsilon_{A1\text{-}new}=\varepsilon_{A1}+1$ and $\varepsilon_{A2\text{-}new}=\varepsilon_{A2}+1$; b) $\varepsilon_{A1\text{-}new}=\varepsilon_{A1}-1$ and $\varepsilon_{A2\text{-}new}=\varepsilon_{A2}-1$; c) $\varepsilon_{A1\text{-}new}=\varepsilon_{A1}+1$ and $\varepsilon_{A2\text{-}new}=\varepsilon_{A2}-1$; d) $\varepsilon_{A1\text{-}new}=\varepsilon_{A1}-1$ and $\varepsilon_{A2\text{-}new}=\varepsilon_{A2}+1$

According to the discussions above, it can be summarized that for the layer thicknesses between the sensitivity depth of the small probe (6 mm) and large probe (12 mm), the estimated permittivity deviation is between one to two units. Therefore, the permittivity

estimation seems to be more accurate for thicker layers. But in contrast to the permittivity measurement, the thickness estimation seems to be more accurate for layers with a thickness less than the sensitivity depth of the small probe. Hence, it can be concluded that the dual probes system gives a more accurate and better estimate of thin layer thickness and thicker layer permittivity.

4.4 Conductivity measurements of diesel /water emulsions

Figure 4.31 and Figure 4.32, show the measured dielectric loss by the small and the large probes, for 7 mixtures of diesel and brine solutions comprising different salinities, respectively. The dielectric loss of distilled water/diesel oil is not shown since it was used as one of the calibration fluids. The measured dielectric constants for both probes are shown in Appendix C.

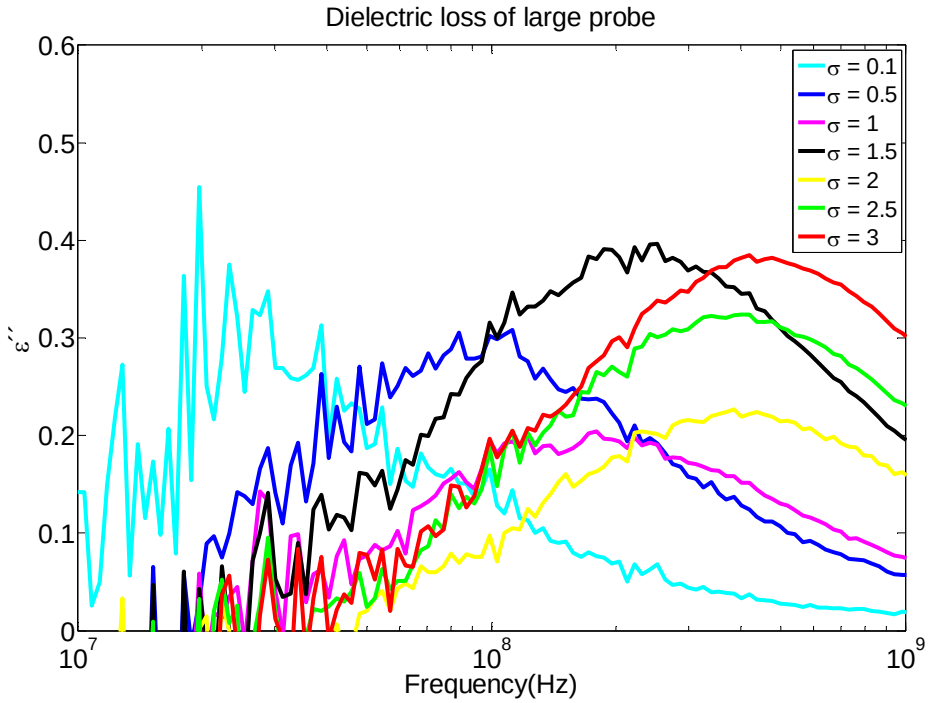

Figure 4.31: Dielectric loss by the large probe for water in diesel emulsion Φ=20% with different conductivities. Calibration fluids are ethanol/water mixture x_e=0.76, diesel and water/ diesel emulsion (Φ=20% and σ=0).

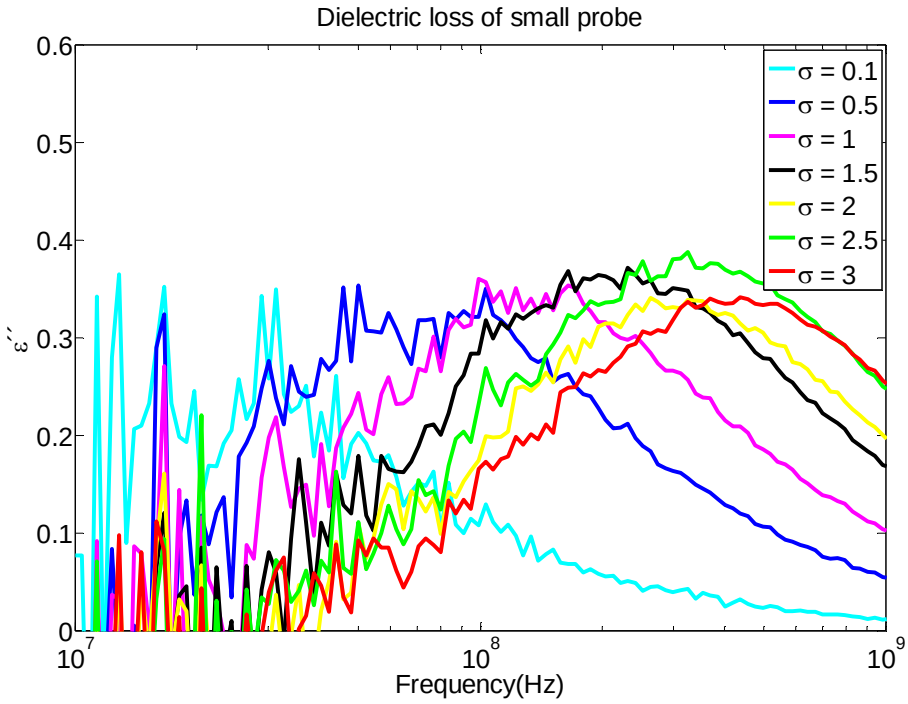

Figure 4.32: Dielectric loss by the small probe for water in diesel emulsion Φ=20% with different conductivities. Calibration fluids are ethanol/water mixture x_e=0.76, diesel and water/ diesel emulsion (Φ=20% and σ=0).

Since the dielectric loss spectrum contain some noise, reading the exact value of the maximum dispersion frequency for each spectrum is possible by introducing the upper bound / lower bound method which is a simple way to get a rough estimate of the uncertainty in a measured quantity. Uncertainty bars for the dispersion frequency are illustrated in Figure 4.33 and Figure 4.34. As can be seen, the relaxation frequencies measured by the small and the large probes increase as the conductivity are increased. The black solid lines (calculated from Hanai-Boyle mixture equation and Peyman et al equations [43]) represent the linear relationship between conductivity and dispersion frequency. A clear deviation between the measured and the literature data can be anticipated due to the cluster formation of water droplets rather than the assumed single spherical droplets in Hanai-Boyle mixture. Interactions between the dipolar droplets are assumed to have an impact on relaxation frequency. Thus the Maxwell-Wagner relaxation in such that a mixture so far has not been possible to reproduce [44]. If the dispersed phase droplets shapes are not spherical, the Hanai-Boyle equation is not applicable for finding the relaxation frequency.

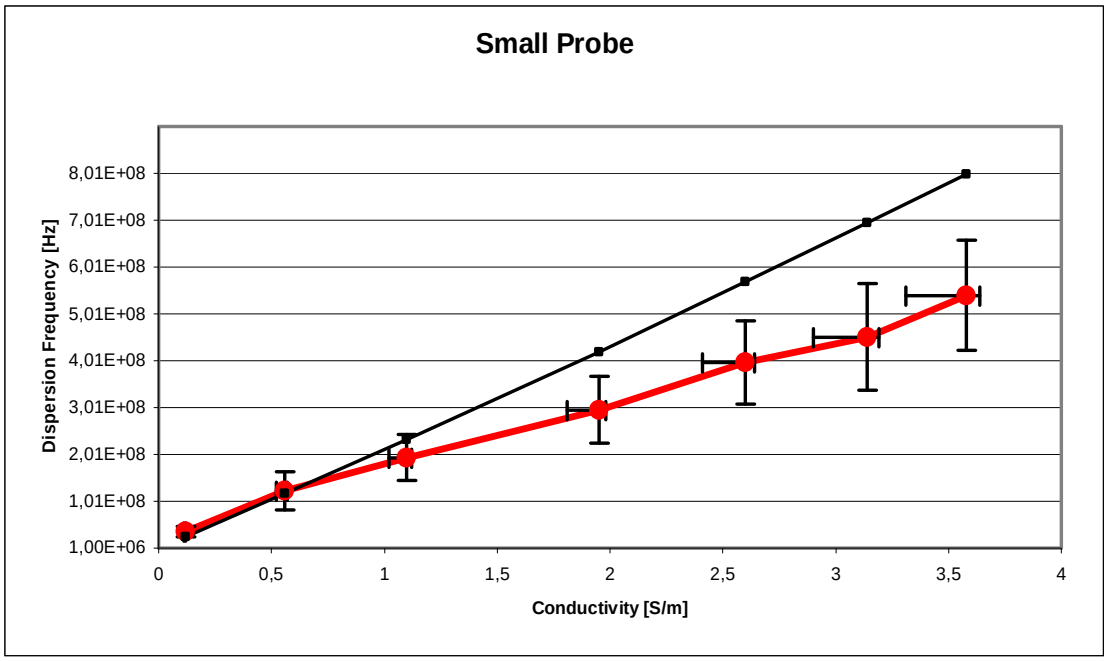

Figure 4.33: Dispersion frequency by the small probe versus conductivity. The horizontal bars indicate the uncertainty of the conductivity due to temperature variations between 30-36 ˚C. The vertical bars indicate the uncertainty in reading the dispersion frequency. Black solid line shows the literature data according Hanai-Boyle mixture equation and Peyman et al equations [43].

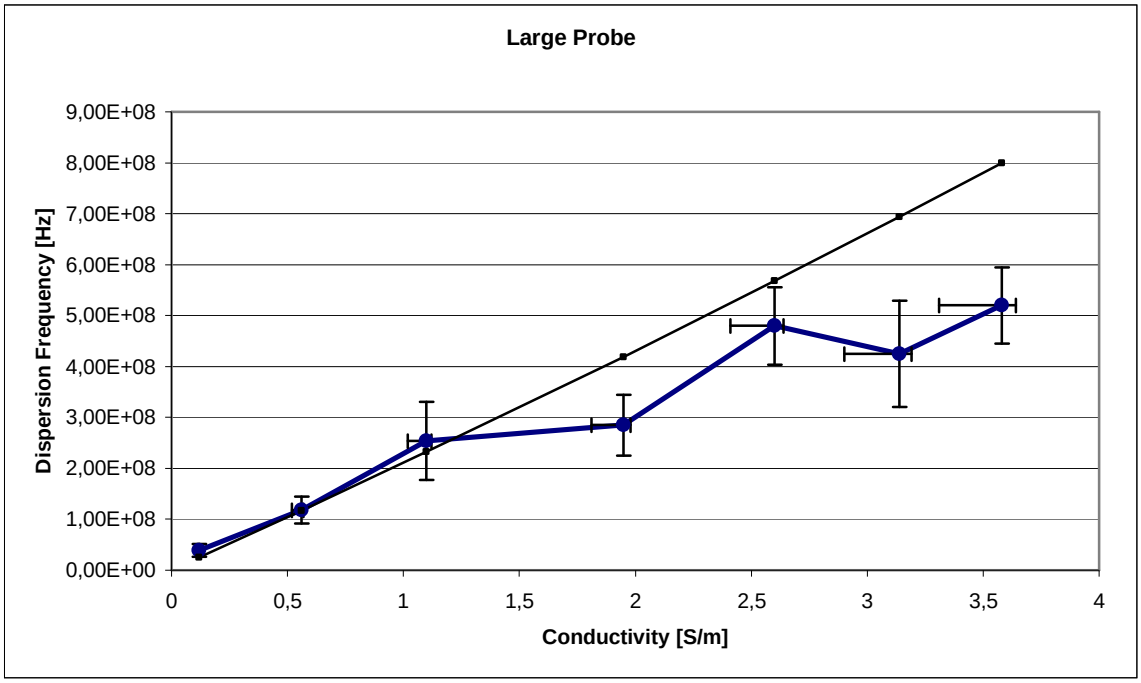

Figure 4.34: Dispersion frequency by the large probe versus conductivity. The horizontal bars indicate the uncertainty of the conductivity due to temperature variations between 30-36 ˚C. The vertical bars indicate the uncertainty in reading the dispersion frequency. Black solid line shows the literature data according Hanai-Boyle mixture equation and Peyman et al equations [43].

5 Conclusions

Gas hydrates tend to accumulate on the inner wall of a pipeline. Formation of gas hydrates in the pipeline cause local changes in the dielectric parameters. Coaxial probes are more sensitive to the dielectric materials in the vicinity of the sensor and are also non-intrusive, thus avoiding a pressure drop along the pipeline. These features make the coaxial probes suitable to be mounted on the pipe wall to detect hydrate formation on the inner pipe wall.

The aim of this work was to conduct a feasibility study on a measuring device to monitor hydrate formation. The developed measurement system is based on two open ended coaxial probes with different geometries. This makes it possible to determine both thickness and permittivity of the fluid. A high degree of accuracy has been obtained through suitable design of the measurement system, optimized calibration and experimental routines.

The main conclusion of this work is that a two-probe system with different geometries and sensitivity depths can be employed to determine both the fluid permittivity and the thickness. Dual probes mounted on the pipe wall can be a suitable technique for gas hydrate monitoring by measuring the changes of permittivity and corresponding hydrate layer thickness.

Cole's Bilinear Calibration Procedure was used together with the simple capacitance model to obtain the apparent static permittivity of the SUT as the layer thickness is increased. Empirical models for two probes were used to model the relationship between the static apparent permittivity and the thickness of the SUT.

Through a series of calibration attempts, an attempt was made to find a desired set of calibration fluids to perform thickness measurements. The highest accuracy was obtained by optimizing calibration fluids with well-known permittivities in the same range as the SUT. The best calibration fluids were air, ethanol and ethanol/water mixture x_e=0.54 when the SUT was ethanol/water mixture x_e=0.76. Reproducibility of the small and the large probes within the frequency range of 50 MHz – 13 GHz were 0.4 and 0.9, respectively.

Using static permittivity within the frequency range of 50 MHz – 200 MHz, empirical models for the both probes were obtained. Probe constants for the large and the small probes were estimated to be 0.4 and 0.36 times the inner radius of the outer conductor of the probes, respectively and corresponding sensitivity depths were reported to be 1.3 times the inner radius of the outer conductor of the probes.

Two probes with different sensitivity depths provided the possibility to determine both the permittivity and film thickness by applying the BCP and the empirical exponential model of the probes. Although the thickness detection was achievable for the layer thinner than the sensitivity depth of the large probe, but it was most accurate for the layer with thickness less than the sensitivity depth of the small probe. The permittivity predictions were more accurate for the thicker layers. Therefore, the thicker the layer, the more accurate the permittivity prediction will be using the dual probes system.

It was found that the thickness of the layers can be predicted within a minimum of 78.23% accuracy (mean accuracy is 89.85%) for layers thinner than the sensitivity depth of the large probe. It was also found that the permittivity of the layers can be calculated to within a minimum of 94.3% accuracy (mean accuracy is 97.4%) for layers thicker than about 1.5 mm.

The measurements of water in oil emulsions with different salinities of dispersed phase show that the open ended probes can be used to perform conductivity measurements. It was observed that the relaxation frequency obtained from broadband complex permittivity spectrum increases due to the increased numbers of ions present.

6 Further Work

Suggestions for further work:

- Using a more precise setup with Teflon as a backing layer and a height adjustment system.
- Applying more than two (even series) of probes with different sensitivity depths to obtain more accurate results when the thickness is greater than the sensitivity depth of the small probe. It may be convenient to use more than two probes mounted in the setup.
- Finding a more flexible algorithm to solve the empirical equations for two and more probes.
- Under the condition of using the dual probes system for the non-flat surface, for example pipe.
- Under condition of varying temperature, pressure and vibration to monitor the behaviour of the coaxial probes.
- Use the dual probes system for monitoring of hydrate formed inside the experimental chamber and estimate the thickness
- Conductivity investigation by ideal Hanai-Boyle emulsions.
- Conductivity measurement of diesel /water emulsions for water fraction more than 20% and with more salinity over a wide frequency range (higher than 9 GHz) by simultaneously monitoring the conductivity and the temperature.

This page is left intentionally blank.

References

[1] E. D. Sloan, and C. A. Koh, *Clathrate hydrates of natural gases*, Boca Raton, Fla.: CRC Press, 2008.

[2] T. Jakobsen, and K. Folgerø, "Dielectric Measurement of Gas Hydrate Formation in Water-in-Oil Emulsions using Open-Ended Coaxial Probes," *Measurement Science and Technology*, vol. 8, pp. 1006–1015, 1997.

[3] J. J. Caroll, *Natural Gas Hydrates - A Guide for Engineers* second ed., United States of America: Elsevier, 2009.

[4] J. Baker-Jaevis, M. D. Janezic, P. D. Domich *et al.*, "Analysis of an Open-Ended Coaxial Probe with Lift-Off for Nondestructive Testing," *IEEE Transactions on Instrumentation and Measurement*, vol. 43, no. 5, pp. 711-718, 1994.

[5] K. Folgerø, "Coaxial sensors for broad-band complex permittivity measurements of petroleum fluids," Department of Physics, University of Bergen, Norway, 1996.

[6] N. Marcuvitz, *Waveguide handbook*, New York: McGraw-Hill, 1951.

[7] E. Tanabe, and W. T. Joines, "A Nondestructive Method for Measuring Complex Permittivity of Dielectric Materials at Microwave-Frequencies Using an Open Transmission Line Resonator," *IEEE Transactions on Instrumentation and Measurement* vol. 25, no. 3, pp. 222-226, 1976.

[8] T. W. Athey, M. A. Stuchly, and S. S. Stuchly, "Measurement of Radio Frequency Permittivity of Biological Tissues with an Open-Ended Coaxial Line. Part I," *IEEE Transactions on Microwave Theory and Techniques*, vol. 30, no. 1, pp. 82-86, 1982.

[9] M. A.Stuchly, T. W. Athey, G. M. Samaras *et al.*, "Measurement of Radio Frequency Permittivity of Biological Tissues with an Open-Ended Coaxial Line: Part II. Experimental Results," *IEEE Transactions on Microwave Theory and Techniques*, vol. 30, no. 1, pp. 87-92, 1982.

[10] Gregory Gajda, and S. S. Stuchly, "An Equivalent Circuit of an Open-Ended Coaxial Line," *IEEE Transactions On Instrumentation And Measurement*, vol. 32, no. 4, pp. 506-508, 1983.

[11] G. B. Gajda, and S. S. Stuchly, "Numerical Analysis of Open-Ended Coaxial Lines," *IEEE Transactions on Microwave Theory and Techniques*, vol. 31, no. 5, pp. 380-384, 1983.

[12] A. Kraszewski, and S. S. Stuchly, "Capacitance of Open-Ended Dielectric-Filled Coaxial Lines Experimental Results," *IEEE Transactions on Instrumentation and Measurement*, vol. 32, no. 4, pp. 517-519, 1983.

[13] P. D. Langhe, L. Martens, and D. D. Zutter, “Design Rules for an Experimental Setup Using an Open-Ended Coaxial Probe Based on Theoretical Modelling,” *IEEE Transactions on Instrumentation and Measurement*, vol. 43, no. 6, pp. 810-817, 1994.

[14] P. D. Langhe, K. Blomme, L. Martens *et al.*, “Measurement of Low-Permittivity Materials Based on a Spectral-Domain Analysis for the Open-Ended Coaxial Probe,” *IEEE Transactions on Instrumentation and Measurement,* vol. 42, no. 5, pp. 879-886, 1993.

[15] C.-L. Li, and K.-M. Chen, “Determination of Electromagnetic Properties of Materials Using Flanged Open-Ended Coaxial Probe Full-Wave Analysis,” *IEEE Transactions onInstrumentation and Measurement,* vol. 44, no. 1, pp. 19-27, 1995.

[16] D. K. Misra, “Evaluation of the Complex Permittivity of Layered Dielectric Materials with the Use of an Open-Ended Coaxial Line,” *Microwave and Optical Technology Letters,* vol. 11, no. 4, pp. 183-187, 1996.

[17] S. Bakhtiari, S. I. Ganchev, and R. Zoughi, “Analysis of Radiation from an Open-Ended Coaxial Line into Stratified Dielectrics,” *IEEE Transactions on Microwave Theory and Techniques,* vol. 42, no. 7, pp. 1261-1267, 1994.

[18] L. L. Li, N. H. Ismail, L. S. Taylor *et al.*, “Flanged Coaxial Microwave Probes for Measuring Thin Moisture Layers,” *IEEE Transactions on Biomedical Engineering,* vol. 39, no. 1, pp. 49-57, 1992.

[19] G. Chen, K. Li, and Z. Ji, “Bilayered Dielectric Measurement with an Open-Ended Coaxial Probe,” *IEEE Transactions on Microwave Theory and Techniques,* vol. 42, no. 6, pp. 966-971, 1994.

[20] T. Friisø, “Quality Determination of Petroleum Liquids from Complex Permittivity Spectra,” Department of Physics, University of Bergen, Norway, 1997.

[21] J. N. Israelachvili, *Intermolecular and Surface Forces,* USA: Elsevier, 2011.

[22] L. F. Chen, C. K. Ong, C. P. Neo *et al.*, *Microwave Electronics, Measurement and Materials Characterisation* UK: John Wiley & Sons, Ltd., 2004.

[23] Wikipedia. "Complex Permittivity," 25.10.2012; http://en.wikipedia.org/wiki/Complex_permittivity#Complex_permittivity.

[24] D. J. Griffiths, *Introduction to Electrodynamics*, 3rd ed., International Edition: Pearson - Benjamin Cummings, 1981.

[25] J. W.Jewett, and R. A. Serway, *Physics for Scientists and Engineers with Modern Physics*, 8th ed., Canada: Brooks/Cole, 2010.

[26] A. R. Von Hippel, and R. B. Adler, *Molecular science and molecular engineering*, New York: Published jointly by the Technology Press of M.I.T. and J.Wiley, 1959.

[27] P. Debye, *Polar molecules*, New York: Book Department, The Chemical Catalog Company, 1929.

[28] P. Petong, R. Pottel, and U. Kaatze, "Water-Ethanol Mixtures at Different Compositions and Temperatures. A Dieletric Relaxation Study," *Journal of Physical Chemistry A*, vol. 104, no. 32, pp. 7420-7428, Aug 17, 2000.

[29] U. Kaatze, M. Schäfer, and R. Pottel, "The Complex Dielectric Spectrum of Aqueous Methanol and Isopropanol Solutions," *Zeitschrift für Physikalische Chemie*, vol. 165, no. Part I, pp. 103-117, 1989/01/01, 1989.

[30] P. Petong, R. Pottel, and U. Kaatze, "Dielectric Relaxation of H-Bonded Liquids. Mixtures of Ethanol and n-Hexanol at Different Compositions and Temperatures," *The Journal of Physical Chemistry A*, vol. 103, no. 31, pp. 6114-6121, 1999/08/01, 1999.

[31] J. Crossley, "Dielectric Relaxation and Hydrogen Bonding in Lliquids," *Advances in Molecular Relaxation Processes*, vol. 2, no. 1, pp. 69-99, 1970.

[32] K. S. Cole, and R. H. Cole, "Dispersion and Absorption in Dielectrics I. Alternating Current Characteristics," *The Journal of Chemical Physics*, vol. 9, no. 4, pp. 341-351, 1941.

[33] W. B. Weir, "Automatic Measurement of Complex Dielectric-Constant and Permeability at Microwave-Frequencies," *Proceedings of the IEEE*, vol. 62, no. 1, pp. 33-36, 1974.

[34] R. H. Cole, "Bridge Sampling Methods for Admittance Measurements from 500 KHz to 5 GHz," *IEEE Transactions on Instrumentation and Measurement*, vol. 32, no. 1, pp. 42-47, 1983.

[35] K. Folgerø, K.-E. Frøysa, T. Tjomsland *et al.*, "Wet Gas Measurement- Determination of Water Cut in Liquid Films by Open-Ended Coaxial Probes.," *CMR Confidential Report*, 1995.

[36] T. P. Marsland, and S. Evans, "Dielectric Measurements with an Open-Ended Coaxial Probe," *IEE Proceedings H*, vol. 134, no. 4, pp. 341-349, 1987.

[37] J. P. Bentley, *Principles of measurement systems*, Harlow: Pearson/Prentice Hall, 2005.

[38] K. Asami, "Characterization of Heterogeneous Systemsby Dielectric Spectroscopy," *Progress in Polymer Science-Elsevier Science Ltd.*, vol. 27, pp. 1617–1659, 2002.

[39] J. C. Maxwell, *Treatise on electricity and magnetism.* : Oxford-Clarendon Press, 1891.

[40] K. W. Wagner, " Erklärung der dielektrishen Nachwirkungsvorgänge auf Grund Maxerllsher Vorstellungen," *Arch Electrotechnik*, 1914.

[41] T. Hanai, *Theory of the Dielectric Dispersion Due to the Interfacial Polarization and its Application to Emulsion. Kolloid-Z*, 1960.

[42] M. H. Boyle, “The Electrical Properties of Heterogeneous Mixtures Containing an Oriented Spheroidal Dispersed Phase.,” *Colloid Polym Sci ;263:51–7.*, 1985.

[43] A. Peyman, C. Gabriel, and E. H. Grant, “Complex Permittivity of Sodium Chloride Solutions at Microwave Frequencies,” *Bioelectromagnetics 28*, pp. 264-274, 2007.

[44] T. Jakobsen, “Clathrate Hydrate Studies by Means of Time-Domain Dielectric Spectroscopy,” Department of Chemistry, University of Bergen, Norway, 1996.

[45] K. Folgerø, "Maxwell-Wagner effect - Permittivity sensors Part I (PHYS-328)," *Lecture note*, CMR, 2009.

[46] A. P. Gregory, R. N. Clarke, and M. G. Cox, “Traceable Measurement of Dielectric Reference Liquids over the Temperature Interval 10–50 C using Coaxial-Line Methods,” *Measurement Science and Technology*, vol. 20, pp. 19, 2009.

[47] M. T. Ghannam, and M. Y. E. Selim, “Stability Behavior of Water-in-Diesel Fuel Emulsion,” *Petroleum Science and Thechnology* vol. 27, pp. 396-411, 2009.

[48] "SUHNER Huber," Comercially available information.

[49] K. Haukalid, “Den Coplanare Bølgelederen som Permittivitetssensor,” Master project thesis, Department of Physics and Technology, University of Bergen Norway, 2011.

[50] Agilent-Technologies. "Network Analyzer Basics," 01.11.2012; http://cp.literature.agilent.com/litweb/pdf/5965-7917E.pdf.

Appendix A

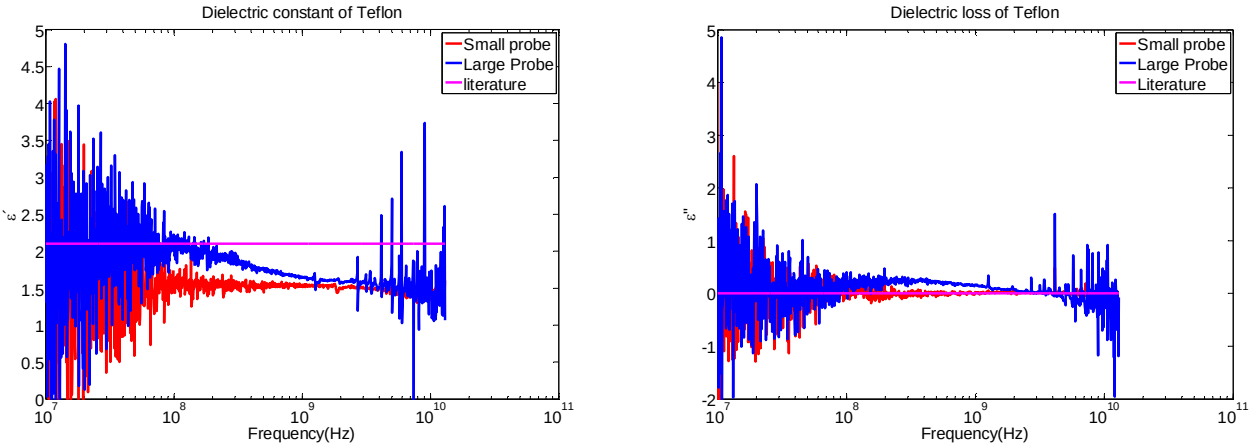

Figure A.1: Estimated dielectric constant and dielectric loss of Teflon when the three calibration fluids are: methanol, ethanol and air.

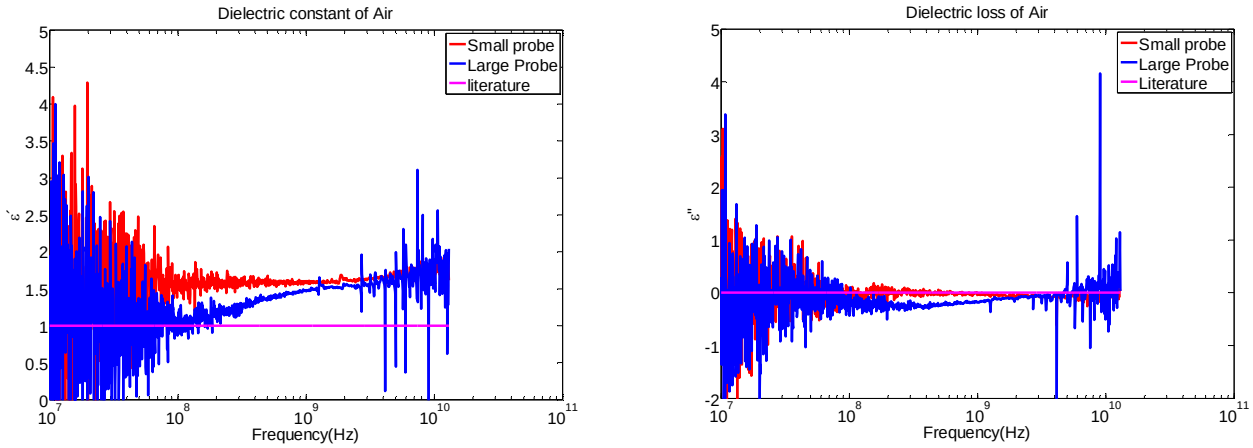

Figure A.2: Estimated dielectric constant and dielectric loss of air when the three calibration fluids are: methanol, ethanol and Teflon.

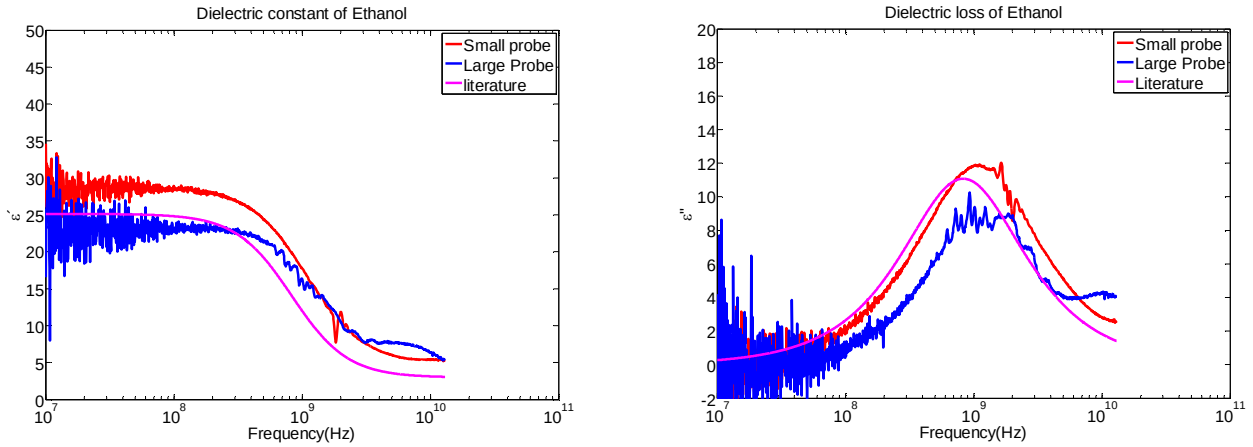

Figure A.3: Estimated dielectric constant and dielectric loss of ethanol when the three calibration fluids are: air, methanol and distilled water.

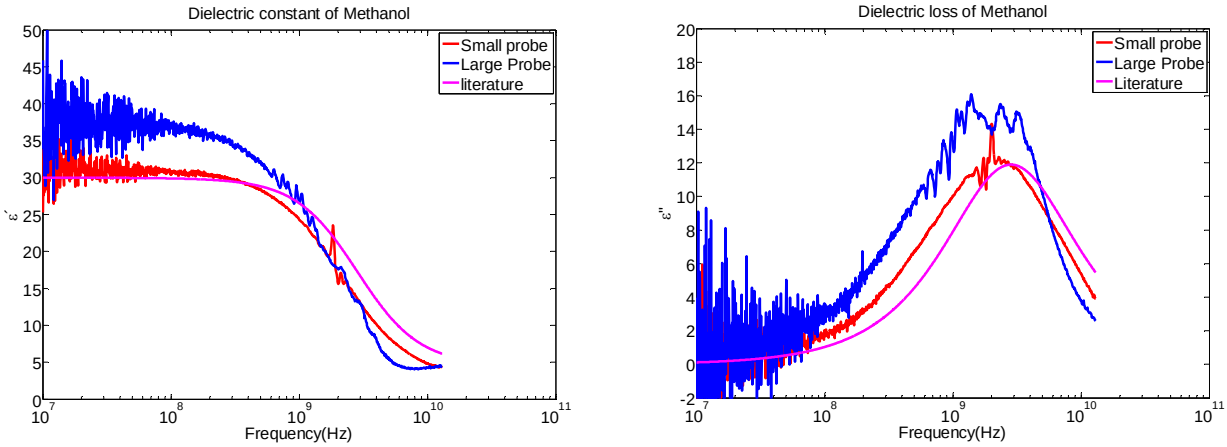

Figure A.4: Estimated dielectric constant and dielectric loss of methanol when the three calibration fluids are: air, ethanol and distilled water.

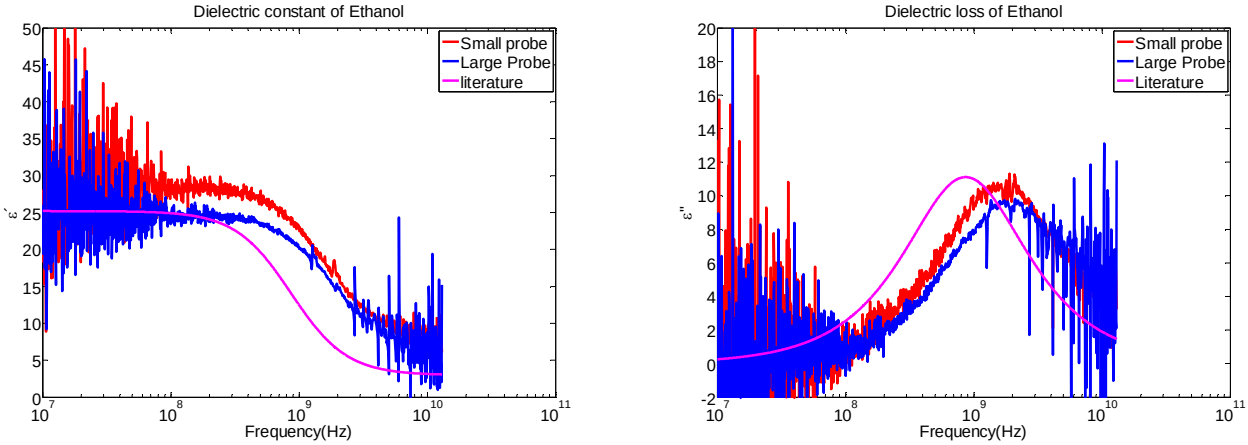

Figure A.5: Estimated dielectric constant and dielectric loss of ethanol when the three calibration fluids are: air, methanol and Teflon.

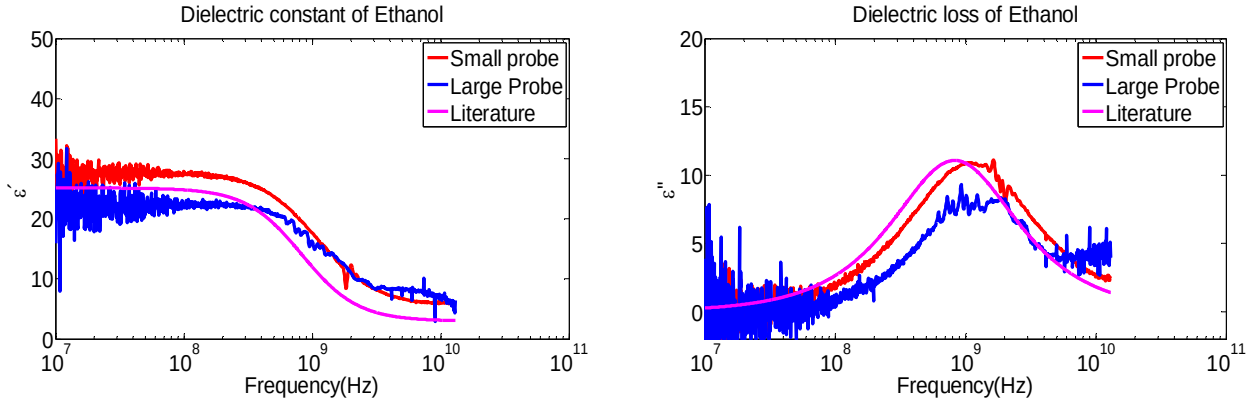

Figure A.6: Estimated dielectric constant and dielectric loss of ethanol when the three calibration fluids are: distilled water, methanol and Teflon.

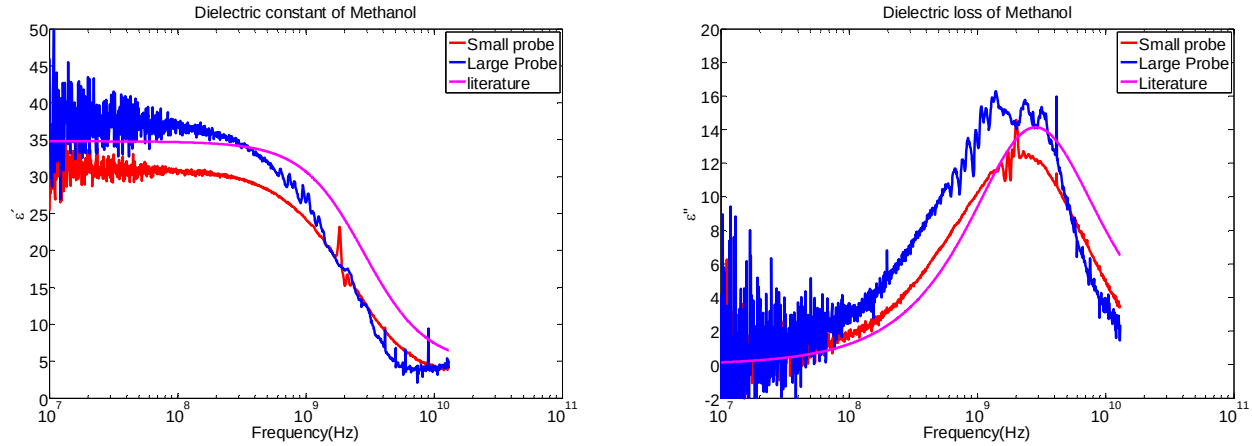

Figure A.7: Estimated dielectric constant and dielectric loss of methanol when the three calibration fluids are: distilled water, ethanol and Teflon.

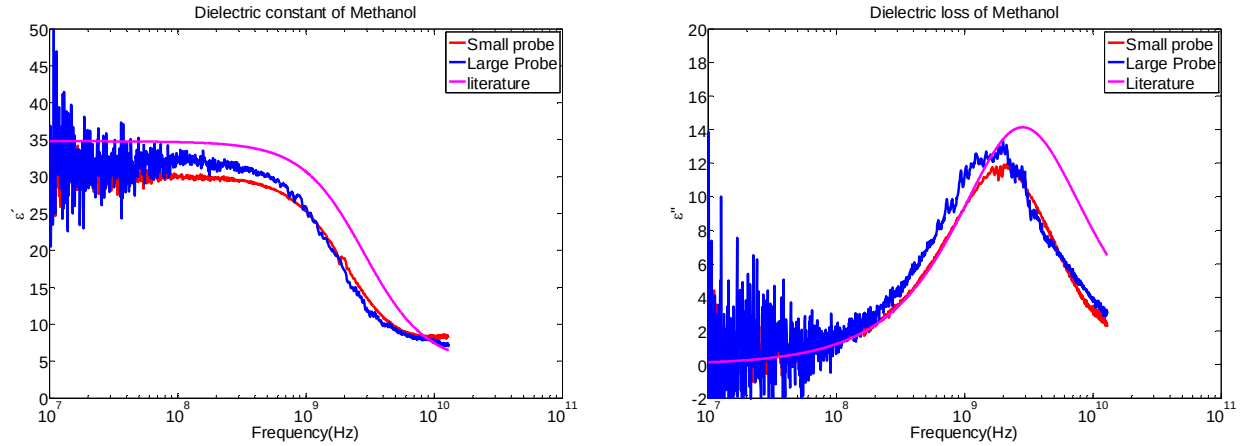

Figure A.8: Estimated dielectric constant and dielectric loss of methanol when the three calibration fluids are: air, distilled water and ethanol/water mixture x_e=0.54.

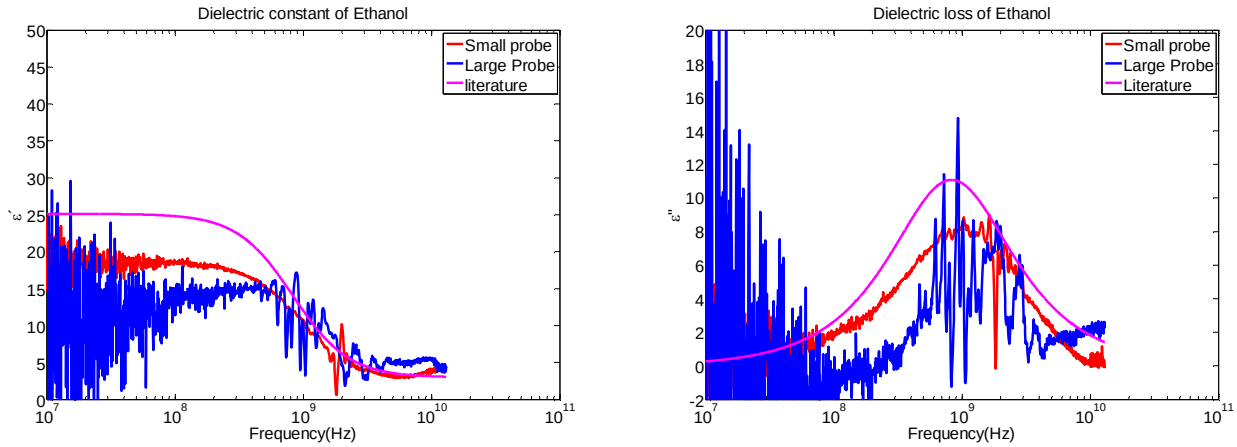

Figure A.9: Estimated dielectric constant and dielectric loss of ethanol when the three calibration fluids are: air, distilled water and ethanol/water mixture x_e=0.54.

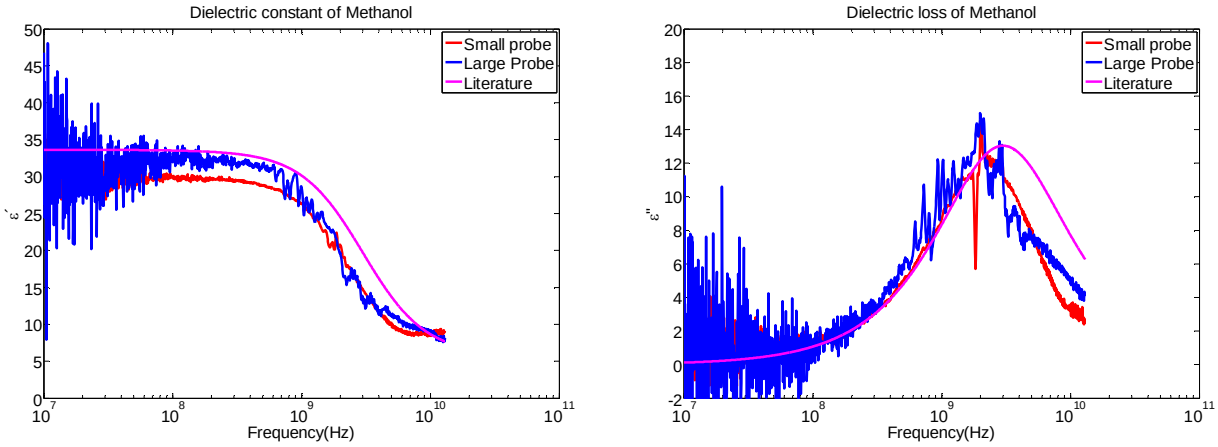

Figure A.10: Estimated dielectric constant and dielectric loss of methanol when the three calibration fluids are: air, distilled water and ethanol/water mixture x_e=0.36.

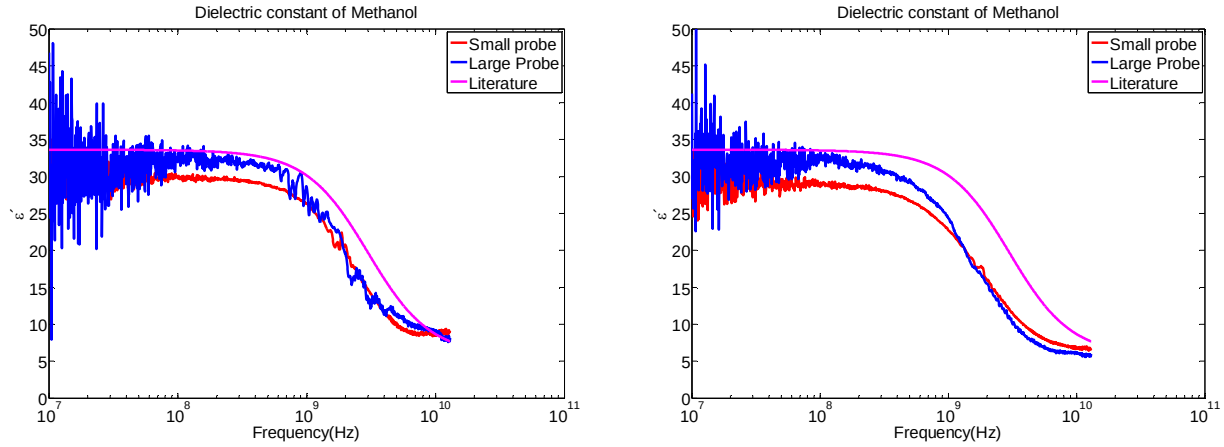

Figure A.11: Estimated dielectric constant of methanol with two different calibration set. The three calibration fluids in the left figure are: air, distilled water and ethanol/water mixture x_e=0.36, while in the right figure distilled water is replaced with ethanol/water mixture x_e=0.76.

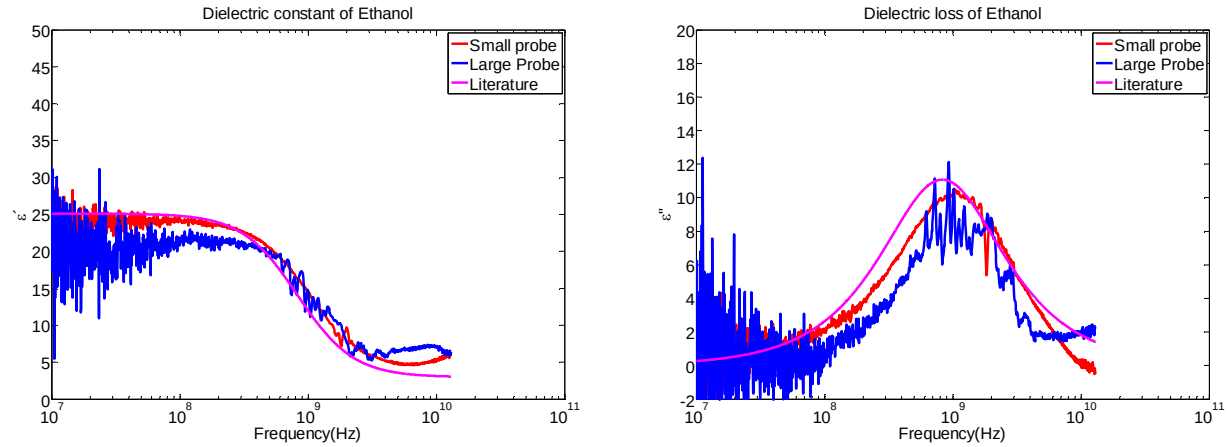

Figure A.12: Estimated dielectric constant and dielectric loss of ethanol when the three calibration fluids are: air, ethanol/water mixture x_e=0.36 and distilled water.

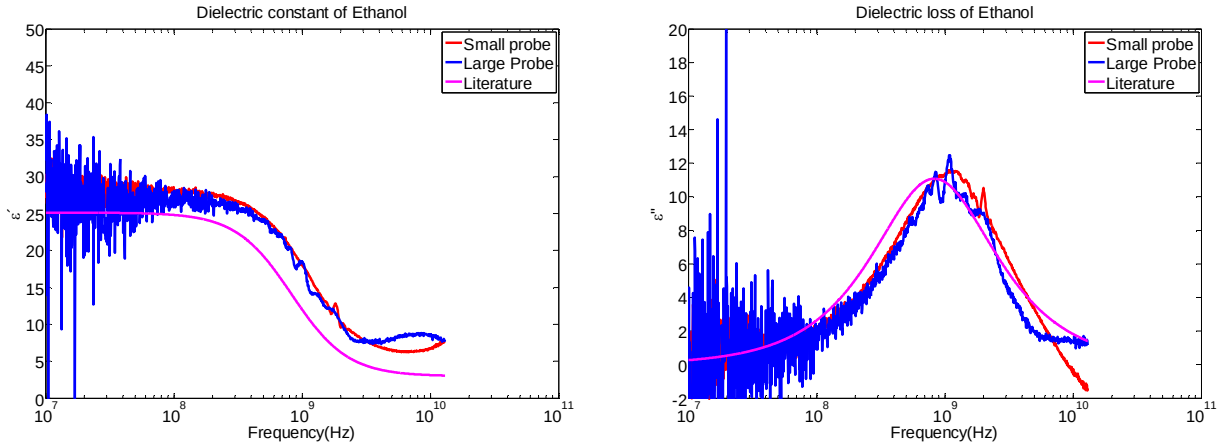

Figure A.13: Estimated dielectric constant and dielectric loss of ethanol when the three calibration fluids are: air, ethanol/water mixture x_e=0.36 and ethanol/water mixture x_e=0.22.

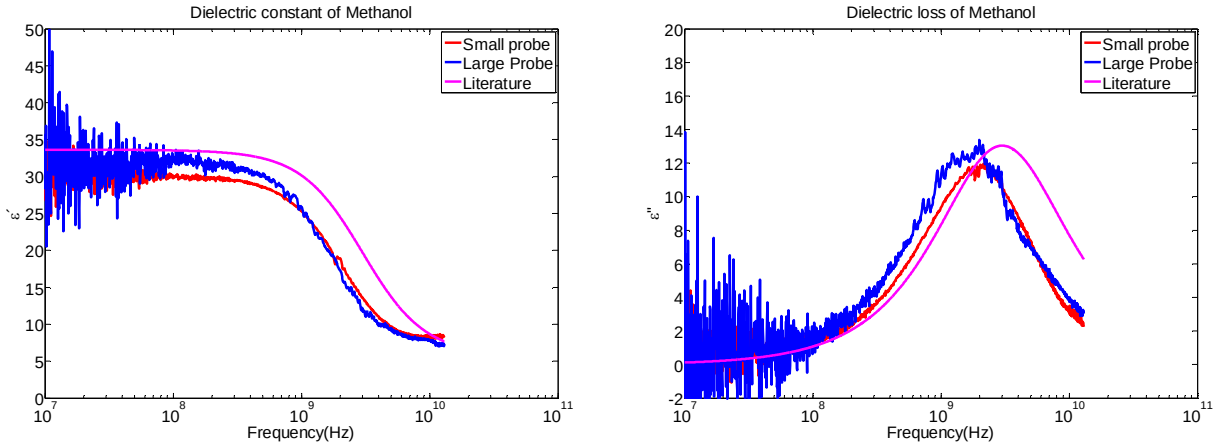

Figure A.14: Estimated dielectric constant and dielectric loss of methanol when the three calibration fluids are: air, ethanol/water mixture x_e=0.54 and distilled water.

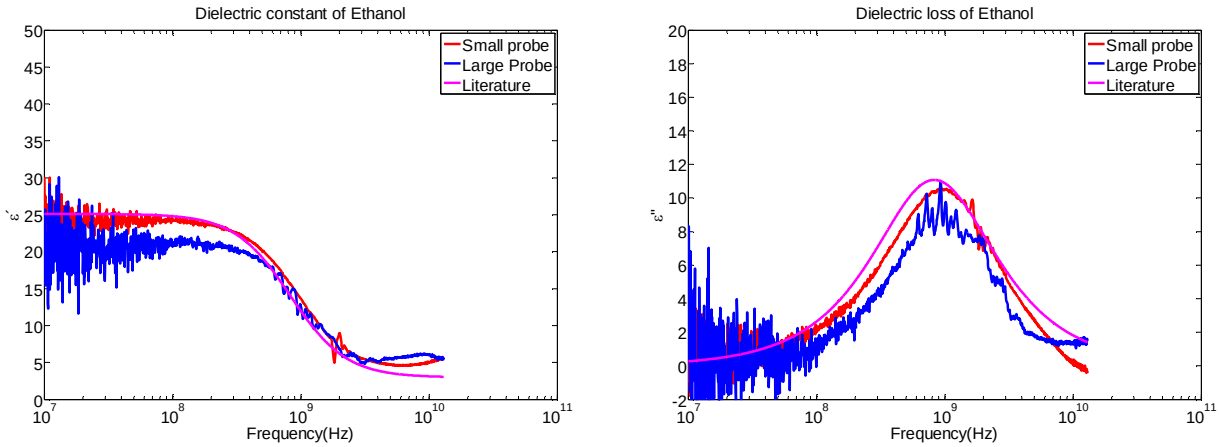

Figure A.15: Estimated dielectric constant and dielectric loss of ethanol when the three calibration fluids are: air, ethanol/water mixture x_e=0.54 and distilled water.

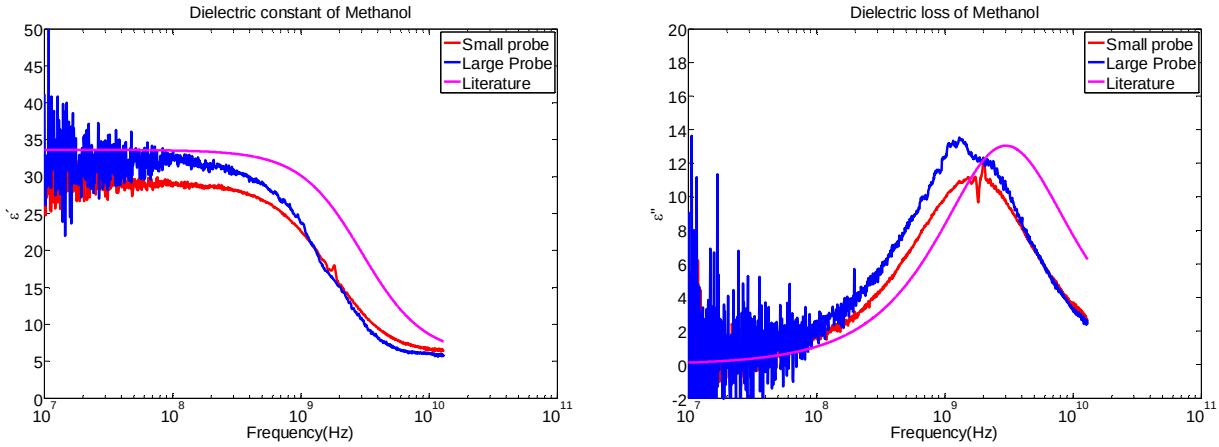

Figure A.16: Estimated dielectric constant and dielectric loss of methanol when the three calibration fluids are: air, ethanol/water mixture x_e=0.76 and distilled water.

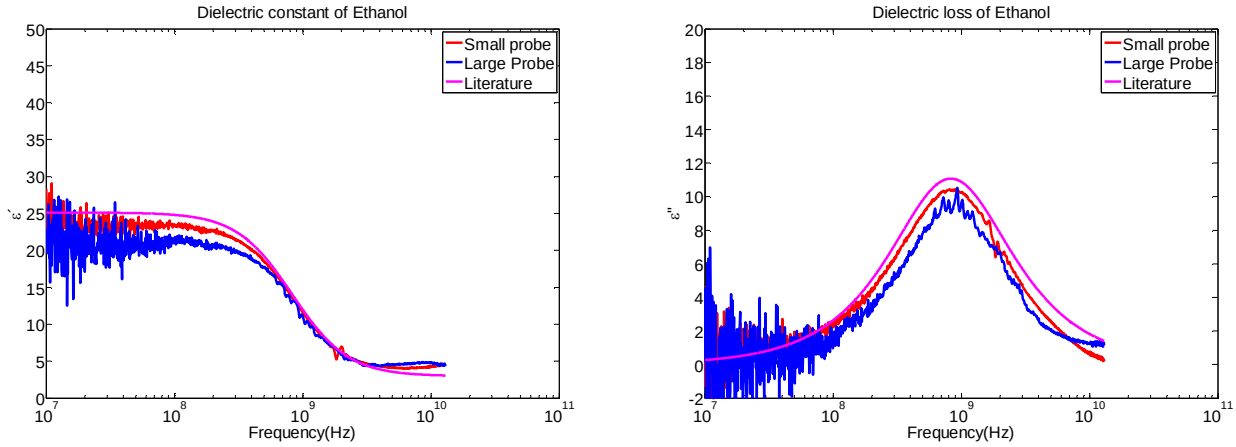

Figure A.17: Estimated dielectric constant and dielectric loss of ethanol when the three calibration fluids are: air, ethanol/water mixture x_e=0.76 and distilled water.

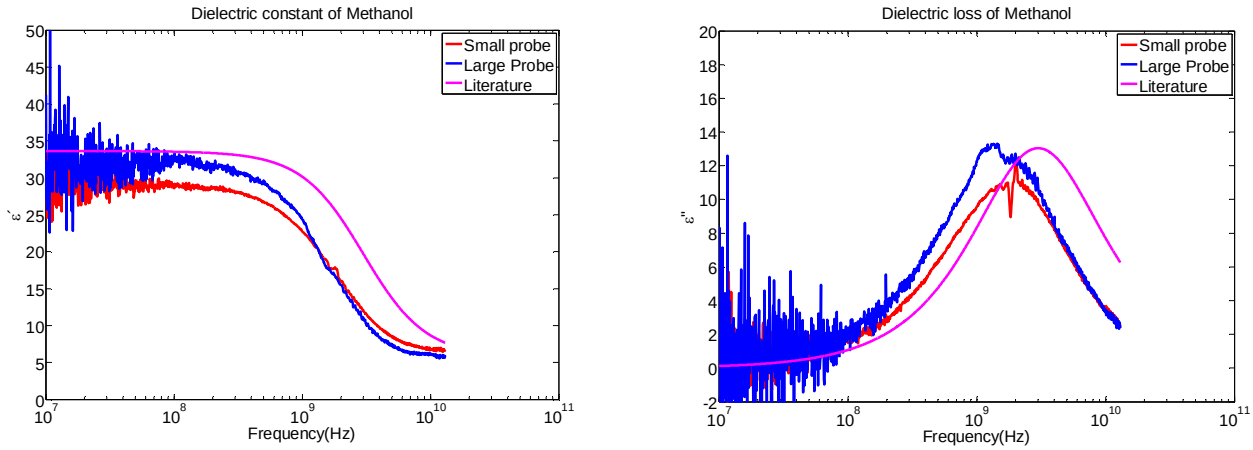

Figure A.18: Estimated dielectric constant and dielectric loss of methanol when the three calibration fluids are: air, ethanol/water mixture x_e=0.36 and ethanol/water mixture x_e=0.76.

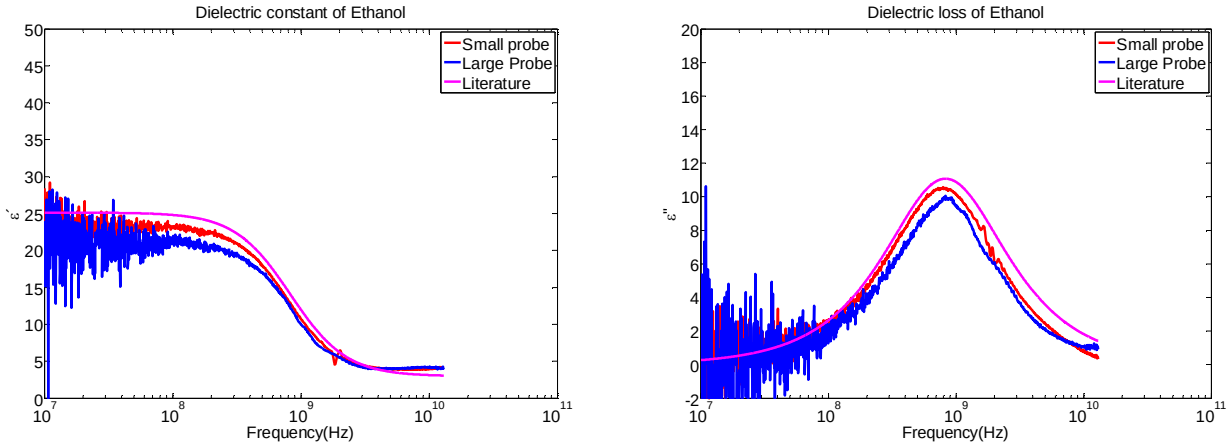

Figure A.19: Estimated dielectric constant and dielectric loss of ethanol when the three calibration fluids are: air, ethanol/water mixture x_e=0.36 and ethanol/water mixture x_e=0.76.

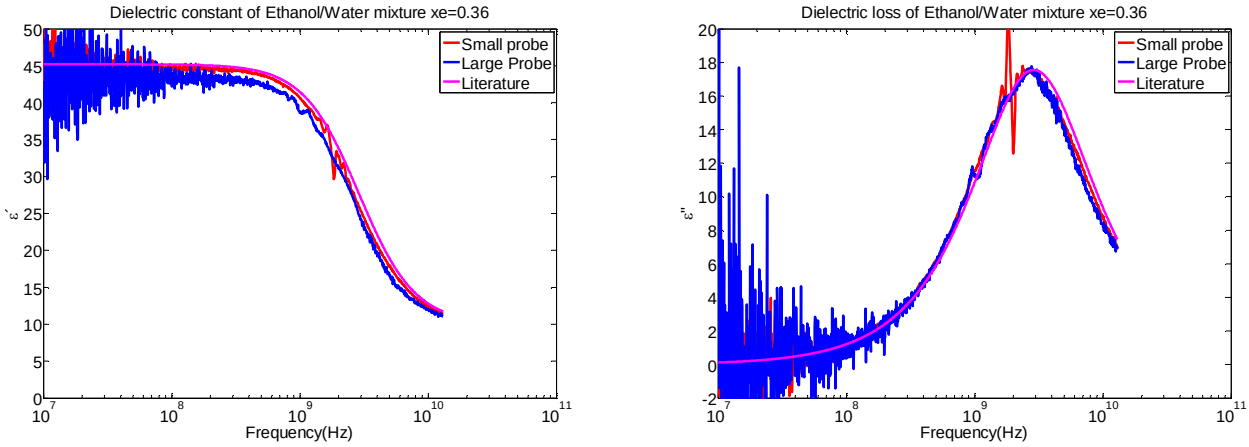

Figure A.20: Estimated dielectric constant and dielectric loss of ethanol/water mixture x_e=0.36 when the three calibration fluids are: ethanol/water mixture x_e=0.22, ethanol/water mixture x_e=0.54 and ethanol/water mixture x_e=0.76.

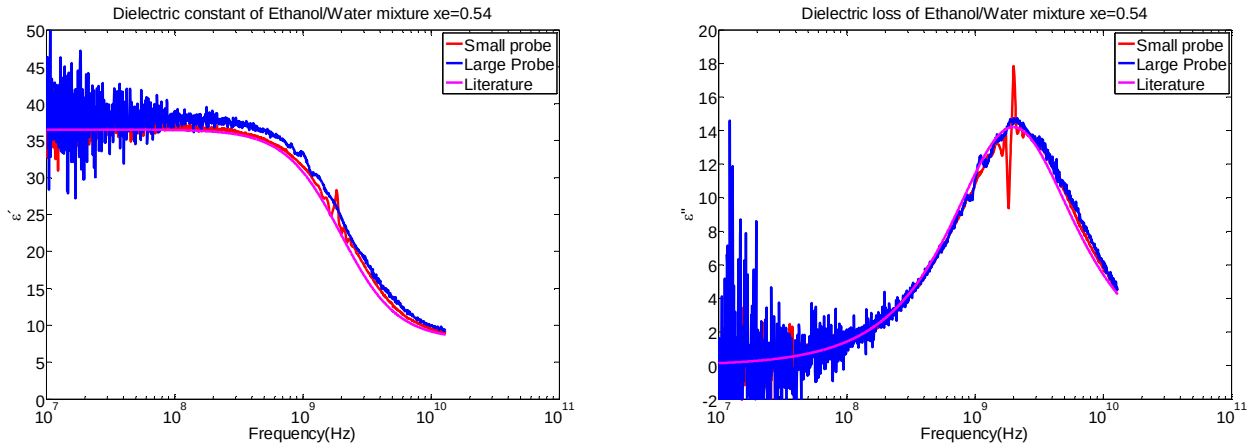

Figure A.21: Estimated dielectric constant and dielectric loss of ethanol/water mixture x_e=0.54 when the three calibration fluids are: ethanol/water mixture x_e=0.22, ethanol/water mixture x_e=0.36 and ethanol/water mixture x_e=0.76.

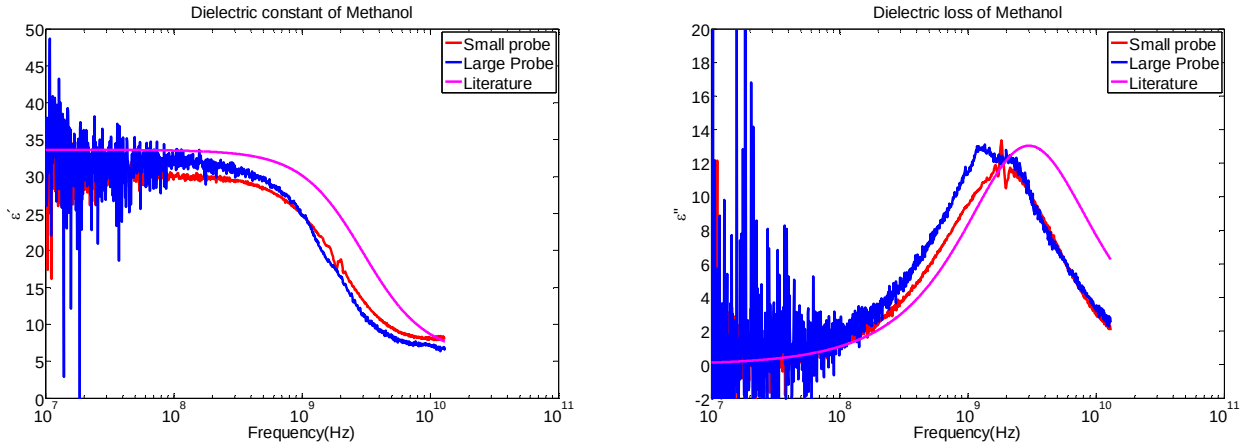

Figure A.22: Estimated dielectric constant and dielectric loss of methanol when the three calibration fluids are: air, ethanol/water mixture x_e=0.36 and ethanol/water mixture x_e=0.54.

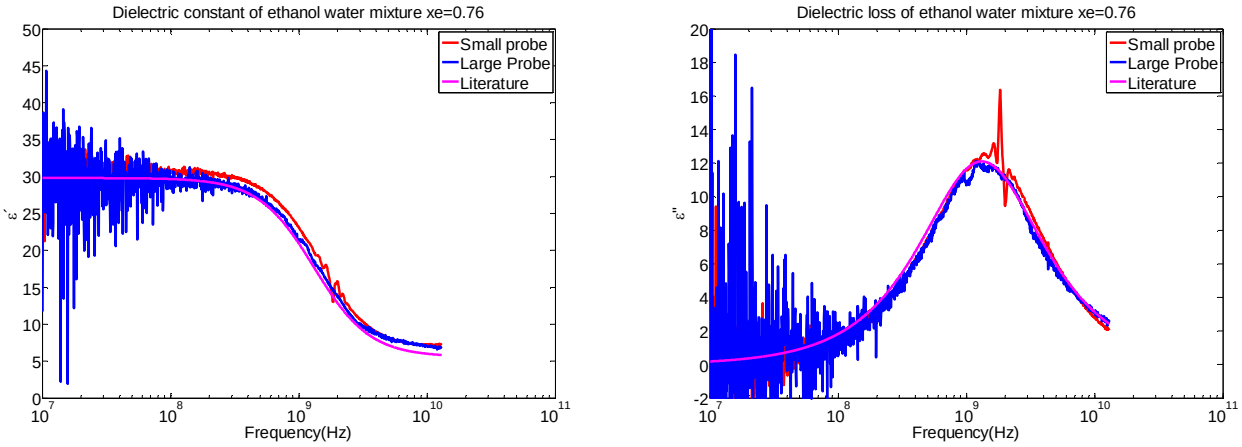

Figure A.23: Estimated dielectric constant and dielectric loss of ethanol/water mixture x_e=0.76 when the three calibration fluids are: air, ethanol and ethanol/water mixture x_e=0.54.

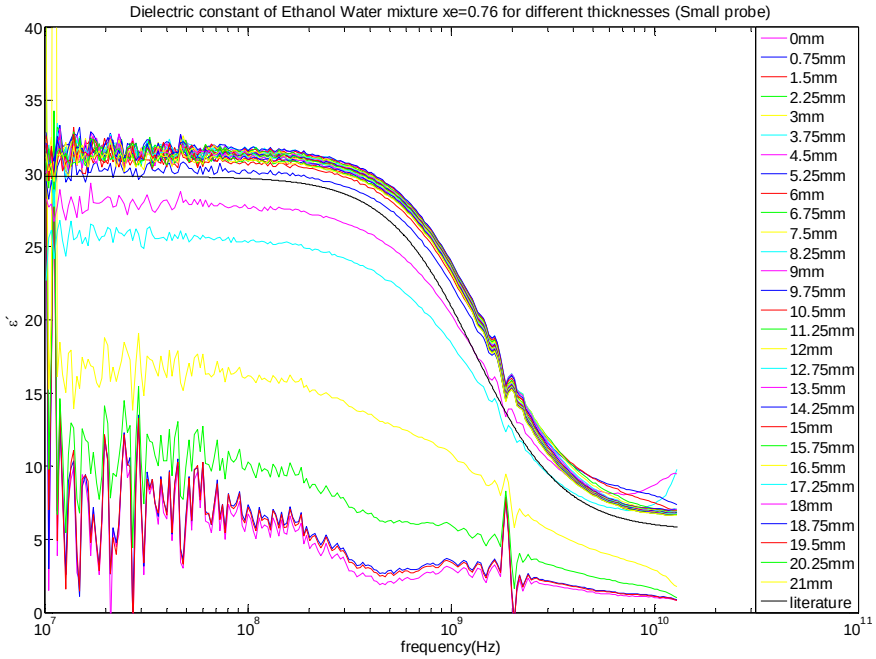

Figure A. 24: Estimated apparent permittivity of ethanol/water mixture x_e=0.76 by the small probe, when the three calibration fluids are: ethanol, ethanol/water mixture x_e=0.36 and ethanol/water mixture x_e=0.54. The thickness of fluid is increased from 0 to 21 mm in steps of 0.75 mm.

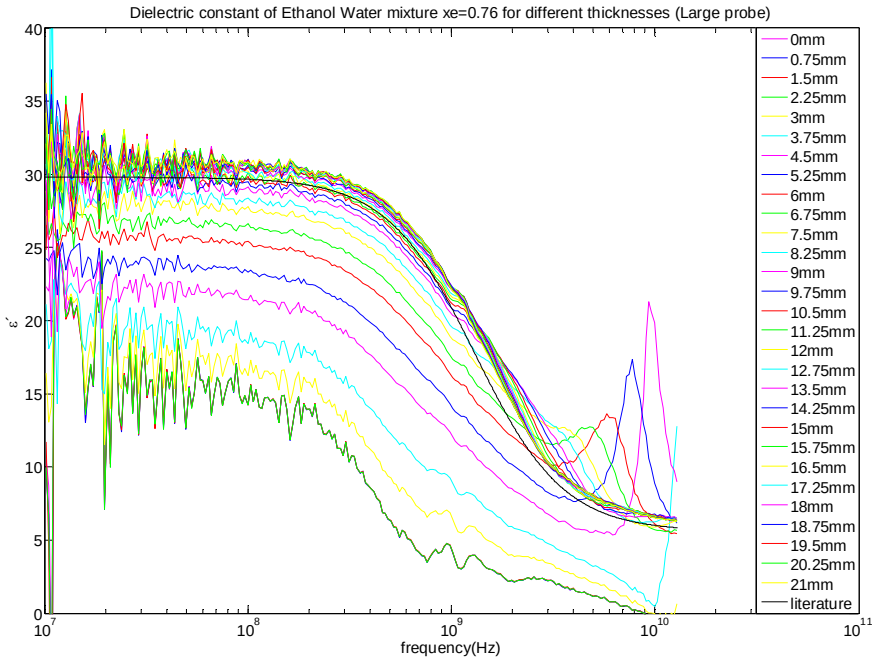

Figure A.25: Estimated apparent permittivity ethanol/water mixture x_e=0.76 by the large probe, when the three calibration fluids are: ethanol, ethanol/water mixture x_e=0.36 and ethanol/water mixture x_e=0.54. The thickness of fluid is increased from 0 to 21 mm in steps of 0.75 mm.

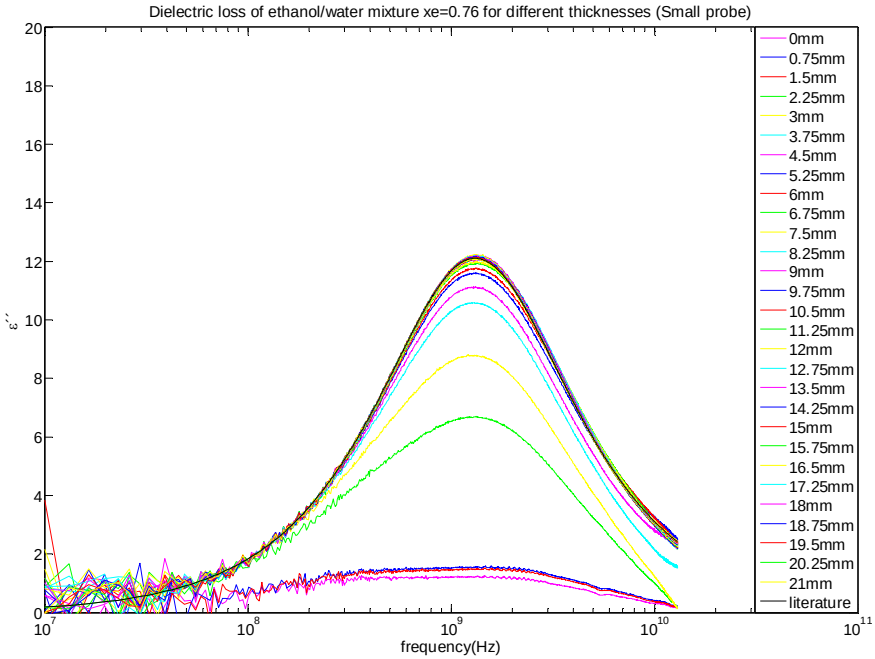

Figure A.26: Dielectric loss of ethanol/water mixture x_e=0.76 versus frequency for different thicknesses of test fluid with using the Teflon part (small probe) with the ideal calibration set. The thickness of fluid is increased from 0 to 21 mm in steps of 0.75 mm.

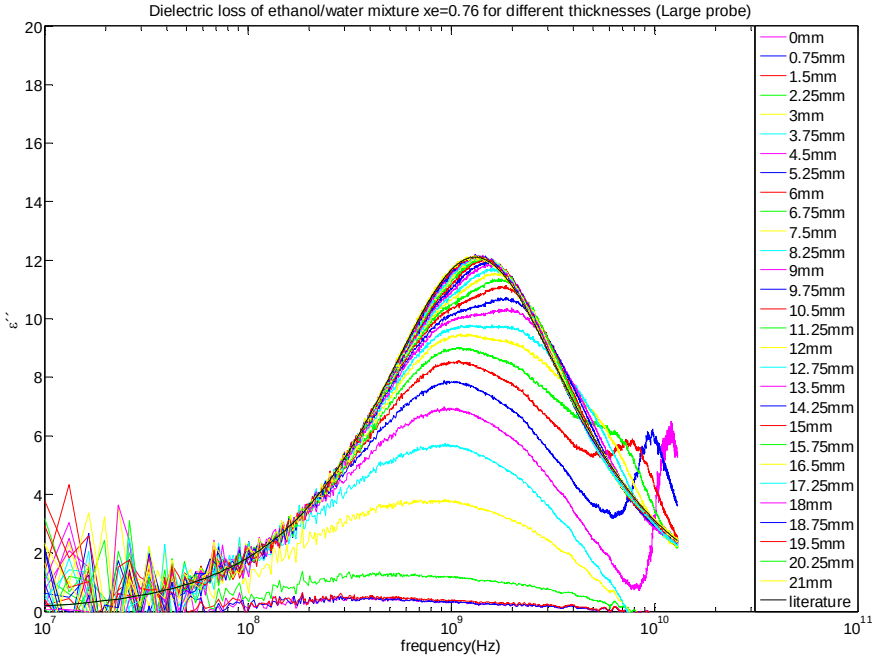

Figure A.27: Dielectric loss of ethanol/water mixture x_e=0.76 versus frequency for different thicknesses of test fluid with using the Teflon part (large probe) with the ideal calibration set. The thickness of fluid is increased from 0 to 21 mm in steps of 0.75 mm.

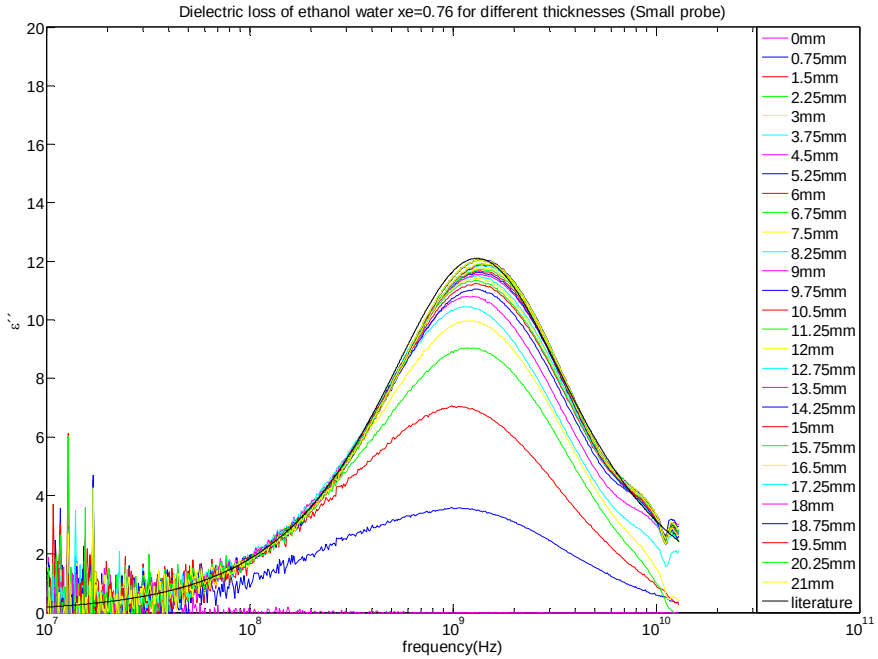

Figure A. 28: Dielectric loss of ethanol/water mixture x_e=0.76 versus frequency for different thicknesses of test fluid without the Teflon part (small probe) with the ideal calibration set. The thickness of fluid is increased from 0 to 21 mm in steps of 0.75 mm.

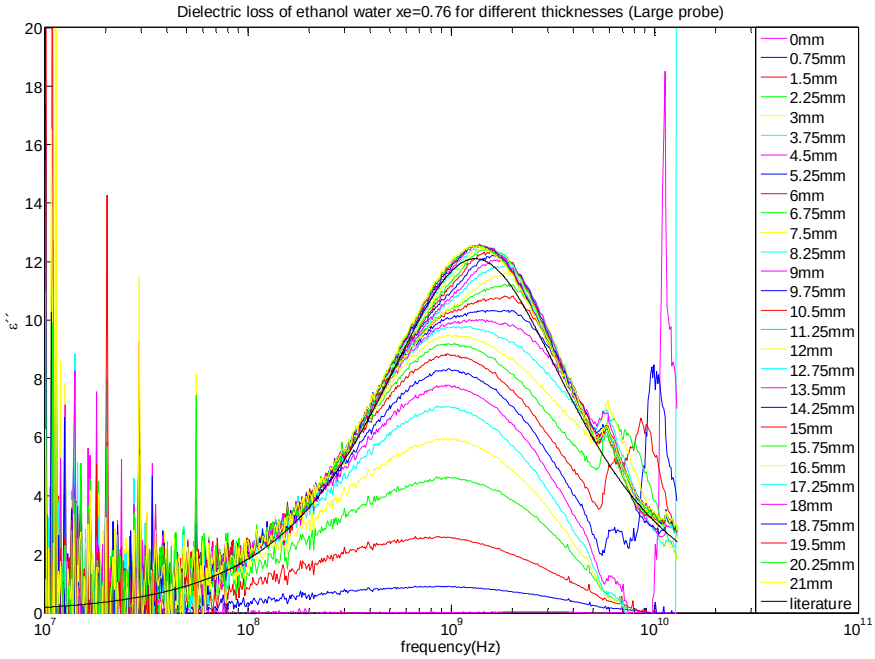

Figure A. 29: Dielectric loss of ethanol/water mixture x_e=0.76 versus frequency for different thicknesses of test fluid without the Teflon part (large probe) with the ideal calibration set. The thickness of fluid is increased from 0 to 21 mm in steps of 0.75 mm.

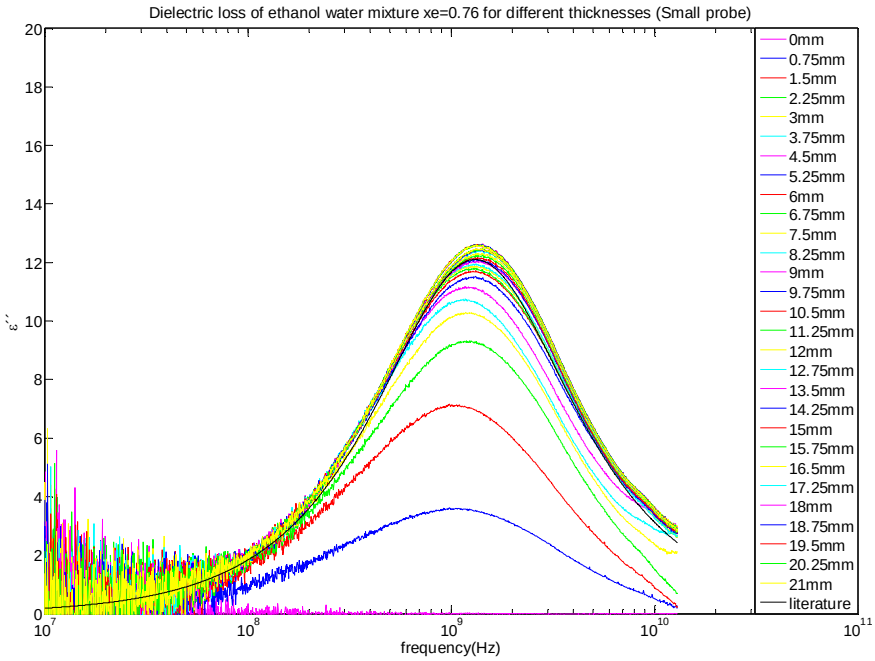

Figure A.30: Estimated dielectric loss of ethanol/water mixture x_e=0.76 by the small probe with the best calibration set and without using the height adjustment system. The thickness of fluid is increased from 0 to 21 mm in steps of 0.75 mm

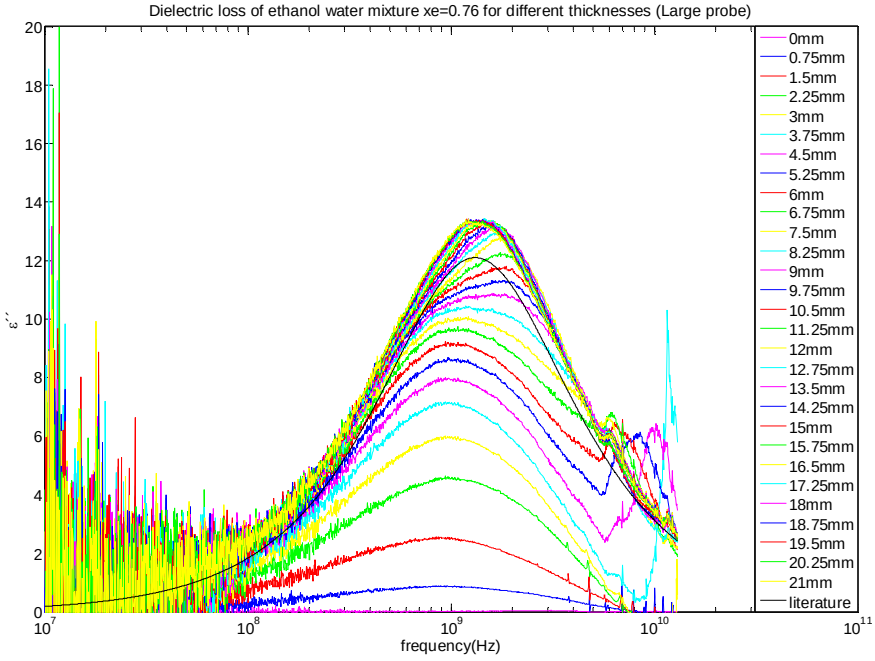

Figure A.31: Estimated dielectric loss of ethanol/water mixture x_e=0.76 by the large probe with the best calibration set and without using the height adjustment system. The thickness of fluid is increased from 0 to 21 mm in steps of 0.75 mm

Appendix B

The electrical network analyzer can test high frequency electrical network, and can characterize both linear and non-linear behaviour of the device. When electromagnetic signal incidents to an electrical network some of the signal is reflected whereas some continue through device. The network analysis is concerned with the accurate measurement of the reflected to the incident signal, and the transmitted signal to the incident signal.

The components are tested for a variety of reasons:

- Verify specification of "building blocks" for more complex RF systems
- Ensure distortion less transmission of communication signals
    - Linearity
    - Non-linearity
- Ensure good matching when absorbing power e.g. by an antenna

Complete characterization of devices and networks involves measurement of phase as well as magnitude.

In the high frequency range, the wavelength of the signal is comparable to or much smaller than the length of the conductors. In this case power transmission can best be thought of in terms of a travelling wave. A lossless transmission line has characteristic impedance (Z_0). When the transmission line is terminated in its characteristic impedance, maximum power is transferred to the load. When the termination is not Z_0, the portion of the signal which is not absorbed by the load is reflected back toward the source. This creates a condition where the envelope voltage along the transmission line varies with position. The fundamental parameter of a transmission line is its characteristic impedance Z_0 which describes relation between the voltage and current travelling waves. Z_0 is a function of the dielectric constant of the non-conducting material in the transmission line. For RF and microwave application, coaxial transmission lines are designed to have a characteristic impedance of 50 Ω.

In common network analyzer terminology the incident wave is measured with the R (for reference) receiver. The reflected wave is measured with the A receiver and the transmitted wave is measured with the B receiver, as shown in Figure B.1. With amplitude and phase

information of these three waves available, the reflection and transmission characteristics of the device under test (DUT) can be quantified. [50]

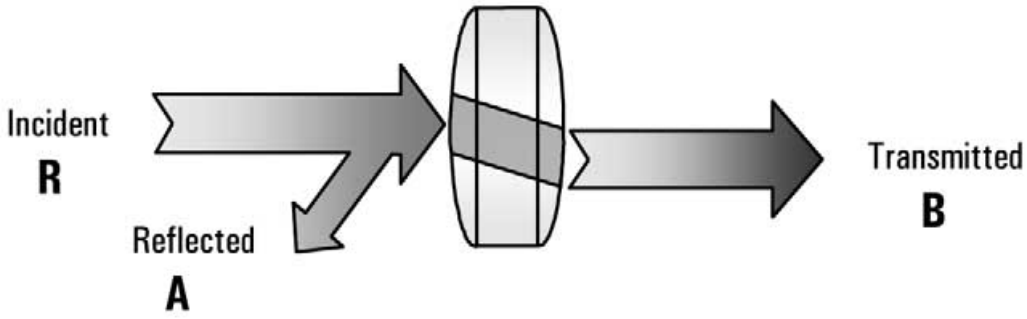

Figure B.1: Network analyzer

The reflection coefficient is the ratio of the reflected signal voltage to the incident signal voltage. It can be calculated as shown above using the impedances of the transmission line and the load.

Network analyzer is an important tool for analyzing analogue circuits. By measuring amplitude and phase of transmission and reflection coefficients of an analogue circuit, a network analyzer reveals all the network characteristics.

Network analyzers are widely used in materials property characterization over a certain frequency range [22], and it is used to measure the four elements in the scattering matrix model: S_{11}, S_{12}, S_{21} and S_{22}.

Appendix C

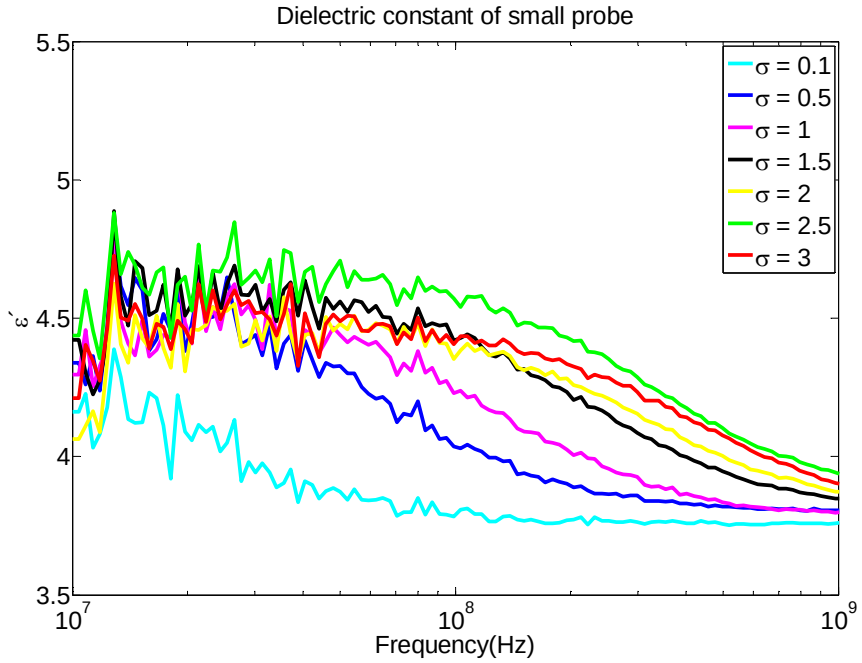

Figure C.1: Dielectric constant by the small probe for water in diesel emulsions Φ=20% with different conductivities. Calibration fluids are: ethanol/water mixture x_e=0.76, diesel and water/ diesel emulsion (Φ=20% and σ=0).

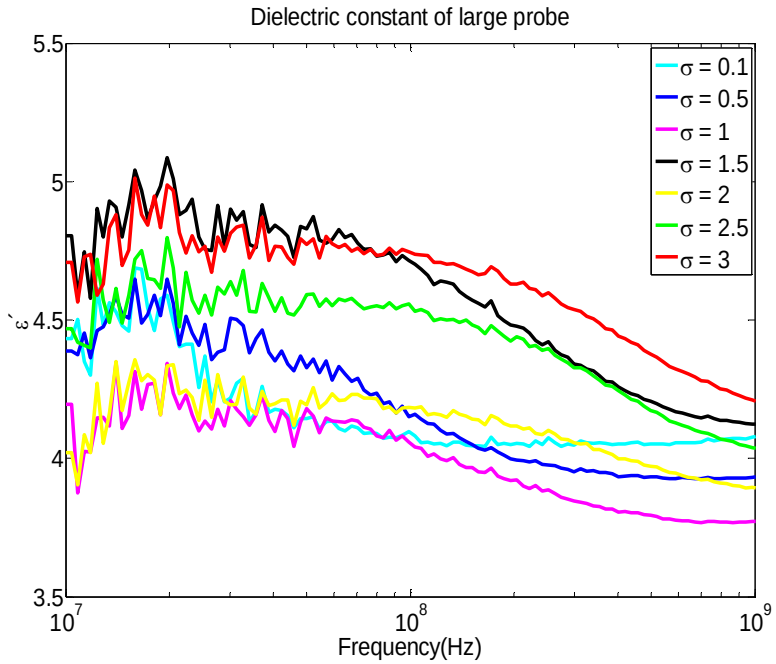

Figure C.2: Dielectric constant by the large probe for water in diesel emulsions Φ=20% with different conductivities. Calibration fluids are: ethanol/water mixture x_e=0.76, diesel and water/ diesel emulsion (Φ=20% and σ=0).